The Effect of Offshore Wind Farms on Upper Ocean Variability and Marine Ecosystems

Frida Stokkenes Eliassen

Thesis for Master of Science Degree in Energy

University of Bergen, Norway

Geophysical Institute

August 15, 2025

Year:	August 15, 2025
Title:	The Effect of Offshore Wind Farms on Upper Ocean Variability and Marine Ecosystems
Author:	Frida Stokkenes Eliassen

Acknowledgements

This master's thesis marks the completion of the 5-year integrated master's program in Energy at the University of Bergen.

First and foremost, I want to thank my supervisor, Associate Professor Mostafa Bakhoday Paskyabi. Thank you for your patience, positive attitude, and supporting words. Thank you for sharing your knowledge with me and providing valuable feedback. I would also like to thank my co-supervisor Karen de Jong for offering insight and guidance on the biological aspects of my thesis, and my co-supervisor Mohammadreza Mohammadpour Penchah for introducing me to ROMS and Fortran, and for providing basic Python example codes to help me get started. In addition, the Institute of Marine Research (IMR) and all the researchers involved in the WindSYS project – especially Anne Christine Utne Palm – deserve a huge thank you for letting me tag along on the research cruise to Hywind Tampen. It was a great learning experience filled with fond memories.

Next, I want to thank my fellow students – in particular Tora, Suhayka, and Tiril – for our weekend trip to Budapest, and for all the laughter but also the worries we have shared this past year. You made me feel less alone during this academic challenge, and for that I am grateful.

Continuing, I want to give the biggest shout-out to my cousins and friends outside of university for helping me stay engaged with my hobbies, for hosting dinners and game nights, for dragging me out on hikes and trail runs, for showing up for our monthly ocean swims with snacks and big smiles, for being interested in my progress, for giving me encouragement through the many ups and downs, for watching horror movies with me, and for overall keeping me sane throughout this entire process. You know who you are, and it goes without saying: you are all my favorite people.

I would also like to thank my wonderful coworkers at the GBALLE-LAB for showing interest in my studies, and for turning every day, evening and night spent at work into a fun and much-needed distraction. Thank you for the laughs and good times, both at and outside of work.

Last, but certainly not least, I want to express my deepest gratitude to my family. Thank you for your (almost) endless patience, and for always supporting and believing in me (and for making sure I have always had dinner to eat). I am not sure which one of us is happier that I am finally done.

Frida Stokkenes Eliassen
Bergen, 15th August 2025

Abstract

Economic growth, elevated living standards, and a growing population are all drivers of increasing electricity demand. Along comes a rise in greenhouse gas emissions, ultimately leading to a rising global temperature. To meet the goals of the Paris agreement and the Sustainable Development Goals (SDGs) set by the United Nations (UN), mitigation strategies must be implemented. Offshore wind energy is proven to be clean, renewable, highly available, cost-competitive and efficient. However, several stakeholders have raised concerns about the effect of offshore wind farms (OWFs) on ocean variability and marine ecosystems. The main objective of this thesis is how reduced wind stress in the farm wake affects vertical mass transport and distribution of temperature and nutrients – and, in turn, how this influences near-surface sound speed and primary production in the nearby areas.

This thesis uses Regional Ocean Modeling System (ROMS) with idealized numerical setup to conduct a sensitivity analysis of the impacts of OWFs on the nearby ocean environment. The analysis is conducted with eight single-farm experiments with farm size $L = 5$ km and $L = 10$ km under four different wind stress conditions (weak wind stress, moderate wind stress, strong wind stress, and combination of strong wind stress and strong wind stress reduction), as well as two multiple overlapping-farm experiments with size $L = 8$ km under strong wind stress conditions. The farm wake is analytically calculated using a Gaussian function.

The results show that OWFs can create unbalanced dipoles with upwelling on one side and downwelling on the other side of the farm. The affected area increases along with L, and the magnitude of wind stress reduction is a determining factor for the magnitude of disturbance for most of the studied properties. The findings underscore that the effect of OWFs on ocean variability is complex and varies throughout the water column. The results also suggest that the presence of OWFs causes a slight net reduction in sound speed near the surface and a net increased primary production.

While these findings provide a solid foundation for evaluating the impact of OWFs on ocean variability and marine ecosystems, further realistic and site-specific studies are needed to assess the significance of disturbances on marine life and other stakeholders. Nonetheless, the study emphasizes the importance of including wake effects in the risk assessment of offshore wind energy projects.

Contents

List of Figures

List of Tables

Nomenclature

Abbreviations

IMR	the Institute of Marine Research
NVE	the Norwegian Water Resources and Energy Directorate
OWFs	Offshore Wind Farms
ROMS	Regional Ocean Modeling System
SDGs	Sustainable Development Goals
UN	United Nations

Symbols

τ	Surface wind stress
c	Sound speed
C_{CFL}	Courant number
f	Coriolis parameter
g'	Reduced gravity
L	Characteristic wind farm length
L_ρ	Rossby radius of deformation
M_{Ek}	Horizontal Ekman transport
N^2	Brunt-Väisälä frequency / buoyancy frequency
W_{Ek}	Vertical Ekman Pumping

Chapter 1

Introduction

1.1 Offshore Wind Energy

The global average temperature has increased by 1 degree Celsius since the late 1800s (NASA, 2024). According to NASA (2024), this rapid increase is mainly due to the emission of greenhouse gases from human activities, primarily the combustion of fossil fuels. In 2015 the United Nations (UN) adopted the Paris agreement (UNFCCC, 2024) to limit the increase of global temperature to a maximum of 2 degrees Celsius by 2100 compared to pre-industrial temperatures. The agreement obliges the UN nations to develop action plans to reduce their greenhouse gas emissions, with renewal every five years. The UN has also established 17 Sustainable Development Goals (SDGs) for all UN-nations to follow (UNA Norway, 2024). The overarching goal of the SDGs is to stop climate change and end poverty and inequality by 2030, while ensuring that the needs of both present and future generations are met.

Meanwhile, economic growth, elevated living standards, more extreme weather, a growing population, and new technology are closely followed by a rapid growth in electricity demand (IEA, 2024). According to a report by United Nations Environment Programme (2024), electricity production is the largest source of global greenhouse gas emissions. However, the report states that the power sector also holds the largest potential for emission reduction, with wind energy specifically highlighted as a proven and cost-competitive mitigation strategy.

Wind energy technology has existed for thousands of years; it has been used in food production, to propel boats, drain lakes, cut wood and pump water, before it was further developed to produce electricity (EIA, 2023). Today, offshore wind energy is one of the most rapidly growing renewable energy sources in Europe (NORCE, 2025). In fact, the largest operating bottom-fixed and floating wind farms are both located in Europe (WindEurope, 2022). With the United Kingdom, Denmark and the Netherlands being the biggest contributors, the total installed offshore wind capacity in Europe is approximately 30 GW, according to WindEurope (2022). As more countries follow and new technology is developed, the installed capacity is expected to increase in the upcoming years (WindEurope, 2022).

The Norwegian Continental Shelf and North Sea have one of the largest wind energy potentials in the world (Equinor, 2025b). Thus, despite already having the highest share of renewable energy out of any European country, with hydro and wind power accounting for 83% and 11% of the electricity production in 2023, it comes as no surprise that both the Norwegian government and industry show high interest in offshore wind energy (NVE, 2024; Norwegian Government, 2022a). Being a big exporter of fossil fuels, the Norwegian Government (2022a) aims to contribute to the European energy transition by increasing the export of non-fossil fuels with 50% by 2030 while decreasing the total greenhouse gas emissions with minimum 55%. Investing in offshore wind energy and becoming a world-leading nation is part of the governments plan to achieve this goal. This includes allocating areas corresponding to a total production of 30 GW within 2040 (Norwegian Government, 2022b). The bathymetry of the ocean areas around Norway is characterized by deep waters in several locations (Equinor, 2025a). This makes the area suitable for floating wind energy technology. Norwegian energy company Equinor is already a pioneer within offshore floating wind industry, operating approximately half of floating wind farms globally (Equinor, 2025a). This includes the worlds largest floating offshore wind farm (OWF), which is located in the North Sea, around 140 km off the west coast of Norway. It is called Hywind Tampen and was fully operational in 2023 (Equinor, 2024).

As described by Statkraft (2025), wind is a clean, renewable and widely available energy source. In addition, the technology has high efficiency, it is cost-effective, and requires little maintenance. Desalegn et al. (2023) highlights some challenges associated with wind energy. One of the challenges described is that wind is an intermittent energy source, especially onshore. Offshore wind velocities are higher and more stable and thus associated with a higher and more reliable power production. Desalegn et al. (2023) also states that, compared to onshore wind, offshore wind has less social and geographical constraints and is generally met with less stigma from the public.

However, several concerns have been raised in regards to the threat OWFs pose to the ocean environment. According to Naturvernforbundet (2025) and Palm et al. (2023), conflicts of interest include how noise and light from the turbines affect fish and mammals, the consequence of artificial reef-effect around the foundations and mooring lines, and the impact of turbines on fishing areas and bird migration patterns. Another concern, and the main focus of this thesis, is the effect of wind turbines on the upper ocean variability and biodiversity. This concern is described in detail by Paskyabi & Fer (2012), Raghukumar et al. (2023) and Palm et al. (2023); the wind turbines generate wakes that disturb and reduce the wind stress in the lee of the farm. As wind is one of the main drivers for upper ocean mixing, this can potentially further disturb ocean circulation patterns, vertical transport of heat, salinity and nutrients, and sound speed and primary production (i.e. photosynthesis conducted by phytoplankton (Sigman & Hain, 2012)), which in turn can affect entire ecosystems. It is still uncertain whether these disturbances will have a positive or negative impact on the ocean environment (Palm et al., 2023). This needs to be addressed as part of the further development of offshore wind energy.

1.2 Upper Ocean Variability

The ocean is in constant motion. The two main contributors to the ocean circulation are wind, and density gradients generated by differences in salinity and temperature (Wells, 2003). In addition to transporting heat and salinity, the ocean currents also transport nutrients that are essential for marine organisms and ecosystems (NOAA, 2011).

Plankton are defined by NOAA (2024b) as organisms that spend at least parts of their life-span floating or drifting at sea, unable to swim against the prevailing currents. Although they are microscopic in size, the entire ocean ecosystem depends on them as they deliver food and oxygen to a variety of species, starting with primary production (Turbeville, 2014). Figure 1.1 shows how plankton form the base of the ocean food webs and how plankton themselves feed on nutrients delivered via upwelling of cold and nutrient-rich water from the deep ocean (Turbeville, 2014).

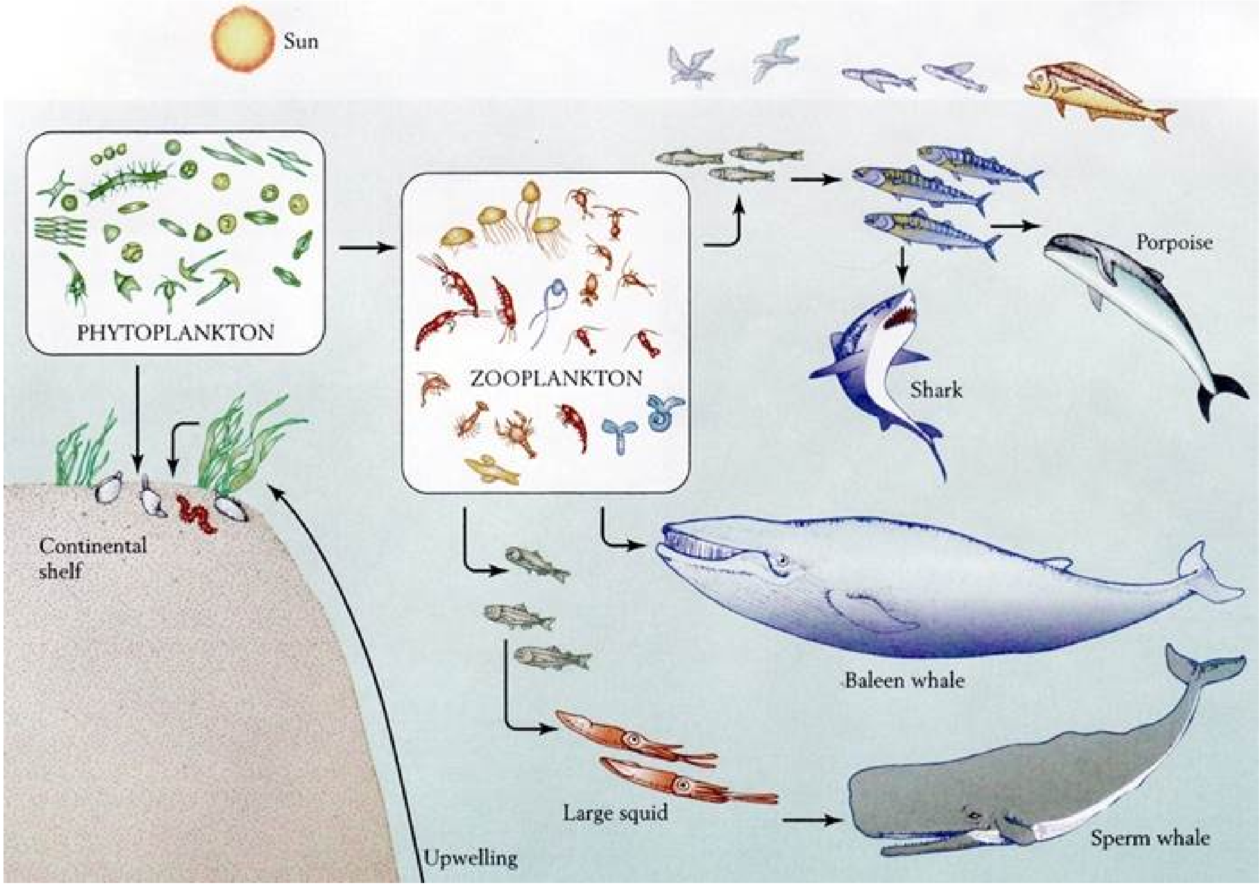

Figure 1.1: Plankton cycle. Plankton are the essential starting point of ocean food webs. Figure is from Turbeville (2014).

In order to protect and preserve the ocean, it is therefore valuable to emphasize the importance of understanding how OWFs will impact the upper ocean variability, including changes in upwelling patterns. Although this impact has been addressed before, more research is needed to obtain a more detailed understanding. As stated by Paskyabi (2015), this should include both theoretical, observational, and numerical studies. This increased knowledge can be further implemented when developing future OWFs, including the development of associated legal frameworks.

1.3 Objectives

According to de Jong et al. (2020), there are large knowledge gaps related to the effect of offshore wind energy on physical ocean conditions and marine biodiversity. Based on current available research, it is impossible to determine whether the cumulative impact on the environment is positive, negative, or neutral. More research is thus needed.

The main objective of this master's thesis is to use numerical modeling to investigate how changes in wind stress caused by the prevalence of OWFs will affect upper ocean variability and marine ecosystems. More specifically, the primary focus is on how the reduction of wind stress in the farm wake affects vertical mass transport and distribution of temperature and nutrients – and, in turn, how this influences near-surface sound speed and primary production in the nearby areas.

The study is based on idealized numerical experiments and is thus not site-specific. However, the WindSYS project led by the Institute of Marine Research (IMR), focusing on Hywind Tampen, was a key motivator and inspiration for the topic of this thesis. For context, brief descriptions are provided in appendix A, appendix B. The numerical model used is the advanced Regional Ocean Modeling System (ROMS). A simpler reduced-gravity model provided by Mostafa Bakhoday Paskyabi was also used for learning purposes in the early stages.

The thesis will directly or indirectly affect the following SDGs developed by the United Nations (2024):

- SDG 7: Affordable and clean energy
- SDG 13: Climate action
- SDG 14: Life below water
- SDG 8: Decent work and economic growth
- SDG 9: Industry, innovation, and infrastructure
- SDG 11: Sustainable cities and communities

1.4 State of the Art

Multiple numerical studies have been conducted with the aim of assessing the effect of OWFs on upper ocean variability, circulation, and biodiversity. With numerical modeling, the results are affected by the simplifications and assumptions made during model setup. This is also highlighted in the different studies.

The potential environmental impact of OWFs on the upper ocean circulation was first described by Broström (2008). He used simple analytical and numerical models to study how large wind farms disturb the wind stress patterns at the sea-surface and how this affects the upper ocean. He used a reduced-gravity model. In his study, he states that the circulation is driven more by spatial variations in wind stress (i.e. wind stress curl) than by the magnitude of the wind stress itself. Furthermore, he points to the strong horizontal shear that is a direct consequence of large wind farm wakes and to its association with convergence and divergence in the upper ocean. He also emphasizes that larger wind farms have greater impact on the ocean current than smaller wind farms, and that upwelling and downwelling will occur around the farm when the size exceeds the Rossby radius of deformation (term explained in chapter 2). He says it is likely that upwelling generated due to the presence of wind farms can affect both temperature patterns as well as the primary production and thus local ecosystems. He ends his article by stating that more studies, especially using realistic scenarios, are needed.

Paskyabi & Fer (2012) utilized numerical modeling to study the response of the upper ocean to wind farms in the presence of surface gravity waves. To model the geometry of the wind farm, a rigid rectangle with characteristic size L was used. In addition, an analytical two-dimensional U-shaped wake profile was applied to simulate a wind deficit downstream of the farm. To study the circulation within the simplified rectangular basin, the shallow-water equations were used. However, to make them more applicable to the setup, the equations were modified to include L, as well as both wind-wave and wave-current momentum transfer. To model the shallow-water equations, they used ROMS and a wave-modified finite volume technique, both of which gave agreeable results. In addition, they used a spectral wave model to generate wave forcing.

The results of Paskyabi & Fer (2012) showed that the response of the upper ocean to large wind farms is highly affected by wave forcing. As shown in Fig. 1.2, the amplitude of the pycnocline (term explained in chapter 2) displacement increases when wave forcing is included compared to when there are no wave forces acting. Fig. 1.3 shows the maximum value of pycnocline depth as a function of γ^2, i.e. the ratio between the Rossby deformation radius and L. Similarly, here it is shown that wave forcing amplifies the amplitude of the upper ocean response to wind farms. In this model, bottom frictional and non-linear effects were neglected.

Further, Paskyabi & Fer (2012) explains that the farm acts as a physical obstacle to the wind and waves, creating a lee region downstream of the wind farm. As shown in Fig. 1.4, this can create eddies that disturb the current and thereby affect the depth of the pycnocline. In the lower part of the lee region the pycnocline depth is increasing as a result of Ekman (term explained in chapter 2) divergence and upwelling. Similarly, in the upper part of the lee region the pycnocline depth is

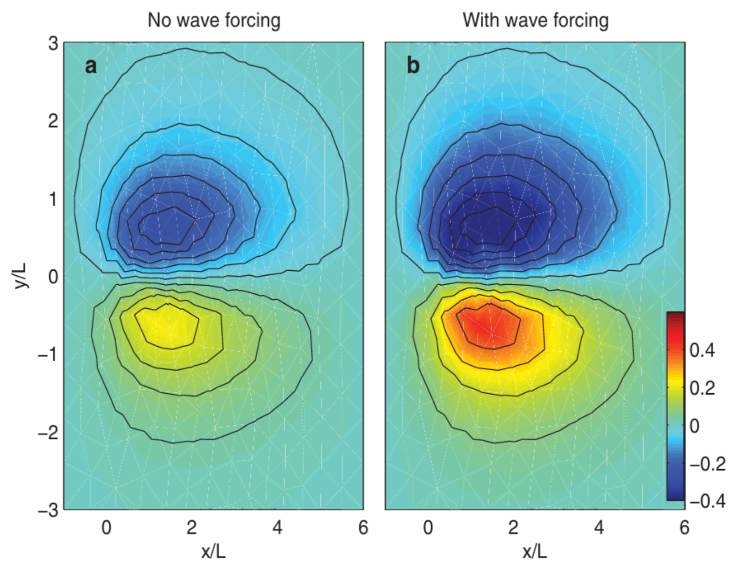

Figure 1.2: Rising and depression of the pycnocline. a) with no wave forcing. b) with wave forcing. Figure is from Paskyabi & Fer (2012).

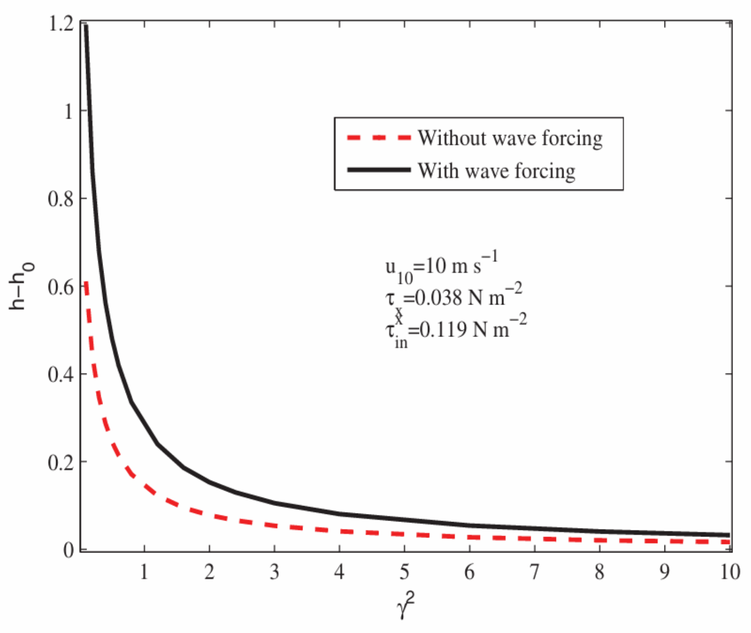

Figure 1.3: The maximum amplitude of the pycnocline depth as a function of Rossby deformation radius γ^2 with (—) and without (—) wave forcing. Figure is from Paskyabi & Fer (2012).

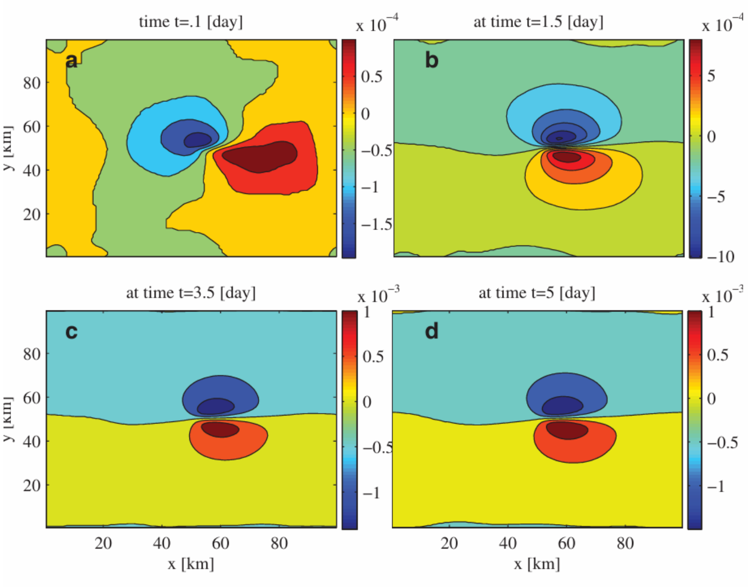

Figure 1.4: The temporal evolution of the pycnocline in the lee of the wind farm. The results are obtained using ROMS. Figure is from Paskyabi & Fer (2012).

decreasing due to Ekman convergence and downwelling. It can be seen that the response becomes weaker after about three days. This study is highly relevant, as wind turbines are constructed in areas with strong winds and large surface gravity waves. The study also emphasizes the importance of being aware of how simplifications may affect numerical results.

Paskyabi (2015) used numerical modeling to study how the deployment of multiple-turbine arrays in shallow water conditions can affect upper-ocean dynamical processes such as upper-ocean turbulent mixing, surface gravity waves, currents, stratification, and Ekman drifts. To predict the wake field behind each turbine, two empirical wake models (the Jensen wake model and the Larsen wake model) were used. In the first part, the farm geometry was assumed to be a rigid rectangle. Thereafter, a two-dimensional shallow water model was used to study the formation of vortex streets in the lee region of the wind farm. Lastly, a two-dimensional vertical ocean model was used to study the wind farm-upper ocean interaction, i.e., stratification, currents, and upwelling patterns. In this part, the farm geometry was assumed to be an array of multiple turbines.

To get a more detailed understanding on how wind farms affects coastal upwelling patterns for varying topography, the results of the two-dimensional ocean model were visualized by cross-sections of the distribution of the v-component of the ocean current as well as density anomalies. This is shown in Fig. 1.5 and Fig. 1.6, respectively. Here, open boundary conditions have been applied by Paskyabi (2015) for the offshore lateral boundary and wind stress is applied to the surface by a free stream velocity of 10 m/s normal to the xz-plane. The initial mixed layer has a density of 1025 kg/m^3 and the initial thickness is set to 10 m. The domain has a sloping bathymetry with depth ranging from 50-25 m over a horizontal distance of 100 km. In the upper panel of Fig. 1.5 and Fig. 1.6, the wind farm effect is excluded. In the middle panel, the wind farm is assumed to be a rigid body with $L = 5$ km located at 50 km in the x-direction. In the bottom panel, the wind

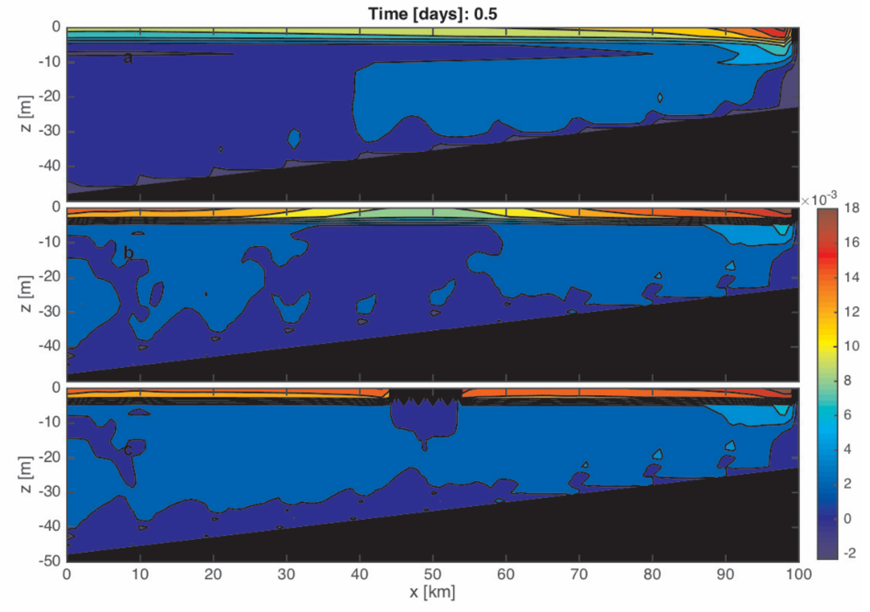

Figure 1.5: The distribution of the v-component of the ocean current with and without a wind farm present. Run time for simulation is 12 hours. a) The top panel represents no wind farm effect. b) The middle panel represents a rigid-body wind farm. c) The bottom panel represents a cluster wind farm and also includes the effect of surface gravity waves. Figure is from Paskyabi (2015).

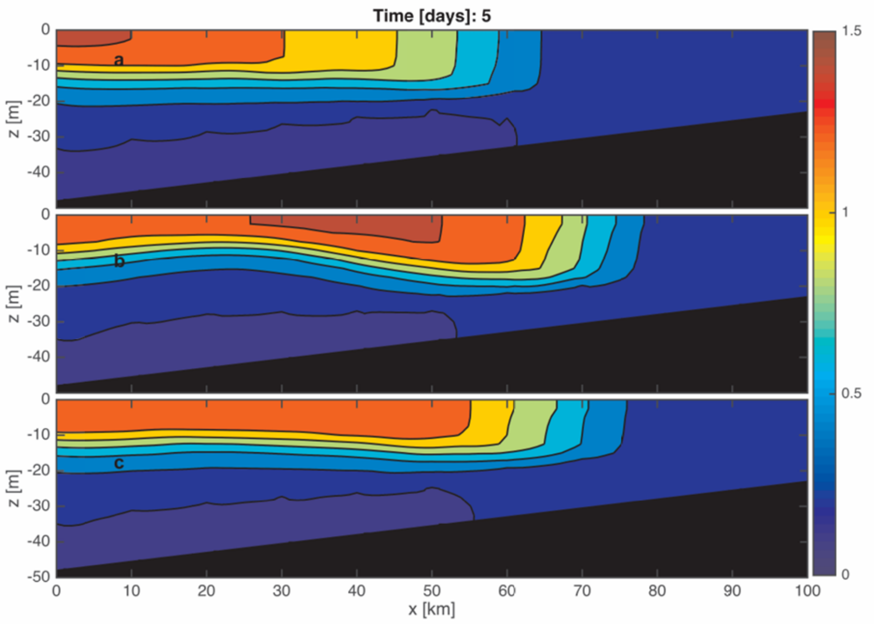

Figure 1.6: The distribution of density anomalies relative to 1025 kg/m^3, with and without find farm effects. Simulation runtime is 5 days. a) The top panel represents no wind farm effect. b) The middle panel represents a rigid-body wind farm. c) The bottom panel represents a cluster wind farm and also includes the effect of surface gravity waves. Figure is from Paskyabi (2015).

farm is located at 50 km and is made up of 5 turbines evenly spaced 1 km apart. In the bottom panel, the effect of surface gravity waves is included. In Fig. 1.5, the simulation is run for 12 hours. The results show that the efficiency and strength of the Ekman drift is affected by the wind farm, making the gradients stronger in the presence of the wind farm. In Fig. 1.6, the simulation is run for 5 days and show the density anomalies relative to 1025 kg/m^3. The results indicate that the Ekman drift at the ocean surface drives perturbations induced by the wind farm further down the water column. In turn, displacements of the horizontal flow and pycnocline oscillations are generated. The results also indicate that the presence of wind farms reduces the distance between the coast and the density outcrop. Paskyabi (2015) attributes this to farm-induced alterations of the Rossby radius of deformation, which is the characteristic length scale where the Coriolis effect is balanced by stratification/gravitation (Drange, 2024, p. 72).

Thus, the idealized numerical simulations conducted by Paskyabi (2015) indicate that the presence of wind farms can change the stratification pattern of the upper ocean with amplified upwelling and pycnocline oscillations compared to undisturbed regions.

Segtnan & Christakos (2015) used numerical modeling to study the impact of different wind farm designs on the vertical motion in the ocean. The studies of both Paskyabi & Fer (2012) and Paskyabi (2015) are idealized model experiments. Segtnan & Christakos (2015) wanted to make the study more realistic by using a wake model that takes the wind farm design (e.g. turbine configuration, rotor size and hub height) into account when calculating the wake effect and wind velocities. With the calculated wind field as forcing input, a ROMS model was applied over a period of 2 days to investigate the ocean response for two different wind farm designs. The vertical ocean velocities calculated by ROMS for the two cases were compared and discussed. The area of interest in this study is the Havsul area, situated off the Møre coast. As explained by Segtnan & Christakos (2015), the region has a documented potential for offshore wind energy production due to strong wind velocities. In addition, the area is associated with small islands, tall mountains, fjords, and chaotic bathymetry with a seafloor dominated by bed-rocks. For both wind farm design cases, the turbine diameter was set to 120 m and the height of the turbines was set to 90 m. The thrust coefficient was set to 0.4 and wake decay coefficient was set to 0.05. The free-stream velocity at 10 m above the surface was set to 20 m/s. Both wind farm designs consist of 70 turbines, however the placement of the turbines differs. For wind farm design 1, the turbines are placed in straight rows and columns. For wind farm design 2, the rows are curved. This is shown in Fig. 1.7.

To calculate anomalies of vertical velocities, wind stress and currents, Segtnan & Christakos (2015) used a control run as a reference value. The results of the calculated vertical velocity anomalies at 20 m depth are shown in Fig. 1.8. For both wind farm designs, the vertical velocity anomaly seems to increase with time with highest values Northwest of the farm. The increase is significantly greater for wind farm design 2, with values above 90 m/day after 24 hours. The vertical velocity anomaly for wind farm design 1 never exceeds 50 m/day. This indicates that the presence of wind farms alter the vertical velocities near the farm and that wind farm design does indeed have an influence on the upwelling and downwelling pattern in the local surrounding area. The wind stress anomaly is stable over the time period but approaches zero at the farm boundaries. This results in strong wind stress curl, and the curl depends on the wind farm design. In deep waters this kind of curl

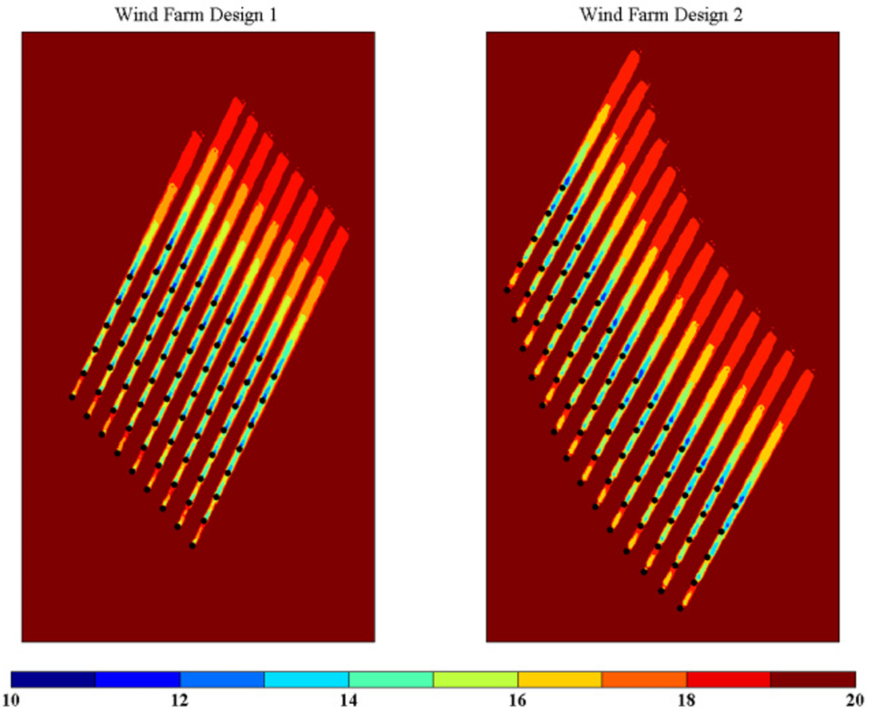

Figure 1.7: Wind farm design 1 to the left and wind farm design 2 to the right. Including wake fields behind the turbines. Figure is from Segtnan & Christakos (2015).

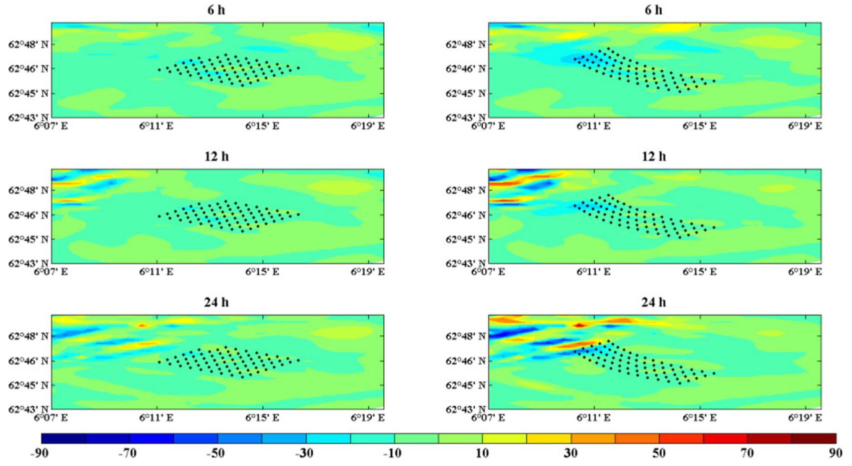

Figure 1.8: Vertical velocity anomaly at 20 m depth in the area surrounding the wind farm. The panels on the left belong to wind farm design 1 and the right panels belong to wind farm design 2. The black dots (—) represent the turbines. Figure is from Segtnan & Christakos (2015).

alteration combined with Ekman pumping (term explained in chapter 2) has the potential to affect the upwelling and downwelling regimes. Since the Havsul area is relatively shallow, Ekman pumping is according to Segtnan & Christakos (2015) thus not the main cause of the vertical velocity anomalies seen around the farm. The current anomalies give information about the horizontal velocity; the wind farm modifies the wind stress in the area. Reduced wind stress results in reduced ocean currents in the horizontal flow direction and vice versa. For wind farm design 2, the current anomalies west of the farm seem to increase after 12 h and 24 h. This agrees well with the vertical velocity anomalies seen at the same spatial and temporal location. In combination with strong bathymetry gradients, this indicate that the vertical motion in the Havsul area is driven mainly by wind farm-driven changes in the horizontal flow field over varying topography rather than Ekman pumping. Wind farm design 2 showed greater impact on the vertical motion than wind farm design 1 due to stronger wind curl and flow variations.

The results of this study by Segtnan & Christakos (2015) show that wind farm design can affect vertical velocity, wind stress, and upwelling and downwelling patterns. This is important to keep in mind when working with numerical modeling as it shows how idealized models can omit important information that can have a great impact on the environment and the installation process of new OWFs.

Raghukumar et al. (2023) used a numerical atmosphere-ocean circulation model and ROMS to study changes to upwelling patterns in the presence of offshore wind farms. The main objective was to determine how farm-induced wind stress reduction affect the upwelling pattern and thus nutrient delivery. The area of interest was the California Coast, more specifically Humboldt, Morro Bay and Diablo Canyon. As stated by Raghukumar et al. (2023), wind-driven upwelling is very important for the ecosystem in these areas. Close to the coast, upwelling is driven by Ekman transport with associated coastal divergence due to Northwesterly winds. Farther offshore, upwelling is driven by wind stress curl, i.e. horizontal wind gradients that create divergence. This latter type of wind-driven upwelling can extend 100-200 km farther offshore than coastal upwelling.

The model run time was set to 25 years, from 1988-2012. Raghukumar et al. (2023) found that the presence of wind farms disturbs the wind stress gradient across the shore. The result is a decrease in upwelling on the side closest to the coast and an increase in upwelling on the offshore side of the farm. It is mainly the wind stress curl-driven upwelling that is affected by the wind farm. Coastal upwelling experienced little change. If looking across all three locations, the net upwelling is almost constant with or without the farm present. However, for smaller-scale areas, the upwelling pattern is disturbed by the wind farm. Further studies are needed to determine the impact this could have on marine ecosystems.

Chapter 2

Theory

2.1 Wind Energy Fundamentals

2.1.1 Wind

Wind is driven by pressure gradients created by uneven solar heating across regions with different terrain and latitude (Ehrlich, 2013, p. 185). The physical explanation is that air flows from high-pressure areas to lower-pressure areas trying to erase the gradients (Marshall & Plumb, 2008, p. 73). The result is wind. Thus, wind energy is an indirect form of solar energy (Ehrlich, 2013, p. 185).

Due to the rotation of the Earth, the wind is deflected by the Coriolis effect towards the right on the Northern hemisphere and towards the left on the Southern hemisphere (Marshall & Plumb, 2008, p. 95-96). Surface friction also causes the wind to deflect slightly towards lower pressures close to the ground (Marshall & Plumb, 2008, p. 129-135).

Wind contains kinetic energy that can be harvested by wind turbines. According to Ehrlich (2013), the global annual accessible potential of wind energy is estimated at 300 million GWh. Ehrlich (2013) also states that this is equivalent to approximately 20 times the current global electricity demand.

2.1.2 Energy Extraction by Wind Turbines

Taking advantage of the enormous potential of wind energy requires an understanding of fundamental mechanical principles.

First, as explained by Ehrlich (2013), lets imagine a cylindrical mass flow of air with length Δx, base area A and velocity v approaching a wind turbine with a swept area A, as shown in Fig. 2.1. The kinetic energy of the moving air mass is given by Ehrlich (2013) as:

$$\Delta E = \frac{1}{2}mv^2 = \frac{1}{2}\rho A \Delta x v^2 = \frac{1}{2}\rho A \Delta t v^3 \tag{2.1}$$

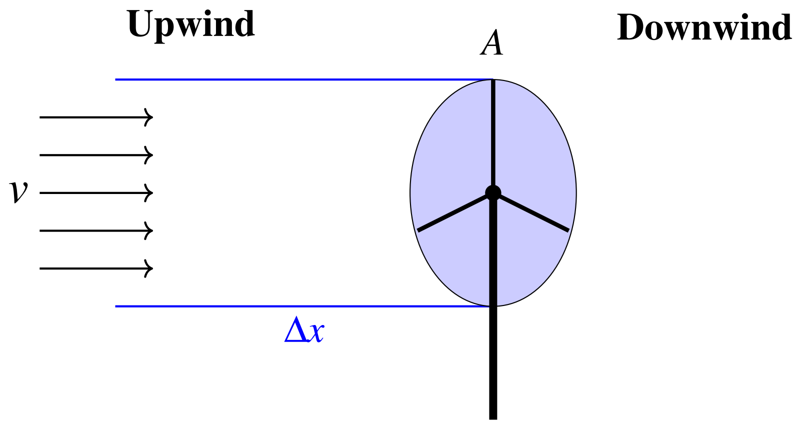

Figure 2.1: A cylindrical air mass with velocity v and length Δx is approaching a wind turbine with a swept area A. Power is extracted from the wind by the wind turbine. Figure is adapted from Ehrlich (2013).

Furthermore, Ehrlich (2013) explains that dividing both sides of Eq. (2.1) by Δt gives the following expression for the power distributed over the area:

$$P_{wind} = \frac{1}{2}\rho A v^3 \tag{2.2}$$

However, the amount of power extracted from the wind by the wind turbine is limited by the power coefficient C_p. The final expression for the maximum power that can be extracted is thus given by Ehrlich (2013) as:

$$P = C_p \frac{1}{2}\rho A v^3 \tag{2.3}$$

The value of C_p ranges from 0 to a maximum of 59.3%, known as Betz limit. This is a theoretical maximum derived using the 1D momentum theory (actuator disc theory), which is a widely applied method that explains how efficiently wind turbines extract kinetic energy from the wind and how this process affects the air flow upwind and downwind of the turbine (Burton et al., 2021). The theory is based on the conservation of mass, momentum and energy. For modern wind turbines, C_p is typically between 40-50% (Ehrlich, 2013; Burton et al., 2021).

From Eq. (2.3) it is clear that the power extracted from the wind is mostly dependent on the magnitude of the wind speed. This is part of the reason why wind energy is associated with a high level of intermittency (Ehrlich, 2013). Eq. (2.3) also shows that the swept area is another parameter of importance for the power output. Hence, the diameter of commercial wind turbine rotors have increased from 50 m in 1995 to 220 m in 2020 (Burton et al., 2021, p. 7).

2.1.3 Wake Effect

Continuing the 1D momentum theory (actuator disc theory) from Burton et al. (2021) discussed in section 2.1.2, lets now look at a steady and incompressible cylindrical flow with free-stream velocity v_∞, as shown in Fig. 2.2a; as the flow approaches the turbine, the velocity will be reduced to v. Following conservation of mass and Eq. (2.1), this reduction in kinetic energy implies that the diameter of the cylindrical flow must expand (Burton et al., 2021). As no work has been exerted by the air yet, the conservation of energy and Bernoulli's principle implies that the static pressure will increase to compensate for the kinetic energy loss (Burton et al., 2021). This is shown in Fig. 2.2b.

Figure 2.2b also shows that there is a sudden drop in static pressure between the inlet and outlet of the turbine. As explained by Burton et al. (2021), this pressure difference creates a thrust force acting on the turbine by the fluid. As the air flow passes through the turbine, kinetic energy is extracted and the velocity of the flow is reduced. Conservation of momentum implies that the change of momentum across the turbine must be balanced by the thrust force applied by the pressure difference across the turbine (Burton et al., 2021). Downwind of the turbine, both the static pressure and air flow velocity are reduced. After a while, the static pressure slowly returns to atmospheric levels, causing a further decrease in the air flow velocity and expansion of the flow diameter. This can be seen in Fig. 2.2. As explained by Krutova et al. (2020) and Krutova (2024), this part of the flow is called the wake, and is characterized by reduced mean wind velocity and increased turbulence intensity. Far downwind, the wake velocity will eventually return to free-stream velocity.

If a turbine is placed within the wake area of another turbine, the downwind turbine can experience both reduced energy production and increased mechanical fatigue due to increased turbulence within the wake (González-Longatt et al., 2012). It is therefore important to include the wake effect when designing and developing wind farms to optimize energy production and minimize mechanical stresses on the turbines.

The length scale of the wake, i.e. how far the wake extends behind the farm, is dependent on atmospheric conditions and the size and layout of the wind farm; instable atmospheric conditions are accompanied by strong mixing and the wake dissipates fast, not allowing it to extend very far (Rivera-Arreba et al., 2023). Similarly, stable atmospheric conditions are accompanied by weak mixing and the wake can take long to dissipate, allowing the wake to extend for several tens of kilometers (Lian et al., 2022). The extent of the wake effect has raised some concern in regards to large offshore wind energy projects due to potential disturbances of wind-driven ocean circulation (Paskyabi & Fer, 2012). This will be further discussed in section 2.2.

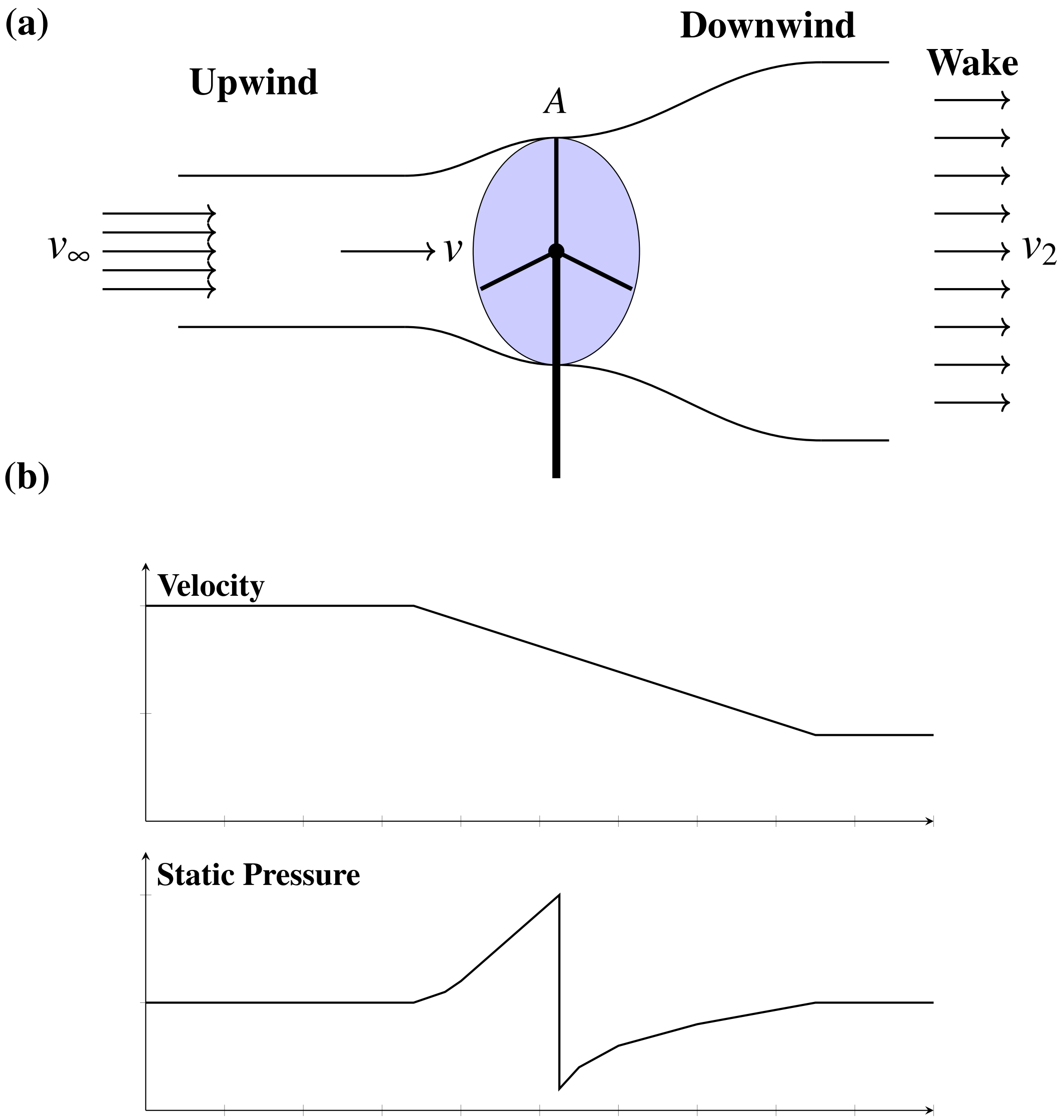

Figure 2.2: a) A cylindrical air mass with free-stream velocity u_∞ is approaching a wind turbine with a swept area A. Energy is extracted from the wind by the wind turbine, causing a decrease in the velocity v_2 downwind. In addition, the downwind base area increases following conservation of energy, momentum and mass. Figure is adapted from Ehrlich (2013). b) In front of the turbine, the velocity decreases and the static pressure increases. Across the turbine, there is a drop in static pressure. In the wake behind the turbine, the velocity is decreased and the static pressure returns to atmospheric pressure. Figure is adapted from Burton et al. (2021).

2.2 Ocean Dynamics and Properties

The ocean circulation is driven by two main processes. The first process is wind stress exerted at the ocean surface and the second process is convection due to variations in salinity and temperature (Marshall & Plumb, 2008). These two processes will be presented and discussed in this chapter.

2.2.1 Physical Properties and Stratification of the Ocean

Density, Salinity and Temperature

The ocean has many unique characteristics that can be described using parameters such as temperature, salinity and density.

The density of sea water is mainly determined by temperature and salinity; salinity is the main determinant for density in high-latitude regions, whereas temperature is typically the primary determinant of density elsewhere (Talley et al., 2011a).

According to Talley et al. (2011a), the temperature of the ocean ranges from approximately $-1.7°$C to 30°C. Talley et al. (2011a) also explains that warmer water has a lower density than cold water due to thermal expansion caused by increased molecular activity.

The ocean salinity varies spatially depending on e.g. evaporation and freshwater dilution from i.e. river runoffs and recomputation (Talley et al., 2011a). The mean ocean temperature is 3.5°C and the mean ocean salinity level is 34.6 psu (Talley et al., 2011b). The open ocean density ranges from around 1021 kg/m^3 at the sea-surface to around 1070 kg/m^3 at the deepest depth (Talley et al., 2011a). As water with higher density tends to sink and water with lower density tends to float, the density of the different water masses is important for the horizontal layering of the ocean, also known as ocean *stratification*.

Ocean Stratification

Static stability of the ocean is related to the vertical density stratification. This is described by Talley et al. (2011a); strongly stratified water columns are more statically stable and harder to mix, and weakly stratified water columns are more statically unstable and easier to mix. The Brunt-Väisälä, or buoyancy frequency is often used to describe the static stability of the water column, and is given by Talley et al. (2011a) as:

$$N^2 = -\frac{g}{\rho}\frac{\partial \rho}{\partial z}, \tag{2.4}$$

where g is gravitational acceleration; ρ is density; z is depth of the water column. As seen from Eq. (2.4), the buoyancy frequency increases with static stability and decreases with static instability.

The typical ocean density profile consists of different layers with different levels of stratification, as shown in Fig. 2.3. The upper-most layer is called the surface mixed layer (Talley et al., 2011a). This layer plays an important role in the exchange and transport of e.g. heat and carbon between the atmosphere and the deep ocean (Sallée et al., 2021). As explained by Talley et al. (2011a), the surface mixed layer has a weak stratification due to strong mixing caused by e.g. solar, wind and wave forcings. In this layer, the salinity, temperature and density is therefore close to uniform. Below the mixed layer, there is a strongly stratified layer called the *pycnocline*. As explained by Talley et al. (2011a), the pycnocline is characterized by strong vertical temperature and salinity (density) gradients that have a stabilizing effect on the layer. In other words, the highly stable pycnocline acts as a physical barrier by inhibiting vertical transport between the mixed layer and the deep ocean. Similarly to the mixed layer, the deep layer is characteristic by weak stratification (Talley et al., 2011a).

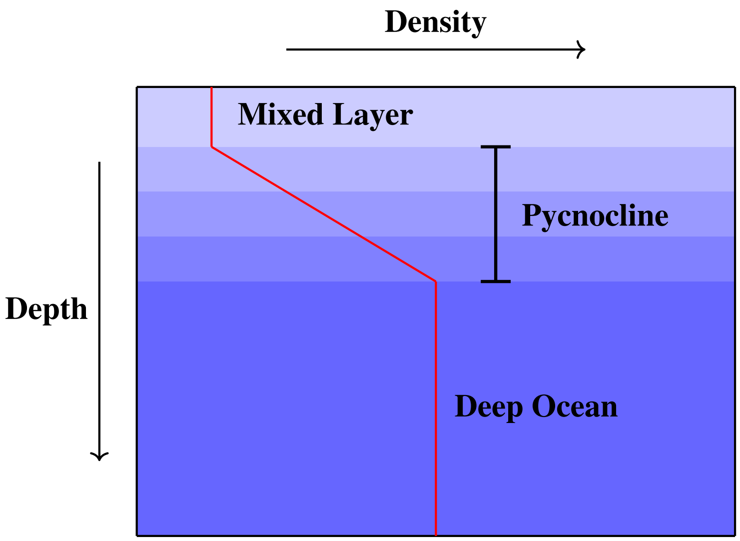

Figure 2.3: Density profile of a stable stratified ocean is shown in red (—). The density is approximately constant in the mixed layer and deep ocean, and rapidly increasing in the pycnocline. The strongly stratified pycnocline acts as a barrier to vertical transport between the weakly stratified layers above and below. Figure is adapted from Webb, Paul and Roger Williams University (2025) and based on theory from Talley et al. (2011a).

The ocean-atmosphere interaction at the ocean surface causes the thickness of the different ocean layers to vary throughout the year. This is described by Talley et al. (2011b); depending on the level of stratification and on surface forcings such as solar radiation, wind stress and breaking of internal waves, there will be different amounts of turbulence (either mechanical or buoyancy-driven) in the surface layer and thus different amounts of mixing. During summer, stabilizing heat fluxes and weak wind conditions typically result in weak mixing and thus a thinning of the mixed layer will occur. Similarly, destabilizing heat loss and strong wind conditions during winter typically result in strong mixing and thus a thickening of the mixed layer.

In a similar manner, the pycnocline stratification is stronger during summer and weaker during winter (Sallée et al., 2021). As briefly implied above, any alteration of the pycnocline stratification will lead to corresponding changes in the exchange rates between the surface mixed layer above and the deep ocean below; a weakening of the pycnocline stratification will result in an increased exchange rate and a strengthening of the pycnocline stratification will result in a decreased exchange rate (Sallée et al., 2021).

In addition to representing a strong density gradient, the pycnocline is by Longhurst (2007) described as a transition zone where nutrients, light from solar radiation and biological activity change significantly. The pycnocline is nutrient-rich and home to a characteristic group of plankton organisms (Longhurst, 2007). Since most of the primary production in the ocean occurs in the surface mixed layer, the concentration of nutrients, such as nitrate, gradually decreases upward through the pycnocline as primary production and chlorophyll biomass increase (Sallée et al., 2021; Longhurst, 2007). Zooplankton are often found in dense populations at depths where algal growth is high (Longhurst, 2007). Zooplankton also follow a typical diurnal cycle of movement across the pycnocline due to different light conditions (Longhurst, 2007; NOAA, 2024b). This will be further discussed in section 2.2.4.

It is quite apparent that modifications of the pycnocline may have significant consequences on both the global climate and marine ecosystems (Sallée et al., 2021). Assessing the physical changes in the pycnocline stratification is therefore critical when developing new offshore technology to determine its impact on the upper ocean variability and biodiversity. This would be of interest by many different stakeholders.

Another phenomenon that affects the ocean stratification in the upper 100 m or so, is the Ekman response to wind forcing (Talley et al., 2011b,c; Marshall & Plumb, 2008). As explained by Talley et al. (2011b), the Ekman velocities are affected by surface turbulence, but are too weak to generate any turbulence and mixing themselves. Thus, the Ekman response has no direct effect on the mixed layer depth and is also independent of the mixed layer stratification (Talley et al., 2011b). Instead, the Ekman velocities are responsible for the large-scale dynamical phenomenons known as upwelling and downwelling (Talley et al., 2011b,c). The curl-driven vertical Ekman pumping generated by local ocean surface wind stress also affects the pycnocline depth (Longhurst, 2007). These Ekman dynamics will be further discussed in section 2.2.3.

2.2.2 Dynamical Properties of the Ocean

This chapter is based on Marshall & Plumb (2008).

Coriolis Effect

The Earth is constantly rotating around its own axis with an angular velocity of 7.27×10^{-5} s^{-1}. To study large-scale ocean dynamics, it is therefore useful to use a rotating coordinate system. This introduces the Coriolis effect, which is a fictional acceleration that describes how otherwise linear motions get deflected in a rotating coordinate system versus in a non-rotating coordinate system. The Coriolis acceleration is given as:

$$2\Omega \times \mathbf{u} = f\hat{\mathbf{z}} \times \mathbf{u}, \tag{2.5}$$

where Ω is the angular velocity of the Earths rotation; $\mathbf{u}$ is the velocity vector, $\hat{\mathbf{z}}$ is the z-direction unit vector; f is the Coriolis parameter given as:

$$f = 2\Omega \sin\varphi, \tag{2.6}$$

where φ is the given latitude. As seen from Eq. (2.6), the Coriolis parameter is positive in the Northern hemisphere and negative in the Southern hemisphere, and decreases towards the equator. From Eq. (2.5) and following the right-hand vector rule of mathematics, the Coriolis acceleration is acting 90 degrees to the right and left of the flow direction on the Northern and Southern hemisphere, respectively.

Rossby Radius of Deformation

The Rossby radius of deformation is a characteristic horizontal length scale that describes at which length scale rotational effects is balanced by the effects of stratification, i.e. gravitational forces. It gives the length scale of eddies in he ocean and is given as:

$$L_\rho = \frac{\sqrt{g'H}}{f} = \frac{NH}{f}, \tag{2.7}$$

where H is the depth of the water column; f is the Coriolis parameter; N is the buoyancy frequency; g' is reduced gravity given as:

$$g' = g\frac{\Delta\rho}{\rho_1} = g\frac{\rho_1 - \rho_2}{\rho_1}, \tag{2.8}$$

where g is gravitational acceleration; ρ is density. Eq. (2.7) indicates that the Rossby radius of deformation decreases towards the poles and increases towards the equator.

2.2.3 Ekman Dynamics

The Ekman theory considers an open ocean area and is based on the assumption of geostrophic balance, but includes the effect of surface wind stress (Marshall & Plumb, 2008; Drange, 2024). This chapter is based on Marshall & Plumb (2008) and on the summary of Marshall & Plumb (2008) written by Drange (2024).

Ekman Layer

Wind exerts wind stress, i.e. mechanical friction on the ocean surface that generates motion in the upper parts of the water column. The wind stress is given as:

$$|\tau| = \rho_{\text{air}} C_D u_{10m}^2, \tag{2.9}$$

where ρ_{air} is air density; C_D is a friction coefficient; u_{10} is the wind velocity at 10 m height. The wind stress is aligned with the direction of the wind.

The layer directly affected by wind stress is called the Ekman layer, and is typically confined to the upper 10-100 meters of the ocean, depending on the magnitude of the wind stress. The unit of wind stress is N/m^2, i.e. force per unit area, and the magnitude of the wind stress gradually diminishes to zero down the water column, as shown in Fig. 2.4. Consequently, the net wind stress across a given layer can be expressed as:

$$F_x = \frac{1}{\rho_{\text{ref}}} \frac{\partial \tau_x}{\partial z}, \tag{2.10}$$

where ρ_{ref} is the uniform density of the layer; $\partial \tau_x$ is the wind stress gradient ; ∂z is the thickness of the layer.

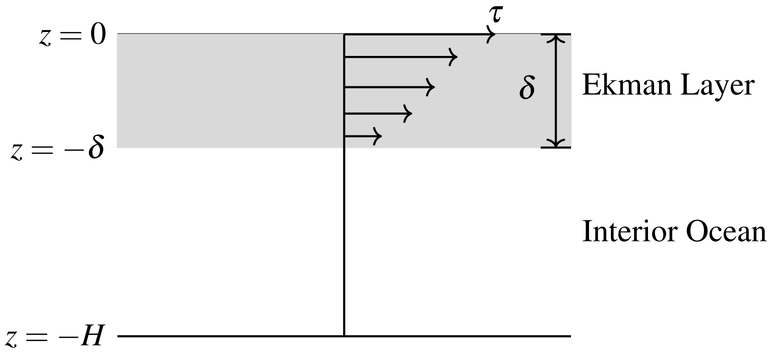

Figure 2.4: The wind stress τ decays to zero at depth $z = -\delta$. The layer directly affected by the wind stress is called the Ekman layer. Figure is adapted from Marshall & Plumb (2008).

Ekman Transport

To account for the effect of wind stress, the horizontal velocity is split into a geostrophic part u_g and an ageostrophic part u_{ag}. Following this, the horizontal momentum equation can be written as:

$$\begin{aligned} \frac{1}{\rho_{\mathrm{ref}}}\nabla p + f\hat{\mathbf{z}} \times \mathbf{u}_g &= 0 \\ f\hat{\mathbf{z}} \times \mathbf{u}_{ag} &= \frac{1}{\rho_{\mathrm{ref}}}\frac{\partial \tau}{\partial z}, \end{aligned} \tag{2.11}$$

where ρ_{ref} is the uniform density of the layer; Δp is the pressure gradient; f is the Coriolis parameter; $\frac{\partial \tau_x}{\partial z}$ is the variation of wind stress across the layer with thickness δz.

Next, an expression for Ekman transport, i.e. net horizontal mass transport over the Ekman layer, can be obtained by multiplying the ageostrophic part of Eq. (2.11) by ρ_{ref} and integrating it across the Ekman layer:

$$\mathbf{M}_{\mathrm{Ek}} = \frac{\tau_{\mathrm{wind}} \times \hat{\mathbf{z}}}{f}, \tag{2.12}$$

where τ_{wind} is the wind stress; f is the Coriolis parameter; $\hat{\mathbf{z}}$ is a upward-pointing unit vector.

Following the right-hand rule of vector mathematics, Eq. (2.12) shows that the net horizontal Ekman transport is directed 90 degrees to the right of the wind stress on the Northern hemisphere ($f > 0$) and 90 degrees to the left of the wind stress on the Southern hemisphere ($f < 0$). This result was shown in terms of the Ekman spiral by Vagn Waldrif Ekman in 1905.

Ekman Spiral

Due to the Coriolis force, the wind-driven motion of the water masses at the ocean surface will deflect towards the right (left) in the Northern (Southern) hemisphere. The second layer in the water column will be affected by both the current of the in-motion layer above and the still layer below. These two layers have opposite effects; the above layer generates motions while the layer below prohibits motion to be generated. In addition, the Coriolis effect will further deflect the current. As shown in Fig. 2.5, the result will be a current that is both weaker and more deflected than the above current. This process is called the Ekman spiral and will continue to occur down the water column until the velocity of the current reaches zero. The sum of all the Ekman currents velocity vectors creates the Ekman transport that is directed exactly perpendicular to the wind stress.

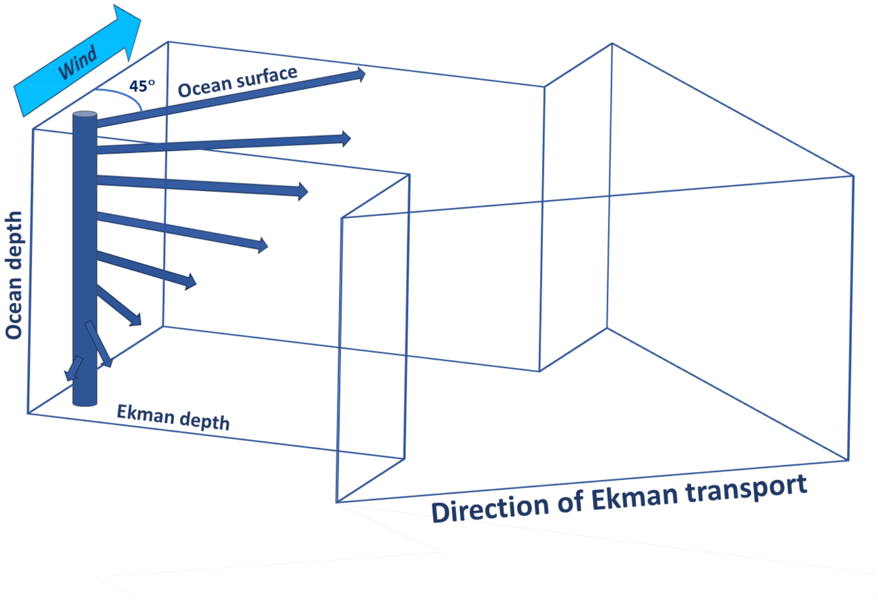

Figure 2.5: Wind stress at the ocean surface creates surface currents that are deflected by the Coriolis force. The currents are dragging along the water below, creating the Ekman spiral extending down the water column. The sum of the Ekman currents velocity vectors is the Ekman transport that is directed perpendicular to the surface wind direction. Figure is adapted from Talley et al. (2011c) and Marshall & Plumb (2008).

Ekman Pumping: Downwelling and Upwelling

Even though the wind stress has a direct frictional effect only on the Ekman layer, circulation will occur throughout the entire water column due to wind-driven convergence and divergence of Ekman transport in the surface layer.

Assuming incompressible flow and constant f, geostrophic flow can be considered horizontally nondivergent ($\nabla_h \cdot \mathbf{u}_g = 0$), and the continuity equation can be written as:

$$\nabla_h \cdot \mathbf{u}_{ag} + \frac{\partial w}{\partial z} = 0, \tag{2.13}$$

where $\nabla_h = \hat{\mathbf{x}}\partial/\partial x + \hat{\mathbf{y}}\partial/\partial y$; $\mathbf{u}_{ag}$ is the ageostrophic flow; w is vertical velocity component.

Eq. (2.13) shows that ageostrophic flow is not horizontally nondivergent. Instead, wind-driven convergence or divergence of Ekman transport at the ocean surface will drive a vertical motion with velocity w. Whenever the Ekman transport results in divergence of water, water from the ocean depth will be pumped up towards the surface. This is called upwelling. The opposite effect is called downwelling, and happens whenever Ekman transport is followed by convergence of water.

Integrating Eq. (2.13) across the Ekman layer and assuming $w = 0$ at the ocean surface, the magnitude of the vertical Ekman pumping is given as:

$$w_{\mathrm{Ek}} = \frac{1}{\rho_{\mathrm{ref}}} \nabla_h \cdot \mathbf{M}_{\mathrm{Ek}} = \frac{1}{\rho_{\mathrm{ref}}} \left(\frac{\partial}{\partial x} \frac{\tau_{\mathrm{wind},y}}{f} - \frac{\partial}{\partial y} \frac{\tau_{\mathrm{wind},x}}{f} \right) \tag{2.14}$$

As indicated in Eq. (2.14), the vertical Ekman velocity is highly dependent on the wind stress curl $\left(\frac{\partial \tau_y}{\partial x} - \frac{\partial \tau_x}{\partial y}\right)$; a positive curl (anti-clockwise direction) creates divergence and upwelling, whereas a negative curl (clockwise direction) creates convergence and downwelling. This is illustrated in Fig. 2.6. Based on this theory, it is apparent that disturbances of the wind field, e.g. from the wake behind a wind turbine, can influence the vertical mass transport, including upwelling patterns.

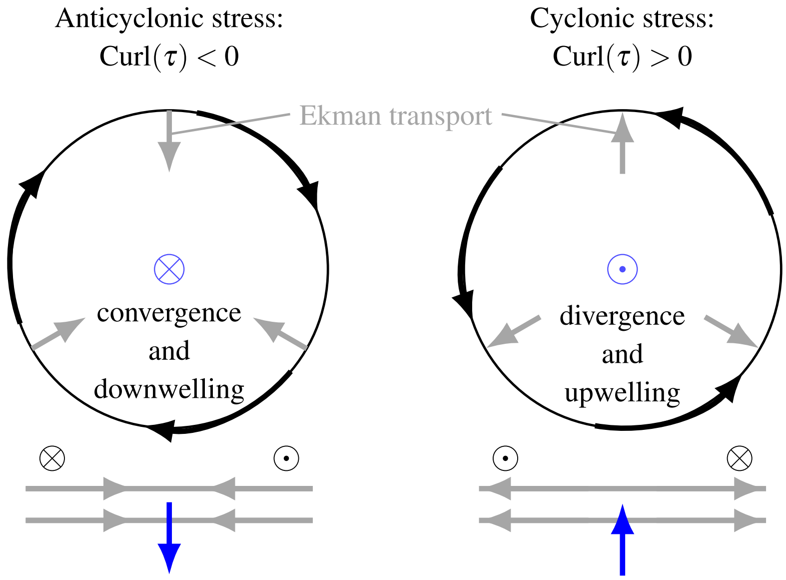

Figure 2.6: Ekman pumping. Ekman transport is directed perpendicular to the wind stress. For positive wind stress curl (anti-clockwise direction), the Ekman transport generates divergence and upwelling. For negative wind stress curl (clockwise direction), the Ekman transport generates convergence and downwelling. Figure is adapted from Marshall & Plumb (2008).

2.2.4 Biological Properties of the Ocean

Biological Tracers

This section is based on theory described by Talley et al. (2011a).

Tracers are dissolved properties that can be used to track water masses and flow patterns in the ocean. A tracer is conservative if changes in concentration are mainly due to ocean mixing. This includes salinity, temperature, and density. If, however, changes in the concentration are due to chemical reactions or biological processes, the tracer is non-conservative. Examples of non-conservative tracers are dissolved oxygen, nutrients, plankton, dissolved inorganic and organic carbon, alkalinity and pH.

Oxygen enters the upper ocean via the atmosphere and through photosynthesis by phytoplankton. Therefore, the oxygen concentration is high on the ocean surface. Oxygen is then removed from the ocean through respiration by zooplankton, in addition to other ocean animals, such as bacteria that live further down the water column where no oxygen is produced. Therefore, the oxygen concentration rapidly decreases with depth below the mixed layer.

Nutrients include dissolved silica, phosphate, and nitrogen compounds such as ammonium, nitrate and nitrite. One of the characteristics of the upper ocean is the abundant marine life. Marine species need nutrients to survive and thrive. Thus, due to high consumption, nutrient concentrations are low in the upper ocean. When the organisms die, they sink towards the sea bed. On the way down, bacterial activity will cause the detritus to break down into ammonium and phosphate molecules. Nitrifying bacteria will then use oxygen to make nitrite and nitrate from ammonium molecules. Some organisms also use silica in their protective shells. When the organisms die and sink towards the sea floor, the shells eventually dissolve, and the silica re-enters the water columns. The nutrient concentration is therefore increasing down the water column.

Upwelling and Biological Activity

Nutrient supply and chemical cycles in the upper ocean layer are dependent on physical processes such as, e.g., upwelling and downwelling (Holt et al., 2009; Talley et al., 2011b). As further described by Talley et al. (2011b), areas with upwelling are characterized by higher biological activity in the ocean surface and vice versa. In addition, downwelling is important for the downward transport of detritus and carbon from the surface towards the deeper ocean (Holt et al., 2009).

The water that is pumped up from ocean depth during upwelling is usually cold and nutritious (Talley et al., 2011c). The nutrients that reach the upper ocean are then eaten by plankton and form the base of the ocean food webs (Miller et al., 2022). The process is shown in Fig. 2.7. Plankton populations tend to grow rapidly in upwelling zones, creating diverse and rich ecosystems suitable for, e.g., fisheries (UCAR, 2025).

The word *plankton* originates from Greek and means “drifter“ or “wanderer“ (NOAA, 2024b). As further explained by NOAA (2024b), this is a fitting name, as plankton are tiny organisms carried by ocean currents and tides, unable to swim against prevailing forces. Some organisms remain plankton

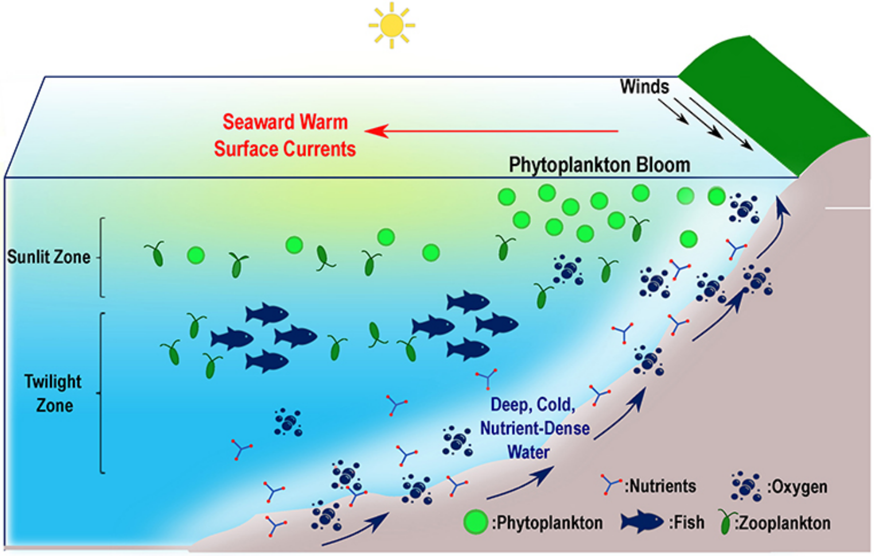

Figure 2.7: Ocean food chain. Plankton are the essential starting point of ocean food webs. They feed on nutrients brought to them via upwelling. Figure is from Miller et al. (2022).

throughout their life span, while others are plankton only for a shorter period before developing the ability to swim against the currents (NOAA, 2024b).

As described by NOAA (2024b), plankton can be classified in multiple different ways, e.g. by type, size, and drifting time. However, the most common way of classifying plankton is by differentiating between phytoplankton and zooplankton NOAA (2024b).

Phytoplankton are microscopic plants (NOAA, 2024a). They contain chlorophyll for performing photosynthesis and are therefore often found near the ocean surface where solar radiation penetrates (NOAA, 2024b). Around 89% of the oxygen we breathe is generated by phytoplankton (Jakobsen & IMR, 2024). In addition, phytoplankton produces proteins, fats and carbohydrates from inorganic nutrients like phosphates, sulfur and nitrates (NOAA, 2024a).

Zooplankton are microscopic animals, e.g., krill and pelagic worms (NOAA, 2024b). According to NOAA (2024b), zooplankton feed on phytoplankton, and bigger animals, e.g. whales, feed on zooplankton. This interaction causes a typical diurnal cycle of movement; during the night, zooplankton drift toward the surface to feed on phytoplankton. Then, to hide from predators, zooplankton tend to drift into deeper waters during daytime. This migration is so significant and widespread it can be observed from space (NOAA, 2024b).

It is clear that both phytoplankton and zooplankton are important links in the food chain in the ocean as well as for the global environment. As highlighted by NOAA (2024b,a), it is however important to note that plankton are very sensitive to environmental changes; even small changes in temperature, pH, salinity and nutrient concentration can have a big impact on plankton. Both a too high and a too low nutrient access can have a negative impact on marine ecosystems. Excessive nutrient levels can cause harmful algal blooms, and low levels can lead to food shortage throughout the food chain (NOAA, 2024b,a). Because upwelling and downwelling are wind-driven circulations (Marshall &

Plumb, 2008; Talley et al., 2011b,c), disruptions of the wind field at the ocean surface have the potential to affect plankton.

In a wind farm, wake generation disturbs the wind field and reduces the wind stress behind the turbine (González-Longatt et al., 2012; Krutova et al., 2020; Lian et al., 2022). Multiple studies have been conducted on how the presence of OWFs affect the vertical mass transport and the biodiversity. Although all studies show that large-scale OWFs affect primary production, the results are contradictory in terms of whether the impacts are positive or negative (Palm et al., 2023). According to the findings of Christiansen et al. (2022b) and Christiansen et al. (2022a), the wake effect reduces the wind stress behind the turbines, resulting in a weaker mixing and stronger stratification. This can cause decreased primary production (Palm et al., 2023). However, the findings of Floeter et al. (2022) suggest that the wake effect creates upwelling and downwelling dipoles with increased upwelling of nutrients from the ocean depth on one side and increased downwelling on the other. The study of Daewel et al. (2022) shows that OWFs impact the ocean dynamic and the nutrient access. In the North Sea specifically, OWFs were found to change the annual primary production with 10%, according to Daewel et al. (2022). These changes can have consequences for many stakeholders and must be further addressed for future deployment of offshore wind energy projects.

2.3 Reduced-Gravity Model

During stable atmospheric conditions, the wake effect behind a large wind farm can extend for several tens of kilometers (Lian et al., 2022). As discussed in section 2.1.3, the wind stress decreases inside the wake while the wind moves undisturbed outside of the wake (Krutova, 2024). According to Ekman theory from section 2.2.3, this can drive convergence of water accompanied by downwelling on one side of the farm, and a divergence accompanied by upwelling on the other side (Lian et al., 2022). This is illustrated in Fig. 2.8.

Using a reduced-gravity model, Broström (2008) found that the size of the wind farm is a decisive factor for the magnitude of disturbance caused by the farm wake on the ocean circulation pattern. More specifically, Broström (2008) states that a vertical mass transport pattern similar to the one shown in Fig. 2.8 is expected to form when the size of the wind farm is comparable to the Rossby radius of deformation discussed in section 2.2.2. For the North Sea, this corresponds to approximately 5-10 km (de Jong et al., 2020).

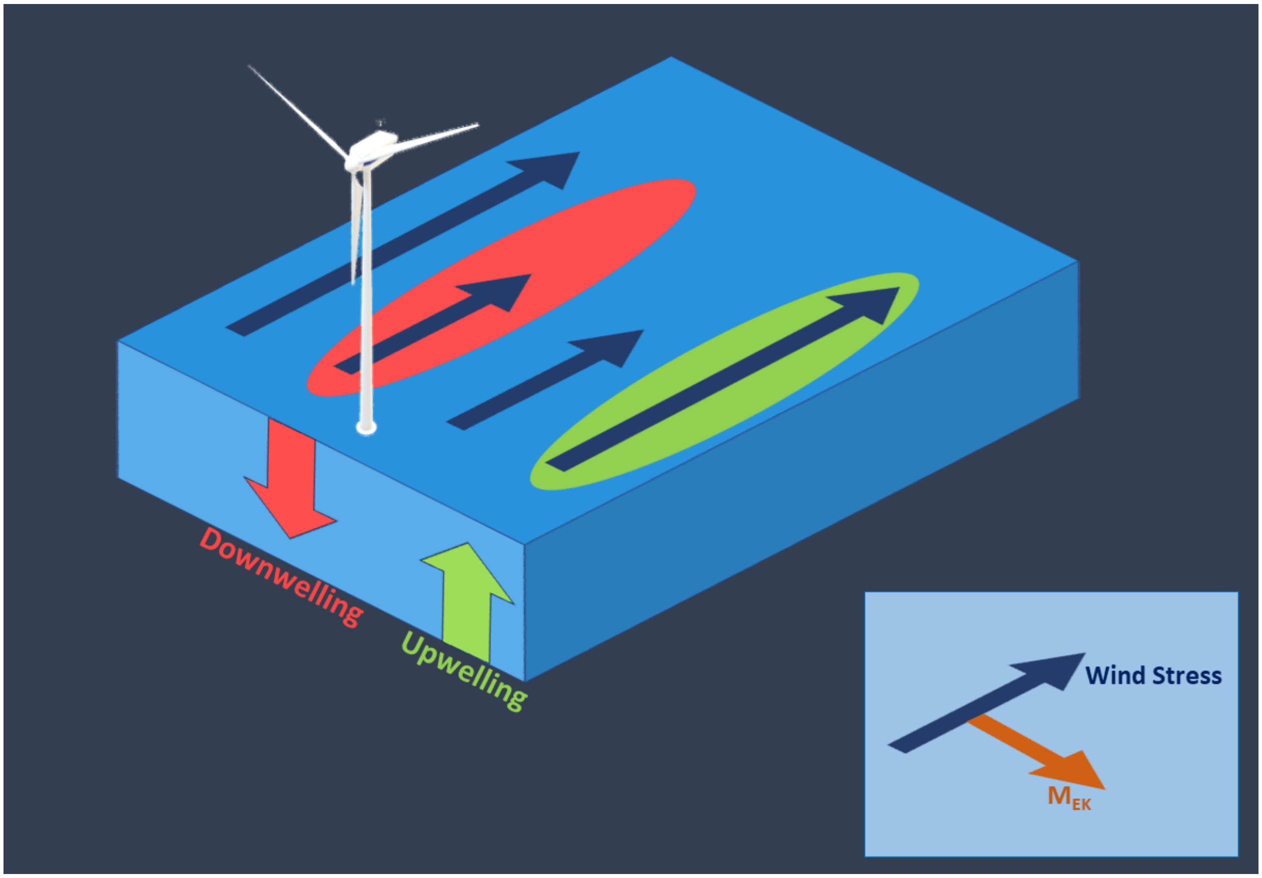

Figure 2.8: As indicated by the length of the dark blue (—) arrows, surface wind stress is undisturbed outside the wake and reduced inside the wake. According to Ekman dynamics, this will result in convergence and downwelling on one side of the turbine and divergence and upwelling on the other side. Figure is inspired by Lian et al. (2022).

The reduced-gravity model is a primitive-equation ocean model, and is described in great detail by Broström (2008), Paskyabi & Fer (2012) and Lian et al. (2022); the reduced-gravity model assumes a two-layered ocean, with a buoyant, dynamically active light layer on top of a deeper and denser motionless layer. The active upper layer has an initial thickness h_0 and density ρ_0, while the lower layer is infinitely deep with density ρ_w. The assumption of a motionless lower layer enables the use of simplified physics to describe the upper ocean circulation, and the model is generally applicable to the deep ocean. The model uses Cartesian coordinates with horizontal coordinates x and y and vertical coordinates z. The latter is set to zero at the ocean surface and has positive direction upward.

The reduced-gravity model describes the response of the upper layer to wind stress forcing using the shallow-water equations derived from the Navier-Stokes equations (Eqs. (2.21) to (2.23)) and the continuity equation (Eq. (2.31)) that will be described in section 2.4.1 (Broström, 2008; Paskyabi & Fer, 2012; Lian et al., 2022). By integrating both equations over the upper active layer with thickness h and applying hydrostatic approximation described in section 2.4.1 as well as neglecting bottom friction forcing, the non-linear conservative *shallow water equations* are found (Paskyabi & Fer, 2012):

$$\frac{\partial}{\partial t}\begin{pmatrix} h \\ uh \\ vh \end{pmatrix} + \frac{\partial}{\partial x}\begin{pmatrix} uh \\ u^2h + \frac{1}{2}gh^2 \\ uvh \end{pmatrix} + \frac{\partial}{\partial y}\begin{pmatrix} vh \\ uvh \\ v^2h + \frac{1}{2}gh^2 \end{pmatrix} = \begin{pmatrix} 0 \\ \dfrac{\tau_x}{\rho_w} + fv \\ \dfrac{\tau_y}{\rho_w} - fu \end{pmatrix}, \tag{2.15}$$

where u and v are horizontal velocity components; h is the upper ocean layer depth; g is gravitational force; τ_x and τ_y are the components of the total wind stress; ρ_w is the density of the deep layer; f is Coriolis.

By linearizing Eq. (2.15) and replacing the gravitational force g with reduced gravity g' given in Eq. (2.8), the following expression is found for the thickness of the upper ocean active layer in response to wind forcing (Broström, 2008):

$$\frac{\partial}{\partial t}\left[\left(\frac{\partial^2}{\partial t^2} + f^2\right)h - \nabla\cdot\left(g' h_0 \nabla h\right)\right] = -\frac{f}{\rho_w}\,\mathrm{curl}\,\tau - \frac{1}{\rho_w}\frac{\partial}{\partial t}\nabla\cdot\tau \tag{2.16}$$

As further described by Broström (2008), short time-scale processes such as internal waves and geostrophic adjustments are also neglected. Thus, all the second-order time derivatives are dropped from the equation. The last term on the right-hand side is also omitted from the equation due to the simplification of temporally constant wind forcing. Next, the variables are made non-dimensional by introducing the scales $t = t' f^{-1}$, $(x, y) = (x', y')L$, $h = \frac{h'\Delta\tau}{f\rho_w L}$, where L is the characteristic size of the wind farm. Thus, the following conservative expressions are obtained for the active layer thickness assuming a temporally constant wind stress forcing:

$$\frac{\partial}{\partial t}\left(h - \gamma^2\nabla^2 h\right) = -\,\mathrm{curl}\left(\frac{\tau}{\Delta\tau}\right) \tag{2.17}$$

or integrated in time:

$$(h-h_0)-\gamma^2\nabla^2(h-h_0) = -t\ \mathrm{curl}\left(\frac{\tau}{\Delta\tau}\right), \tag{2.18}$$

where γ is the Rossby radius of deformation (Eq. (2.7)) divided by L:

$$\gamma = \frac{\sqrt{g'h_0}}{fL} \tag{2.19}$$

As first described by Broström (2008) and later by Paskyabi & Fer (2012) and Lian et al. (2022), both numerical and analytical solutions of Eq. (2.18) show that the maximum vertical response of the ocean is dependent on the normalized Rossby deformation radius γ. This relation is shown in Fig. 2.9; the maximum thickness of the pycnocline decreases as γ^2 increases, i.e. as L decreases. The analytical one-dimensional, time-dependent solution of Eq. (2.18) is given by Broström (2008) as:

$$h(t,y)-h_0 = t\,\frac{\sqrt{\pi}}{16\,\gamma^2}\,e^{-\frac{1}{8\gamma^2}}\left[e^{\frac{2y}{\gamma}}\left(1-\mathrm{erfc}(\tfrac{1}{4\gamma}+2y)\right)-e^{-\frac{2y}{\gamma}}\left(1-\mathrm{erfc}(\tfrac{1}{4\gamma}+2y)\right)\right], \tag{2.20}$$

where erfc is the error function. As stated by Broström (2008), the solution is bounded at infinity, and Gaussian wind stress is a required assumption for this to be valid. Eq. (2.18) and Eq. (2.20) describe that the thickness of the upper ocean layer increases linearly with time and that the disturbance is proportional to the wake size. As further explained by Broström (2008) and also shown in Fig. 2.10, the shape of the cross-section of the upper layer thickness also depends on the value of γ; following the definition of γ given in Eq. (2.19), $\gamma \approx 0$ if $L >>$ the Rossby radius of deformation. Eq. (2.18) shows that the pycnocline thickness is fully determined by the wind stress curl for this scenario. This creates a sharp and local disturbance of the pycnocline thickness. Oppositely, if $L \leq$ Rossby radius of deformation, the disturbance of the pycnocline spreads out over a larger area that corresponds to the Rossby radius of deformation. Another important information given by Fig. 2.10, is that the pycnocline depth increases on the Southern side of the wind farm and decreases on the Northern side. This is in alignment with the vertical disturbance shown in Fig. 2.8 .

When designing future offshore wind projects, an assessment should be carried out of the degree of disturbance the given wind farm has on the vertical mass transport and thus on processes such as e.g. primary production and biodiversity (Palm et al., 2023; Paskyabi & Fer, 2012).

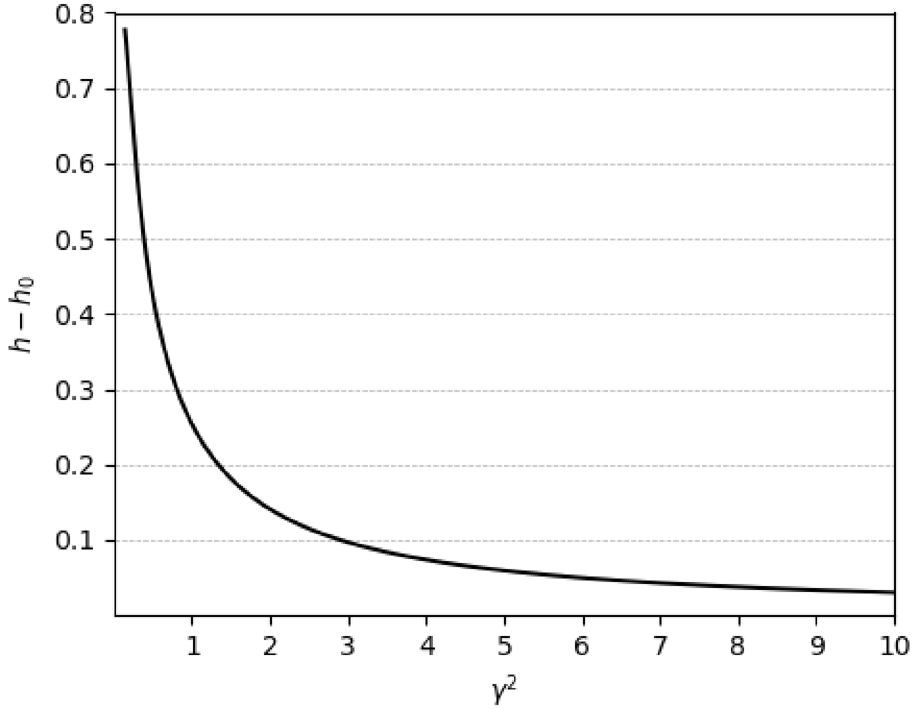

Figure 2.9: Analytical maximum amplitude of pycnocline depth as a function of γ^2. Figure is recreated with python based on theory by Broström (2008).

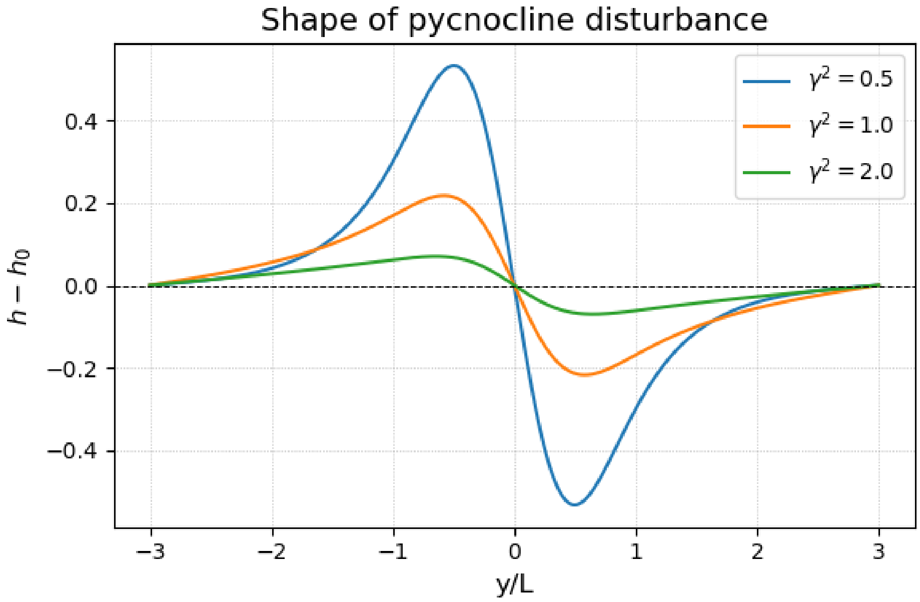

Figure 2.10: Cross-section of analytical maximum amplitude of pycnocline depth for different values of γ^2 (—, —, —). Figure is recreated with python based on theory by Broström (2008).

2.4 Regional Ocean Modeling System (ROMS)

Regional Ocean Modeling System (ROMS) is an advanced numerical ocean model developed by researchers at Rutgers University and the University of California Los Angeles (Wiki ROMS, 2022). Key contributors include Hernan G. Arango, Robert J. Chant, Katherine S. Hedström, James C. McWilliams and Alexander F. Shchepetkin. The first version of ROMS was made available in 1999 and has since been updated multiple times with new functions and improved algorithms. The complete history of ROMS is available at Wiki ROMS (2022). The model is very complex, yet flexible and customizable, making it suitable for a variety of applications within oceanography, meteorology, and energy. ROMS is, however, most suitable for simulating mesoscale eddies and approximately geostrophic currents (Shchepetkin & McWilliams, 2009).

2.4.1 Governing Equations

ROMS is a primitive equation model (Haidvogel et al., 2013). The primitive equations are explained by Drange (2024) as a set of differential equations that describe the physical and thermodynamical processes of the ocean and atmosphere. The basis of the equations includes the fundamental idea of mass and heat conservation, as well as the state equation.

The governing equations used in ROMS are described by Wiki ROMS (2024); the horizontal momentum equation for the x- and y-direction is given in Cartesian coordinates as:

$$\frac{\partial u}{\partial t} + \vec{v}\cdot\nabla u - fv = -\frac{\partial \phi}{\partial x} - \frac{\partial}{\partial z}\left(\overline{u'w'} - \nu\frac{\partial u}{\partial z}\right) + \mathrm{F}_u + \mathrm{D}_u \tag{2.21}$$

$$\underbrace{\frac{\partial v}{\partial t}}_{(1)} + \underbrace{\vec{v}\cdot\nabla v}_{(2)} + \underbrace{fu}_{(3)} = -\underbrace{\frac{\partial \phi}{\partial y}}_{(4)} - \underbrace{\frac{\partial}{\partial z}\left(\overline{v'w'} - \nu\frac{\partial v}{\partial z}\right)}_{(5)} + \underbrace{\mathrm{F}_v}_{(6)} + \underbrace{\mathrm{D}_v}_{(7)}, \tag{2.22}$$

where the first term (local acceleration) and the second term (advection) together form the total derivative, which according to Drange (2024) describes the acceleration when following the direction of the motion; the third term represents the Coriolis parameter; the fourth term is the pressure gradient force; the fifth term is vertical mixing including both turbulent fluxes and molecular viscosity; the sixth term represents external forces such as e.g. wind stress; the seventh term is the horizontal diffusive term.

Similarly, the vertical momentum equation is given by Wiki ROMS (2024) as:

$$\underbrace{\frac{\partial w}{\partial t}}_{(1)} + \underbrace{\vec{v}\cdot\nabla w}_{(2)} = -\underbrace{\frac{\partial \phi}{\partial z}}_{(3)} - \underbrace{\frac{\rho}{\rho_0}g}_{(4)} - \underbrace{\frac{\partial}{\partial z}\left(\overline{w'w'} - \nu\frac{\partial w}{\partial z}\right)}_{(5)} + \underbrace{\mathrm{F}_w}_{(6)} + \underbrace{\mathrm{D}_w}_{(7)}, \tag{2.23}$$

where the Coriolis term is removed and gravitational force is included as the fourth term.

The advection-diffusion equation describes the temporal variation of scalars such as temperature, salinity, and nutrients. It is given by Wiki ROMS (2024) as:

$$\underbrace{\frac{\partial C}{\partial t}}_{(1)} + \underbrace{\vec{v}\cdot\nabla C}_{(2)} = \underbrace{-\frac{\partial}{\partial z}\left(\overline{C'w'} - \nu_\theta \frac{\partial C}{\partial z}\right)}_{(3)} + \underbrace{\mathrm{F}_C}_{(4)} + \underbrace{\mathrm{D}_C}_{(5)}, \tag{2.24}$$

where the first term is the local temporal change of the scalar C; the second term is advection; the third term is the vertical mixing including both turbulent fluxes and molecular diffusivity; the fourth term is forcing terms; the fifth term is the horizontal diffusive terms.

Turbulent mixing is the dominant contributor to vertical mixing in the ocean (Wiki ROMS, 2024). Thus, the terms involving molecular viscosity (ν) and diffusivity (ν_θ) can be neglected. The turbulent fluxes are given by Wiki ROMS (2024) as:

$$\overline{u'w'} = -K_M \frac{\partial u}{\partial z} \tag{2.25}$$

$$\overline{v'w'} = -K_M \frac{\partial v}{\partial z} \tag{2.26}$$

$$\overline{C'w'} = -K_C \frac{\partial C}{\partial z}, \tag{2.27}$$

where K_M and K_C are the vertical eddy viscosity and diffusivity, respectively. The turbulent fluxes are here parameterized using K-theory, which is a technique used in the study of turbulence to deal with closure problems, i.e. higher number of unknowns than number of equations (Stull, 1988, p. 197).

As explained in detail by Drange (2024), the equation of state describes the empirical relationship between density (ρ), salinity (S), temperature (T), and pressure (P). There exist many different versions with varying complexity based on the desired regime. The general form is given by Wiki ROMS (2024) and Drange (2024) as:

$$\rho = \rho(T, S, P) \tag{2.28}$$

Eq. (2.28) indicates that an increase (decrease) in salinity causes a decrease (increase) in density. Similarly, due to the thermal expansion a water parcel undergoes during warm-up, an increase in temperature will lead to a decrease in density and vice versa (Drange, 2024). As further explained by Wiki ROMS (2024) and Drange (2024), density gradients are typically small in the horizontal direction and can thus be neglected for most terms of the momentum equation. The exception is in the vertical momentum equation, where the density variations contribute to the buoyancy force. This assumption is known as the Boussinesq approximation. Furthermore, a dimensional scaling of Eq. (2.23) gives that all terms but the pressure gradient and gravity can be neglected. This is known as the hydrostatic approximation, and is applicable for most large-scale motions in the ocean (Drange, 2024). The hydrostatic equilibrium is given by Wiki ROMS (2024) as:

$$\underbrace{\frac{\partial \phi}{\partial z}}_{(1)} = -\underbrace{\frac{\rho g}{\rho_0}}_{(2)}, \tag{2.29}$$

where the first term is the vertical dynamic pressure gradient and the second term is the buoyancy force.

A liquid with constant density is called incompressible (Drange, 2024). The ocean is thus considered to be approximately incompressible. This is described mathematically by Drange (2024) as:

$$\frac{D\rho}{Dt} = 0 \tag{2.30}$$

As further explained by Drange (2024), the continuity equation describes the mass conservation, and expresses how the density changes with mass flux in or out of a control volume. Combined with the momentum equation, the continuity equation is essential for understanding the dynamics of the ocean. The continuity equation is given by Drange (2024) as:

$$\frac{D\rho}{Dt} + \rho \nabla \cdot \vec{u} = 0 \tag{2.31}$$

From Eq. (2.30) and Eq. (2.31), the continuity equation for incompressible fluids can be written as:

$$\nabla \cdot \vec{u} = 0 \tag{2.32}$$

which is equivalent to the form given by Wiki ROMS (2024):

$$\frac{\partial u}{\partial x} + \frac{\partial v}{\partial y} + \frac{\partial w}{\partial z} = 0 \tag{2.33}$$

As explained by Drange (2024), Eq. (2.32) and Eq. (2.33) express that there is no divergence within the flow. Consequently, there has to be a vertical transport of mass in cases of divergence or convergence at the ocean surface. This is the essence of the Ekman pumping discussed in section 2.2.3.

2.4.2 Vertical Discretization

This chapter is based on Wiki ROMS (2016) and Wiki ROMS (2019b).

In the vertical, ROMS uses a free-surface, terrain-following S-coordinate system with adjustable stretching and number of grid cells. This implies that the grid cells can vary in size and thickness depending on the desired resolution. This can be beneficial at e.g. the sea-surface and seabed, where higher resolution might be required to capture rough topography. This is illustrated in figure Fig. 2.11. The grid is vertically staggered, where horizontal momentum (u,v), density ρ and tracers t are calculated in the center of the grid cells while vertical velocity w and vertical mixing variables are calculated at the top and bottom surfaces of the grid cells. The total thickness of the water column is given by the sum of the bottom bathymetry $h(i,j)$ and the free-surface elevation $\zeta(i,j)$.

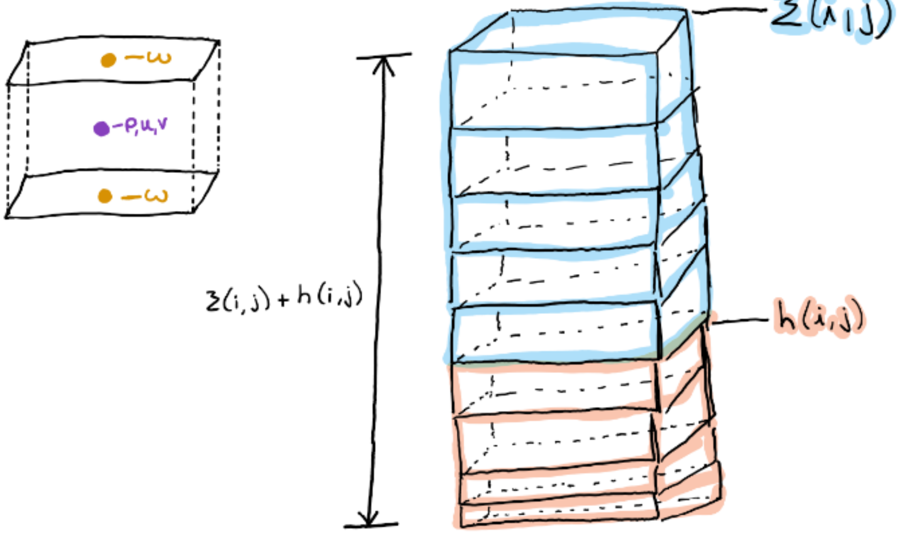

Figure 2.11: Staggered vertical grid. On the left, a single grid cell is shown. Horizontal momentum (u,v), density ρ and tracers are calculated in the center of the grid cell (—) while the vertical velocity w and vertical mixing variables are calculated at the top and bottom surfaces of the grid cell (—). On the right, the orange (—) grid cells represent the sediments and the blue (—) grid cells represent the water column. The total thickness of the water columns is given by the sum of the bathymetry h and the free-surface ζ. Figure is adapted from Wiki ROMS (2016).

2.4.3 Horizontal Discretization

This chapter is based on Wiki ROMS (2016).

In the horizontal, ROMS uses boundary-fitted orthogonal curvilinear coordinates (ζ, η) on a staggered Arakawa-C grid. This is illustrated in Fig. 2.12. As shown, the density ρ, the free-surface elevation ζ and tracers t are all calculated in the center of the grid cell (called the ρ-point) and follow the indices of the axes. Following their own respective indices, the horizontal velocities u and v are calculated at the edges of the cell, more specifically at the west-east and south-north borders, respectively. Lastly, ψ is calculated at the corners of the grid cell.

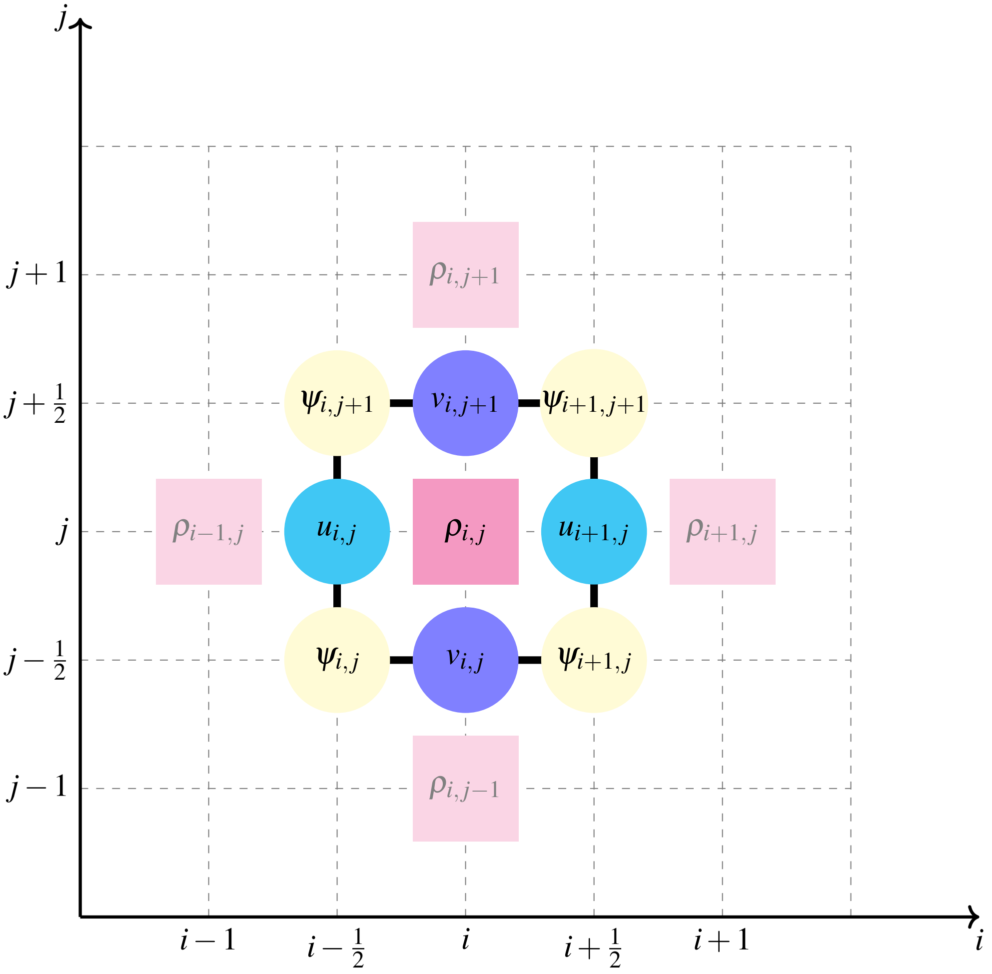

Figure 2.12: Staggered Arakawa C-grid. The axes show the indices of ρ. The horizontal grid cell is outlined by a solid black line (—). The density ρ, the free-surface elevation ζ and tracers t are all calculated in the center of the grid cell (—). Following their own respective indices, the horizontal velocities u (—) and v (—) are evaluated at the edges of the cell, and ψ (—) is calculated at the corners of the grid cell. The four transparent magenta rectangles each represent the center of the adjacent grid cells. Figure is adapted from Wiki ROMS (2016).

2.4.4 Numerical Stability

The numerical stability of ROMS depends on how the model handles time-stepping. The Courant-Friedrichs-Lewy (CFL) criterion sets an upper bound for the time-step size the model can handle before instability occurs, and is generally expressed as (Gnedin et al., 2018):

$$C_{CFL} = \frac{c_{phase}\Delta t}{\Delta x} \leq C_{\max}, \tag{2.34}$$

where C_{CFL} is the Courant number; c_{phase} is the phase speed; Δt is the time step; C_{max} is a constant.

As shown in Eq. (2.34), the maximum time step size that the model can handle without introducing instabilities depends on the phase speed. A higher phase speed requires shorter time steps and vice versa. ROMS handles both fast barotropic modes and slow three-dimensional baroclinic modes (Shchepetkin & McWilliams, 2009). As further explained by Shchepetkin & McWilliams (2009), the phase speed of barotropic modes is assumed to be an order of magnitude faster than the baroclinic modes. Thus, the CFL criterion is the most restrictive for the barotropic modes as they require higher resolution to be captured properly.

To maintain stability without increasing computational costs by unnecessarily reducing the time step for the slow baroclinic processes, ROMS uses a split-explicit time-stepping scheme to solve the hydrostatic primitive momentum equations (Shchepetkin & McWilliams, 2005, 2009; Wiki ROMS, 2016). As explained in great detail by Shchepetkin & McWilliams (2005, 2009), this technique separates the barotropic and baroclinic modes and solves them separately but in a coupled manner, using two different temporal resolutions; barotropic modes are fast-evolving and require small time steps to be accurately captured, whereas baroclinic modes evolve more slowly, making larger time steps feasible. Consequently, several barotropic time steps are executed within each baroclinic time step (DMCS Ocean Modeling Group, 2025). This allows the model to accurately capture both rapid and slow oceanic processes without compromising stability and computational costs.

To mitigate aliasing of unresolved frequencies in the slow baroclinic time-stepping, the barotropic variables are time-averaged in the barotropic time step with a cosine-shaped filter before being coupled to the baroclinic equations (Shchepetkin & McWilliams, 2009; DMCS Ocean Modeling Group, 2025). In addition, all 2D and 3D equations are time-discretized using a Leapfrog predictor with third-order accuracy, combined with an Adams-Moulton corrector time-stepping algorithm (DMCS Ocean Modeling Group, 2025). According to DMCS Ocean Modeling Group (2025), this combination enhances the stability and robustness of the model, allowing for larger time steps without losing accuracy.

2.4.5 Horizontal Boundary Conditions

ROMS have multiple horizontal boundary conditions to choose from based on the application (Wiki ROMS, 2019a). The options are shown in Table 2.1 and include different types of open, closed and cyclic boundary conditions.

Table 2.1: An overview of all the horizontal boundary conditions available for ROMS (Wiki ROMS, 2019a).

Long Name	Short Name
Chapman Implicit	Cha
Chapman Explicit	Che
Clamped	Cla
Closed	Clo
Flather (2D momentum)	Fla
Gradient	Gra
Nested	Nes
Nudging	Nud
Periodic	Per
Radiation	Rad
Reduced Physics (2D momentum)	Red
Schchepetkin (2D momentum)	Sch

2.4.6 Advection Schemes

ROMS offers several options for advection schemes, including the default third-order upstream biased scheme, and second- and fourth-order centered difference schemes (DMCS Ocean Modeling Group, 2025). The stability of these schemes is ensured through the predictor-corrector methodology as already mentioned (DMCS Ocean Modeling Group, 2025). All the available advection scheme options for tracers are shown in Table 2.2. The second-order centered difference scheme is the simplest, but does not handle strong gradients very well (Wiki ROMS, 2016). A more detailed description of the different tracer advection schemes is available on Wiki ROMS (2016).

Table 2.2: An overview of all the tracer advection schemes available for ROMS (Wiki ROMS, 2021, 2016).

Keyword	Advection Scheme	Direction
A4	4th-order Akima	horizontal/vertical
C2	2nd-order centered differences	horizontal/vertical
C4	4th-order centered differences	horizontal/vertical
HSIMT	3rd-order High-order Spatial Interpolation at Middle Time with TVD limiter	horizontal/vertical
MPDATA	recursive flux corrected MPDATA	horizontal/vertical
SPLINES	parabolic splines reconstruction	vertical
SU3	split third-order upstream	horizontal/vertical
U3	3rd-order upstream-bias	horizontal

2.4.7 Coupling Options

ROMS can be initialized as an independent model or coupled with other models such as atmospheric models, biogeochemical models, bio-optical models, sea-ice models, sediment models, and wave models (DMCS Ocean Modeling Group, 2025). This makes ROMS flexible and customizable for several applications.

Bio Fennel Model

One coupling option that is relevant to this thesis is the Bio Fennel model described by Wiki ROMS (2020a); this option sets biological tracers such as nitrate (NO_3), ammonium (NH_4), chlorophyll, phytoplankton biomass, zooplankton biomass, inorganic carbon, alkalinity and oxygen. The coupling configuration is user-friendly and easy to set up. The default ASCII input file for the biological parameters is included in the ROMS source code. The path to the biological input file is then specified in the main project input file, and the corresponding biology CPP options are activated in the main project header file. The Bio Fennel biological model is provided with default settings that can be used as is, or they can be customized as needed. Examples of customizable settings are described in Wiki ROMS (2020a) and include options for light attenuation, growth-rate and mortality rate of plankton, vertical sinking velocity for detritus, vertical mixing coefficients and CO_2 partial air pressure. Different horizontal and vertical advection schemes can also be selected for each tracers, see Table 2.2 in section 2.4.6.

The advection-diffusion equation (Eq. (2.24)) describes the temporal variations of tracers. It does, however, not account for biogeochemical sources and sinks such as growth rate, mortality rate, available radiation, grazing rate, nitrification rate etc. Thus, to fully describe the temporal variation of biological tracers, all relevant sources and sinks must be added to the right side of Eq. (2.24). Fennel et al. (2006) describes, in great detail, the most relevant sources and sinks and how they affect the temporal change of phytoplankton, chlorophyll, zooplankton, NO_3 and NH_4:

The temporal rate of change of phytoplankton as a result of sources and sinks is given by Fennel et al. (2006) as:

$$\frac{\partial \mathrm{Phy}}{\partial t} = \mu \mathrm{Phy} - g\mathrm{Zoo} - m_P \mathrm{Phy} - \tau(SDet + Phy)Phy - w_p \frac{\partial \mathrm{Phy}}{\partial z}, \tag{2.35}$$

where Phy is phytoplankton; μ is the phytoplankton growth rate, which is dependent on temperature, radiation available for photosynthesis, and concentration of nutrients NO_3 and NH_4; Zoo is zooplankton; $SDet$ is small detritus; g is the phytoplankton grazing by zooplankton; m_p is the phytoplankton mortality rate; τ is the aggregation parameter; w_p is constant vertical sinking velocity.

The temporal rate of change of chlorophyll as a result of sources and sinks is given by Fennel et al. (2006) as:

$$\frac{\partial \mathrm{Chl}}{\partial t} = \rho_{Chl} \mu \mathrm{Chl} - g\mathrm{Zoo}\frac{Chl}{Phy} - m_p \mathrm{Chl} - \tau(SDet + Phy)Chl, \tag{2.36}$$

where Chl is chlorophyll; ρ_{Chl} is the fraction of phytoplankton growth used for chlorophyll synthesis.

The temporal rate of change of zooplankton as a result of sources and sinks is given by Fennel et al. (2006) as:

$$\frac{\partial \mathrm{Zoo}}{\partial t} = g\beta \mathrm{Zoo} - l_{BM}Zoo - l_E \frac{Phy^2}{k_p + Phy^2}\beta Zoo - m_z Zoo^2, \tag{2.37}$$

where Zoo is zooplankton; β is the assimilation efficiency, i.e. how much of the total ingested biomass is absorbed (Allaby, 2010); l_{BM} is the excretion rate associated with basal metabolism; l_E is the maximum rate of excretion associated with assimilation; k_p is the half-saturation concentration of phytoplankton ingestion, i.e. how much phytoplankton zooplankton needs available to meet half its maximum intake (Mulder & Hendriks, 2014); m_z is the mortality rate of zooplankton.

The temporal rate of change of $\mathrm{NO_3}$ as a result of sources and sinks is given by Fennel et al. (2006) as:

$$\frac{\partial \mathrm{NO3}}{\partial t} = -\mu_{max} f(I) L_{NO3} Phy + nNH4, \tag{2.38}$$

where $NO3$ is nitrate; $NH4$ is ammonium; μ_{max} is the maximum growth rate of phytoplankton; $f(I)$ is the relationship between photosynthesis and light; L_{NO3} is the nutrient limitation function for nitrate; n is the nitrification rate.

The temporal rate of change of $\mathrm{NH_4}$ as a result of sources and sinks is given by Fennel et al. (2006) as:

$$\frac{\partial \mathrm{NH4}}{\partial t} = -\mu_{max} f(I) L_{NH4} Phy - nNH4 + l_{BM}Zoo + l_E \frac{Phy^2}{k_p + Phy^2}\beta \cdot Zoo + r_{SD}SDet + r_{LD}LDet, \tag{2.39}$$

where L_{NH4} is the nutrient limitation function for ammonium; r_{SD} is the rate of remineralization of suspended detritus; r_{LD} is the rate of remineralization of large detritus.

2.4.8 ROMS and Sound Propagation Modeling

Salinity, temperature and pressure data from ROMS simulations can be used to create sound speed profiles that can be further used as input data for sound propagation modeling (Firouz et al., 2024). This will be further discussed in chapter 8.

2.5 Basic Sound Theory

Section 2.5.1 and section 2.5.2 are based on Jensen et al. (2011) unless otherwise specified.

2.5.1 Sound Speed

The sound speed in the ocean ranges between approximately 1450-1570 m/s (Mackenzie & Byrne, 2025), and is a function of of density, i.e. temperature and salinity, and compressibility, i.e. static pressure. The sound speed can be expressed as:

$$c = 1449.2 + 4.6T - 0.055T^2 + 0.00029T^3 + (1.34 - 0.01T)(S - 35) + 0.016z, \tag{2.40}$$

where T is temperature in Celsius; S is salinity in parts per thousand; z is depth in meter.

The equation is a simplification, but it is accurate enough for most scenarios. As shown by Eq. (2.40) and Fig. 2.13, the sound speed increases with increasing temperature, salinity, and pressure. Pressure is a function of depth, i.e. pressure increases with depth. Thus, generally the sound speed also increases with depth. As discussed in section 2.2.1, the upper ocean undergoes both diurnal and seasonal changes, resulting in variations in temperature and other parameters. In turn, these changes affect the propagation of sound throughout the water column. When the surface temperature rises, e.g. during the summer or mid-day, there will be a similar increase in the sound velocity towards the surface. The upper part of the ocean directly affected by these varying surface forcings and oceanographic conditions, is known as the surface duct region. In the mixed layer, the temperature is approximately uniform due to wind-driven mixing. In this layer, the sound speed is determined mainly by the vertical pressure gradient, increasing as the pressure increases down the water column. The layer below is called the main thermocline. Here, both the temperature and sound velocity decrease with depth. In the deep ocean below the thermocline, the temperature is yet again close to constant, and as for the mixed layer, the sound velocity is here increasing with depth due to the vertical pressure gradient. Between the two isothermal layers, a sound speed minimum is found. This minimum is known as the deep sound channel axis. As shown in Fig. 2.13, this does not apply for polar regions. Instead, the sound speed increases down the entire water column due to cold surface water temperatures.

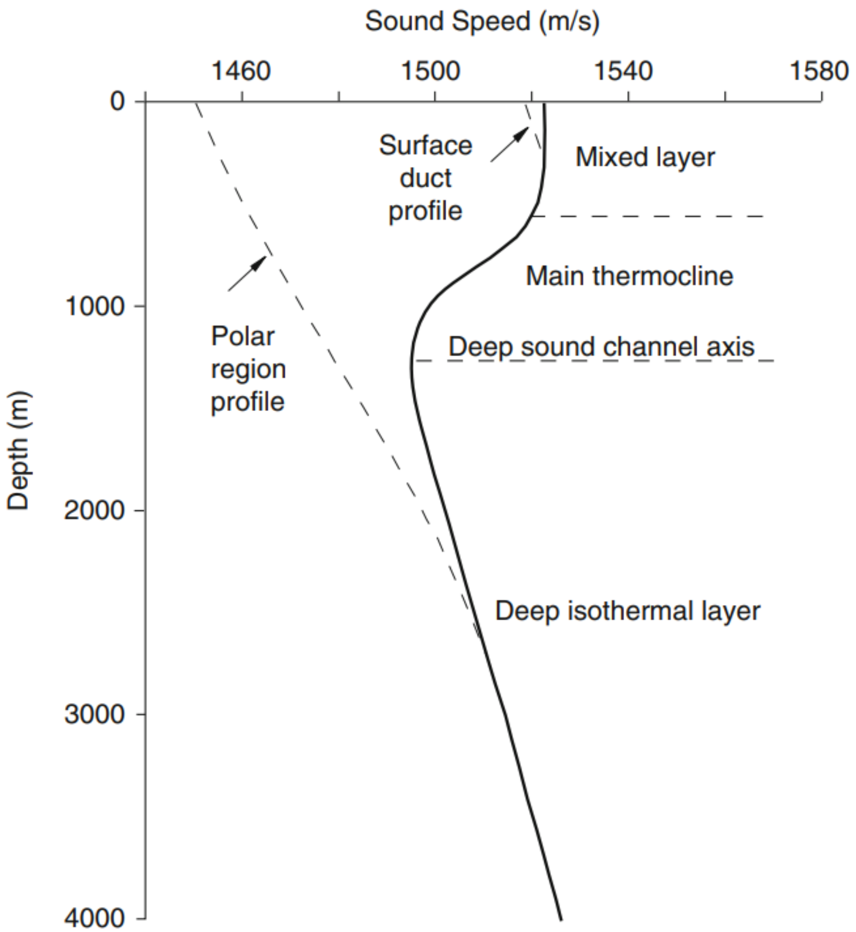

Figure 2.13: General ocean sound speed profile with sound speed on the x-axis and depth on the y-axis. Figure is from Jensen et al. (2011).

2.5.2 Sound Propagation in the Ocean

Based on the sound speed profile, sound signals follow different paths while propagating through the ocean. This is known as Snell's law and can be expressed as:

$$\frac{\cos\theta}{c} = \text{const}, \tag{2.41}$$

where c is the local sound speed; θ is the angle of the sound signal relative to the horizontal plane.

Eq. (2.41) indicates that the sound bends towards regions with lower sound speed. This happens locally. Fig. 2.14 shows a schematic representation of some different propagation paths, which is described in further detail by Jensen et al. (2011). Ocean sound propagation is extremely complex. The environmental variables affecting sound propagation include ocean stratification, bathymetry, and wind-wave interactions at the surface. In addition, sound propagation can differ depending on the frequency of the signal.

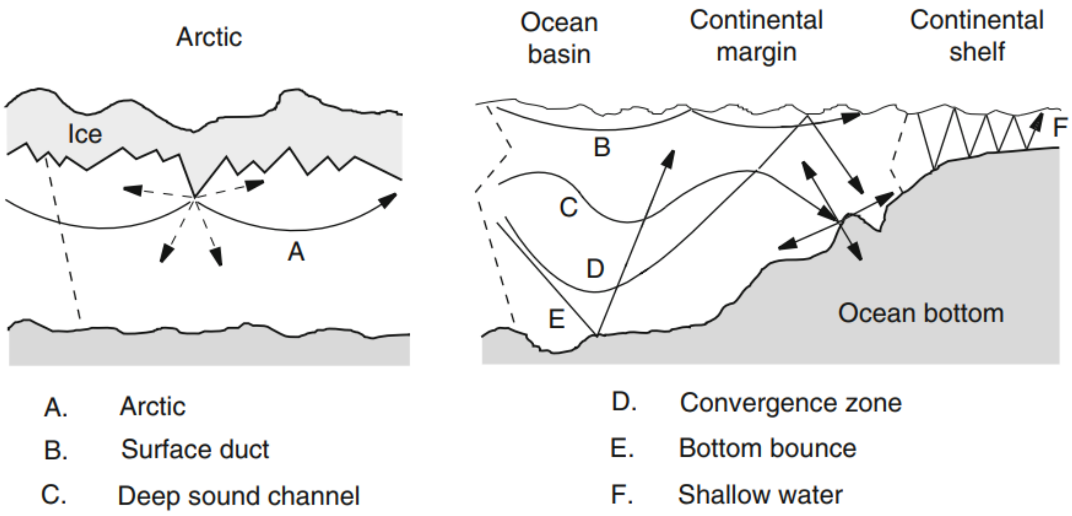

Figure 2.14: Different propagation paths for sound in the ocean. Figure is from Jensen et al. (2011).

2.5.3 The Effect of Offshore Wind Farms on Ocean Sound Propagation

Many ocean animals use sound to communicate with each other, to locate food, to find mating partners, to locate predators, and for general navigation (Forland et al., 2025). As already discussed in section 2.2, OWFs can affect upwelling and downwelling patterns. In a recent study conducted by Lopes et al. (2024) it was found that coastal upwelling caused changes in sound speed by several orders of magnitude in a Brazilian bay. Changes in sound speed can affect the ability of ocean animals to communicate, locate predators, and find food as well as mating partners (Affatati et al., 2022). As described in section 2.5.1 and section 2.5.2 and by Jensen et al. (2011), changes in the sound speed profile can in turn disturb the sound propagation in the ocean. As described by Talley et al. (2011a,b,c), upwelling redistributes cold water upwards and downwelling redistributes warmer water downwards. This means that the thermocline can be shifted upwards in cases of upwelling and downwards in cases of downwelling (Marshall & Plumb, 2008; Talley et al., 2011c). In the theory of Jensen et al. (2011) discussed in section 2.5.1 and section 2.5.2, it has become clear that sound bends towards regions with lower sound speed (Snell's law, Eq. (2.41)). This means that sound traveling obliquely through the water column towards the sea bottom will bend upwards in cases of positive sound speed gradient and bend downwards in cases of negative sound speed gradient (Mackenzie & Byrne, 2025). In addition, the theory of Jensen et al. (2011) describes that sound speed decreases downward the thermocline. Based on all of this, it would be reasonable to think that sound can travel deeper before it is refracted in areas with downwelling of warmer water. Following the same logic, in areas with upwelling, the emergence of colder water at shallower depths would reduce the local sound speed, causing the sound to refract towards these colder regions.

That means that OWFs may disturb the sound speed and propagation of sound emitted by e.g. animals. This aspect is important to include in the risk assessments of future offshore wind energy projects, and it is also the main focus of the acoustic part of this thesis.

Chapter 3

Methodology

3.1 Area of Investigation

This thesis is based on idealized numerical experiments, and the results are thus not fully comparable to realistic scenarios nor fully representative for any site-specific area of investigation. However, idealized cases can still provide valuable insight into physical and dynamical processes that are relevant to the real ocean.

3.2 Regional Ocean Modeling System (ROMS)

To study the ocean response to the presence of OWFs, the complex ROMS model (Arango & Shchepetkin, 2024) has been used. In this chapter, the numerical setup and configuration as well as methods of data processing are presented.

3.2.1 Numerical Experiments

To study how the upper ocean responds to the presence of OWFs, a sensitivity analysis was carried out with the aim of isolating different factors, allowing them to be studied individually.

A detailed description of all the numerical experiments is shown in Table 3.1 and Fig. 3.1. As seen, the numerical experiments are divided into two groups based on the farm layout. In the first group (experiments 1-8), the farm is modeled as a singular square, with the aim of capturing the basics of the ocean response. In the second group (experiments 9-10), multiple squares are applied to simulate overlapping farms, which are of interest from an economic perspective for optimizing the spatial use of ocean areas and minimizing power cable costs.

For experiments 1-8, the model was run for two different farm sizes $L = (5, 10)$ km, three different initial horizontal wind stresses $\tau_{x0} = (0.05, 0.08, 0.10)$ N/m^2 and two different wind stress reduction values $\Delta\tau = (0.05, 0.10)$ N/m^2. For experiments 9-10, the model was run with initial horizontal wind stress τ_{x0} set to 0.10 N/m^2 and wind stress reduction $\Delta\tau$ set to 0.05 N/m^2 for overlapping wakes consisting of two and three wind farms with $L = 8$ km. To isolate the effect of the wind farms, baseline simulations without wind farm effects (uniform wind stress) were carried out for each τ_{x0} and used to make anomaly plots.

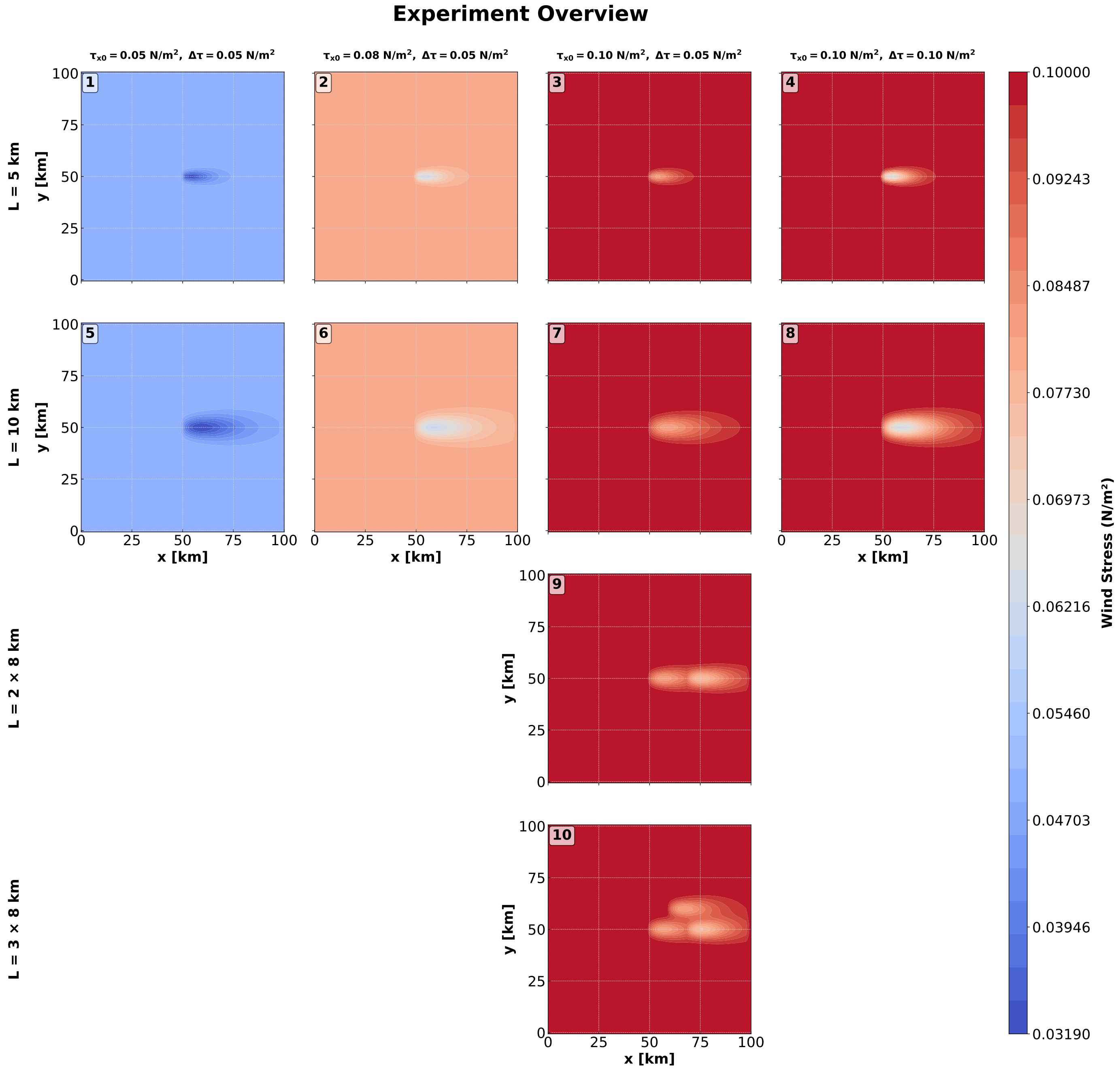

Figure 3.1: Overview of the numerical experiments. The numbers in the upper left corner correspond to the experiment numbers shown in Table 3.1.

Table 3.1: Overview of the numerical experiments.

Farm Layout	**Experiment #**	**Farm Size L (km)**	τ_{x0} **(N/m^2)**	$\Delta\tau$ **(N/m^2)**	**Description**
Single Farm	1, 5	5, 10	0.05	0.05	Weak wind stress
	2, 6	5, 10	0.08	0.05	Moderate wind stress
	3, 7	5, 10	0.10	0.05	Strong wind stress
	4, 8	5, 10	0.10	0.10	Strong wind stress + strong wind reduction
Multiple Overlapping Farms	9	2×8	0.10	0.05	Strong Wind Stress
	10	3×8	0.10	0.05	Strong Wind Stress

3.2.2 Wind and Wake Field

To generate the wake field behind the turbines as shown in Fig. 3.2 and Fig. 3.1, the wind stress acting on the ocean surface was analytically calculated. Following the description of both Broström (2008) and Paskyabi & Fer (2012), this was done using a Gaussian function that describes the distribution of the wind deficit field in the lee of a wind farm:

$$P(x,y) = \exp\left(-\left(\frac{2y}{\alpha L+\beta x}\right)^2\right)\max\left(\frac{x\exp((1-x)/L)}{L},0\right), \tag{3.1}$$

where L is the characteristic farm length; x and y are the horizontal axes; α and β are variables describing the width and length of the wake, and have to be selected such that $\alpha+\beta=1$. Following Paskyabi & Fer (2012), $\alpha = 0.8$ and $\beta = 0.2$.

The horizontal x-direction wind stress τ_x was then calculated as followed (Paskyabi & Fer, 2012):

$$\tau_x = \tau_{x0} - \Delta\tau \times P(x,y), \tag{3.2}$$

where τ_{x0} is the initial horizontal wind stress acting on the domain (the wind stress outside of the wind farm wake); $\Delta\tau$ is the reduction in wind stress in the x-direction caused by the presence of the wind farm (inside the wake).

Eq. (3.1) and Eq. (3.2) were implemented once for the experiments with single-farm layout, twice for the experiment with two overlapping farms and three times for the experiment with three overlapping farms. Note that for the experiments with overlapping farms, the value of τ_{x0} for each farm was determined and updated iteratively from the wind stress directly in front of the respective farm. The distribution and magnitude of the horizontal wind stress for three overlapping farms is shown in Fig. 3.2. As seen in the cross-section, the wind stress deficit is about the same for farm I and III as no farm is blocking the wind upwind. For farm II the wind stress is further reduced due to being placed inside the wake of farm I.

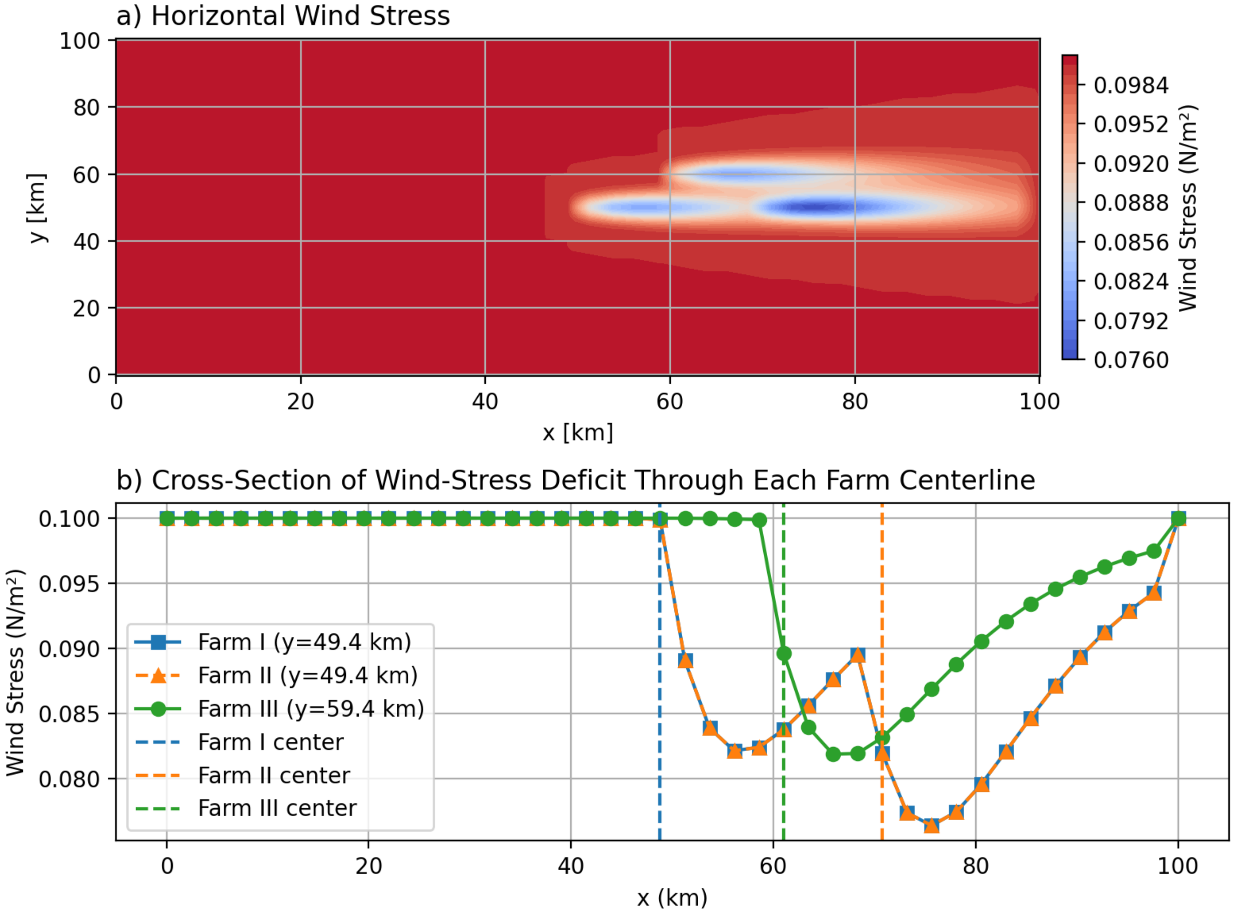

Figure 3.2: a) The distribution of the horizontal wind stress upwind and downwind of three overlapping wind farms. The artificial wind farms have $L = 8$ km. The wind stress is reduced, creating a wake behind the farm that extends for several kilometers before the wind stress returns to its original far-upwind value. The wind stress deficit has been analytically calculated using a Gaussian function. b) A cross-section of the horizontal wind stress deficit through each farm centerline. The reduction is stronger for farm II as it is located inside the wake of farm I.

3.2.3 ROMS Configuration

The backbone of the ROMS experiments in this thesis is the idealized test case for wind-driven upwelling in a periodic channel described by Wiki ROMS (2008). For simplicity, most of the configuration has been left untouched. However, to be representative for an open ocean basin, the test case has been somewhat modified. To study the effect of OWFs on the ecosystem and primary production, the model was also coupled with the Bio Fennel model described in section 2.4.7. For simplicity, all default values were used in this model. The utilized model configuration is described below. In addition, all the activated CPP-flags can be found in appendix C.

Spatial- and Temporal Resolution

For all numerical experiments, the total simulation time was set to 2304 time steps each of size 300 seconds. This includes a spin-up time of 2 days and 6 days post spin-up. The spin-up time was selected through an evaluation of the stability of the kinetic energy with a threshold of 5%.

The model uses analytical grid set-up. The horizontal grid consists of 41 interior ρ-points in the i-direction (x-direction) and 80 interior ρ-points in the j-direction (y-direction). The x-direction spacing was set to 2.44 km and the y-direction spacing was set to 1.25 km. This gives a horizontal domain size of approximately 100×100 km. Following Paskyabi & Fer (2012), the wind farm was represented by one or several rigid rectangles with varying L centered within the domain. This is illustrated in Fig. 3.3. As shown, L aligns with the direction of the wind.

In the vertical, the domain consists of 16 s-levels across a depth of 150 m. See appendix D and appendix G for an overview of the grid parameters. To represent an open ocean basin, the shelves on each side of the original channel were replaced by uniform bathymetry with depth 150 m everywhere.

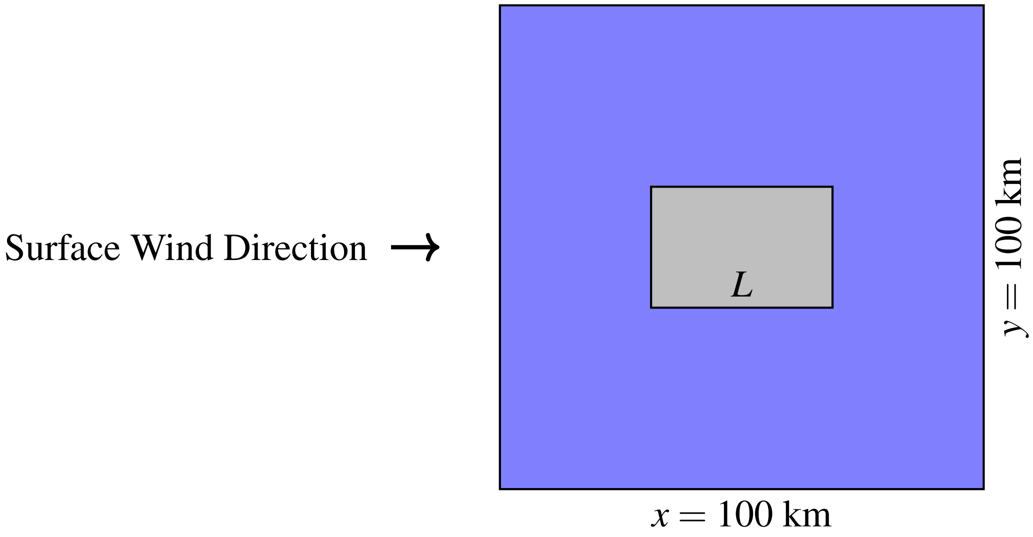

Figure 3.3: General domain dimensions for the numerical experiments. The simulated ocean area is a square with dimensions 100×100 km (—) and the wind farm is a rigid rectangle (—) with varying characteristic farm size L, aligning with the surface wind direction (from west).

Analytical Initial- and Forcing Conditions

The model uses analytically set initial- and forcing conditions. The initial velocity field and free surface were set to zero. The salinity was uniformly set to 35 psu, and the temperature ranges from approximately 22.5°C at the surface to 13.6°C at the ocean bottom, following the trigonometric function:

$$T(z) = T_0 + \frac{z+75.0}{150.0} + 4.0\left(1.0 + \tanh\left(\frac{z+35.0}{6.5}\right)\right), \tag{3.3}$$

where T_0 is the background potential temperature given in Table G.1 in appendix G; z is the ocean depth.

The initial vertical profile of the temperature is shown in Fig. 3.4. As shown, the initial thermocline depth is approximately 33.5 m. In the Fennel model, NO_3, NH_4, chlorophyll, phytoplankton, zooplankton, total alkalinity and total inorganic carbon were set to 1.67-2.65 mmol nitrogen m^{-3}, 0.1 mmol nitrogen m^{-3}, 0.02 mg, 0.08 mmol nitrogen m^{-3}, 0.06 mmol nitrogen m^{-3}, 2350 mmol m^{-3} and 2100 mmol m^{-3}, respectively. See appendix E for full overview of the initial conditions.

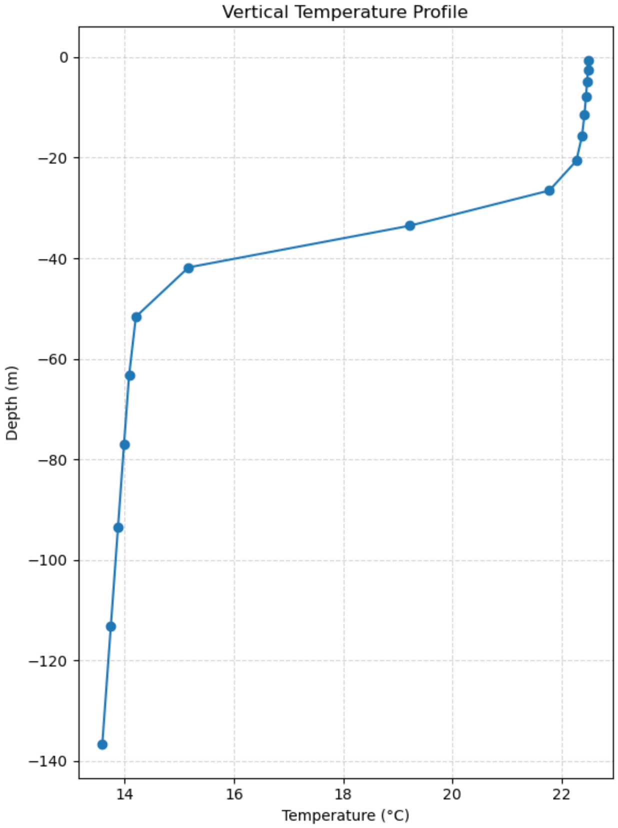

Figure 3.4: The initial ocean temperature profile for ROMS simulations. The temperature ranges from approximately 22.5°C at the surface to approximately 13.6°C at the bottom. The initial thermocline depth is approximately 33.5 m.

Surface momentum, i.e. analytical wind stress was then initialized with positive values in the x-direction and set to zero in the y-direction to represent westerly winds. The wind farm wake was modeled using the Gaussian function described in section 3.2.2. To represent the Northern Hemisphere, the Coriolis parameter f was set to 1.28×10^{-4} s^{-1}. Based on Eq. (2.6), this corresponds to latitudes of approximately 55-60°. As listed in Table G.1 in appendix G and Table E.1 in appendix E, the surface and bottom temperature and salinity fluxes were set to zero, and kinematic surface solar shortwave radiation flux was uniformly set to 150 $\mathrm{W/m^2}$. An overview of the vertical and horizontal mixing coefficients are shown in appendix F.

Boundary Conditions

Periodic boundary conditions were applied to all variables in the East-West directions and gradient (zero-gradient) boundary conditions were applied to all variables in the North-South directions. See Table 2.1 for further description. No nudging or volume conservation was applied at the boundaries.

Numerical Schemes

The model uses three different advection schemes. For temperature, it uses a third-order upstream-biased advection scheme in the horizontal direction and a fourth-order centered difference advection scheme in the vertical direction. For salt and biological parameters, the model uses a third high-order spatial interpolation at middle time advection scheme with Total Variation Diminishing (TVD) limiter in both the horizontal and vertical direction. See section 2.4.6 for further description.

3.2.4 Data Processing

Data processing accounts for a significantly large part of the workload in this thesis. ROMS provide a lot of output data, some of which can be plotted and presented as is, and some of which need to be further processed first. The latter will be described in this chapter. Properties not mentioned (vertical velocity, temperature, biological tracers, and primary production) have been provided directly from ROMS.

Surface Elevation

The surface elevation anomaly outputs from ROMS were multiplied by -1 to align with the ROMS coordinate system and its sign conventions (Wiki ROMS, 2020b), as well as with the color conventions used in previous studies (Paskyabi & Fer, 2012). This ensures that the results are more intuitive, with negative values representing downwelling, and positive values representing upwelling.

xroms Toolbox

An open-source ROMS post-processing tool called xroms was used to make the data processing faster (Thyng et al., 2024a,b). The toolbox is made available on GitHub by Thyng et al. (2024a). It is written in python and is based on xarray. The toolbox makes the data processing easier and more efficient by adding vertical z-coordinates, providing extra ROMS coordinates, grid lengths, grid areas, grid volumes, and it has built-in functions to calculate physical properties such as density, buoyancy, kinetic energy, horizontal convergence, horizontal and vertical gradients, velocities and more. It is also possible to change between different grids, calculate derivatives, and calculate spatial averages and summations over one or more of the grid dimensions while accounting for varying grid cell sizing. The toolbox also has options for interpolation. The complete documentation can be found in Thyng et al. (2024b).

Normalized Horizontal Convergence

As described in section 2.2.3, convergence of water at the ocean surface is associated with downwelling of water and divergence of water at the surface is associated with upwelling of water (Marshall & Plumb, 2008). Thus, horizontal surface convergence is a useful parameter in the study of vertical mass transport. The xroms toolbox comes with a function that uses horizontal velocity components u and v to calculate the horizontal surface divergence given as (Thyng et al., 2024c):

$$\nabla \cdot \mathbf{u} = \frac{\partial u}{\partial x} + \frac{\partial v}{\partial y} \tag{3.4}$$

and normalizes it by the Coriolis parameter. Eq. (3.4) essentially describes how rapidly the horizontal velocity changes in each horizontal direction. $\nabla \cdot \mathbf{u} > 0$ indicates divergence and upwelling, and $\nabla \cdot \mathbf{u} < 0$ indicates convergence and downwelling.

Ekman Pumping

To calculate the Ekman pumping from Eq. (2.14), the xroms module called ”utilities” was used. First, the raw wind stress output was transferred from u-points to ρ-points in the x-direction using the function ”to_rho”. Then, the wind stress curl was calculated using the functions ”ddxi” and ”ddeta”. Lastly, the Ekmpan pumping was calculated as shown in Eq. (2.14). The utility modules is described in detail by Thyng et al. (2024d).

Thermocline

The xroms utility module was also used to compute the spatial disturbance of the thermocline depth. The thermocline can be define as the depth with the largest vertical temperature gradient (Zhu et al., 2020). Thus, the xroms utility function ”ddz” was used to calculate the vertical temperature gradient over the S-coordinate ρ-points. The physical depth corresponding to the maximum gradient was then extracted. To account for spatial and temporal changes in sea-surface elevation associated with upwelling and downwelling, the instantaneous free surface was subtracted from the physical depth.

Sound Speed

Sound speed was calculated from Eq. (2.40) using temperature, salinity and depth data from ROMS.

Integral and Spatial-Average Plots

To calculate spatial integrals, the function ”gridsum” from xroms utilities was used. This function calculates the sum of a variable across the grid in one or more spatial dimension. Similarly, the function ”gridmean” calculates the spatial average of a variable across the grid in one or more spatial dimensions. Both functions account for the variable spatial grid in ROMS. A full description is written by Thyng et al. (2024d). The spatial integrals were calculated over the active zone, i.e. the zone directly affected by OWFs. This zone was manually mapped out for each of the studied parameters.

Chapter 4

Results and Interpretation

From the reduced-gravity model, Broström (2008) underlined the importance of wind farm size on the oceanic response, and that a significant response is expected when the farm size becomes larger than the Rossby radius of deformation. From Eq. (2.7), the Rossby radius of deformation of the numerical setup in this thesis has been calculated to be approximately 4 km. Thus, experiments with farm sizes $L = (5, 10, 2 \times 8$ and $3 \times 8)$ km, are all expected to show noticeable oceanic response.

Generally, all experiments show that the presence of OFWs generates a dipole with upwelling on the southern side and downwelling on the northern side of the farm. From the continuity equation (Eq. (2.13)) in section 2.2.3, it follows that wind-driven convergence and divergence of Ekman transport at the surface must generate a compensating vertical motion (Marshall & Plumb, 2008). The wind farm blocks the wind, creating a wake with reduced wind stress downstream while the wind stress outside the wake remains unchanged. This causes a positive wind stress curl and divergence to be generated on the southern side, and a negative wind stress curl and convergence to be generated on the northern side of the farm (Floeter et al., 2022). This dynamic is illustrated in Fig. 2.6.

The next chapters will dive deeper into the results. The results are divided into three parts; physical properties (surface elevation, normalized surface convergence, vertical velocity and Ekman pumping), thermodynamic- and acoustic properties (temperature, thermocline and sound speed), and biogeochemistry (biological tracers and primary production). Each category of results is presented first for the single-farm layout (experiments 1-8) and then for overlapping wind farms (experiments 9-10). All results are anomalies obtained by subtracting the baseline simulation without farm effects from the experiments with farm effects.

To get a better insight into the total effect of OWFs on the water column, spatial integrals of the different properties have been calculated over the active zone for all experiments. For comparison purposes the experiments with $\tau_{x0} = \Delta\tau = 0.05$ N/m^2 were selected as a reference. All subsequent results were then normalized by this reference; experiments 1-4 against experiment 1 and experiments 5-8 against experiment 5. Experiments 9 and 10 were normalized by themselves. The results are shown in Tables 4.1 to 4.4 and are presented according to the explained categories.

4.1 Physical Properties

Table 4.1: Physical properties integrals. The results of experiments 1-4 are normalized by experiment 1 and the results of experiments 5-8 are normalized by experiment 5. Experiments 9 and 10 are normalized by themselves. The green (—) reference values mean that positive values indicate net upward motion (upwelling) and negative values indicate net downward motion (downwelling). The red (—) reference value means that positive values indicate net downward motion (downwelling) and negative values indicate net upward motion (upwelling).

Experiment	$\int \zeta' \, \mathrm{d}x \, \mathrm{d}y$	$\int (\nabla \cdot u)' \, \mathrm{d}x \, \mathrm{d}y$	$\int w'_{x \approx 55km} \, \mathrm{d}z \, \mathrm{d}y$	$\int \overline{w'}_{depth} \, \mathrm{d}x \, \mathrm{d}y$	$\int w'_{Ek} \, \mathrm{d}x \, \mathrm{d}y$
1	**1.00**	**1.00**	**1.00**	**1.00**	**1.00**
2	0.79	1.44	0.78	0.95	1.00
3	0.65	1.66	0.33	0.79	1.00
4	1.48	3.46	0.45	1.70	2.00
5	**1.00**	**1.00**	**1.00**	**1.00**	**1.00**
6	0.31	1.42	0.76	0.91	1.00
7	-0.17	1.74	0.45	0.80	1.00
8	0.35	3.64	0.77	1.69	2.00
9	**1.00**	**1.00**	**1.00**	**1.00**	**1.00**
10	**1.00**	**1.00**	**1.00**	**1.00**	**1.00**

4.1.1 Surface Elevation

Single Wind Farm Layout

Fig. 4.1 shows the temporal evolution of the sea-surface elevation anomaly for experiment 1 at $0.5, 2, 4$ and 6 days. It is apparent that the presence of the wind farm creates a dipole with upwelling on the southern side and downwelling on the northern side. From Fig. 4.1, it seems as the effect of the wind farm on the sea-surface elevation anomaly increases with time. The results are comparable to the results of Paskyabi & Fer (2012) presented in section 1.4.

Fig. 4.2 shows the sea-surface elevation anomaly at day 6 for experiments 1-8. They all show the same dipole pattern as seen before. The results of experiments $1, 2, 3, 5, 6$ and 7 ($\tau_{x0} = (0.05, 0.08)$ N/m^2 and $\Delta\tau = 0.05$ N/m^2) show no variation in magnitude for the different wind stress parameters. The magnitude of disturbance does, however increase when L is increased from 5 km to 10 km. This indicates that the size of the wind farm is more important for the impact on the local surface elevation than the wind stress strength. The affected area seem to increase slightly with increased wind stress. For strong wind stress and strong wind reduction, i.e. experiments 4 and 8 ($\tau_{x0} = 0.10$ N/m^2 and $\Delta\tau = 0.10$ N/m^2), results show an increased magnitude of surface elevation anomalies. These results indicate that the farm size is a deciding factor, but that the combination of strong wind stress and strong wind stress reduction behind the wake will also contribute to changes in sea-surface elevation.

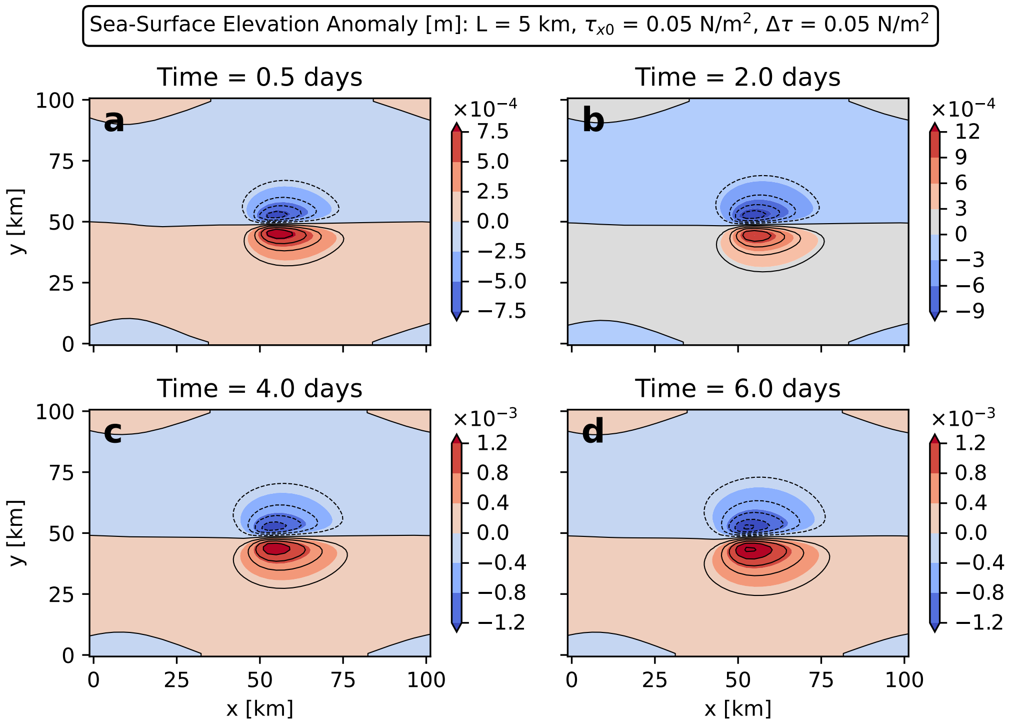

Figure 4.1: Temporal evolution of sea-surface elevation anomaly for experiment 1: $\tau_{x0} = 0.05$ N/m^2, $\Delta\tau = 0.05$ N/m^2 at: a) 0.5 days, b) 2 days, c) 4 days and d) 6 days. OWFs create a dipole pattern with downwelling on the northern side and upwelling on the southern side of the farm.

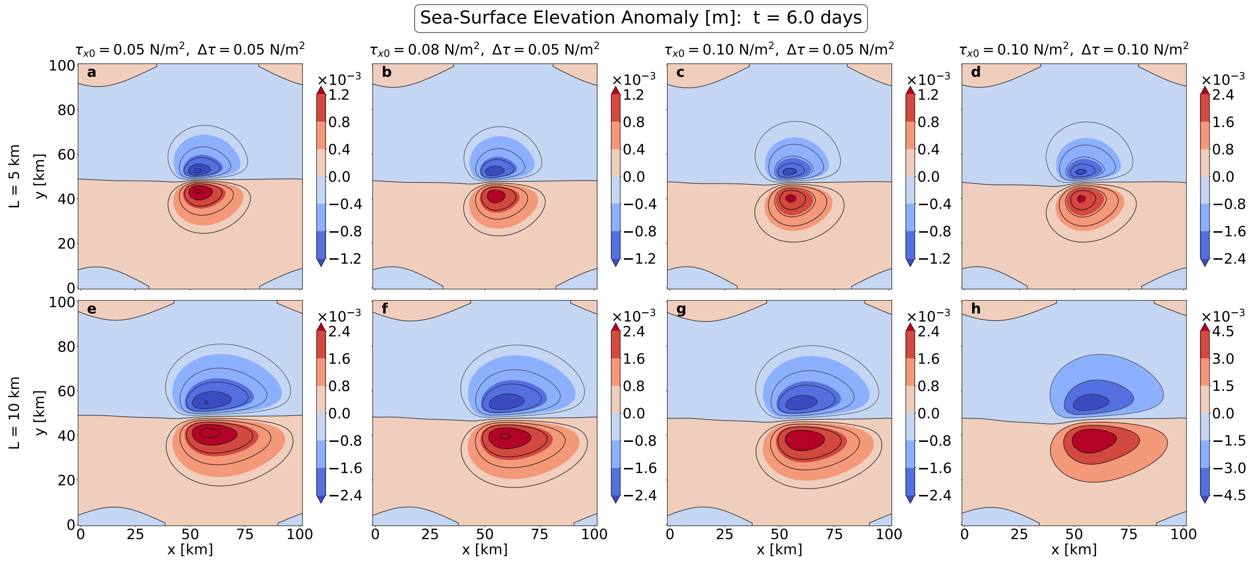

Figure 4.2: Sea-surface elevation anomaly at day 6 for experiments 1-8 for various $\tau_{x0} = (0.05, 0.08, 0.10)$ N/m^2 and $\Delta\tau = (0.05, 0.10)$ N/m^2 as described above each panel. Panels a) to d) experiments 1-4 ($L = 5$ km), panels e) to h) experiments 5-8 ($L = 10$ km). The dipole is apparent in all experiments.

Overlapping Wind Farms

The results of experiments 9 and 10 are shown in Fig. 4.3. Also here, the results indicate that the size, here the number of overlapping farms, is a deciding factor for the magnitude of the disturbance of the sea-surface elevation. For these two experiments, $\tau_{x0} = 0.10$ N/m^2 and $\Delta\tau = 0.05$ N/m^2. Thus, the results at 6 days can be easily compared to experiments 3 and 7. For single-farm layout with $L = 5$ km and $L = 10$ km, the sea-surface elevation anomaly ranges between $(-1.2\text{-}1.2) \times 10^{-3}$ m and $(-2.4\text{-}2.4) \times 10^{-3}$ m, respectively. For overlapping wind farms with $L = 2 \times 8$ km and $L = 3 \times 8$ km, the sea-surface elevation anomaly ranges between $(-3\text{-}3) \times 10^{-3}$ m and $(-3\text{-}4.5) \times 10^{-3}$ m, respectively. These results indicate that the size of the wind farm is an important factor for both the magnitude of the disturbance of the sea-surface elevation, and for the size of the affected area. The results also indicate that the layout of the OWFs, or more precisely, the magnitude of wind stress reduction, is of importance; from Fig. 3.2, it can be seen that the wind stress reduction is larger behind farm II than for the other farms due to the overlapping effect. Following the Ekman theory discussed above and in section 2.2.3 this generates a stronger wind stress curl and stronger horizontal Ekman transport at the surface, and thus a stronger vertical motion. This can explain why the overlapping farms show larger magnitudes of disturbance than the single-farm layouts.

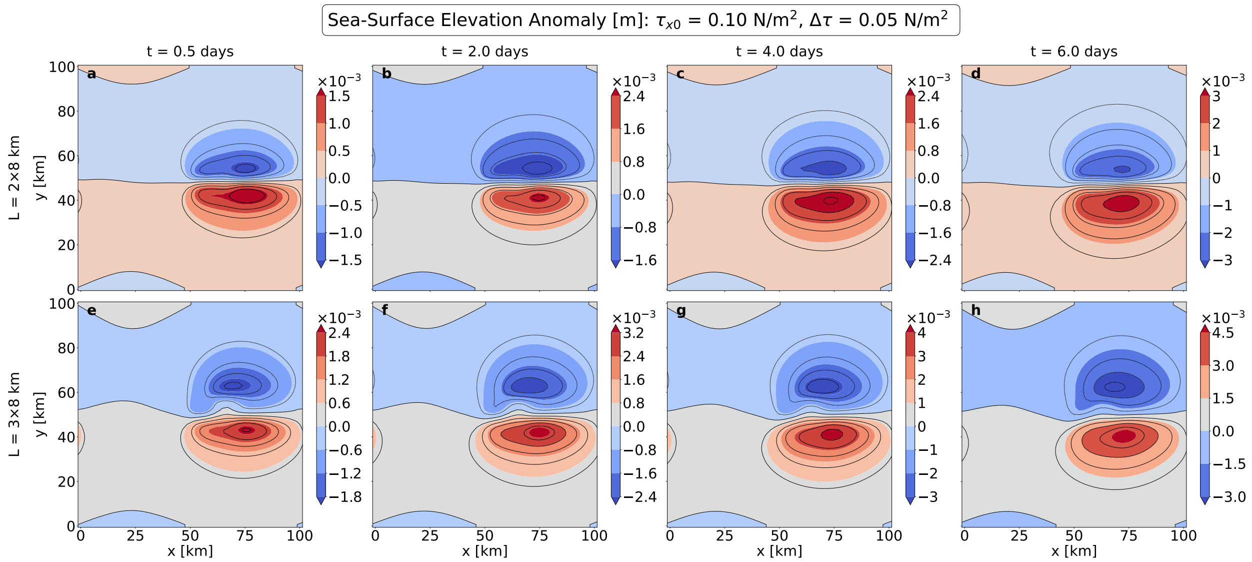

Figure 4.3: Temporal evolution of sea-surface elevation anomaly at day 0.5, 2, 4 and 6 for experiments 9-10 ($\tau_{x0} = 0.10$ N/m^2 and $\Delta\tau = 0.05$ N/m^2). Panels a) to d) show the results for two overlapping farms with $L = 8$ km and panels e) to h) show the result for three overlapping farms with $L = 8$ km. The dipole is apparent for both experiments.

Integral Over Active Zone

The first integral in Table 4.1 gives information on the net sea-surface elevation anomaly across the active zone in the horizontal x- and y-direction. Here, 1 indicates a net positive sea-surface elevation across the active zone. Values > 1 indicate a greater net positive elevation, values < 1 indicate decreased but still positive elevation anomaly, and values < 0 means a net negative surface elevation anomaly. As a reminder, in this particular notation, positive and negative sea-surface elevation anomalies correspond to upwelling and downwelling zones, respectively. The results of the integral indicate that there is a net positive surface elevation (i.e. net upwelling) for all experiments except for experiment 7. For $L = 5$ km it seems that the experiment with the combination of strong wind stress and strong wind stress reduction ($\tau_{x0} = \Delta\tau = 0.10$ N/m^2) deviates the most from the baseline. The same pattern is not found for $L = 10$ km. It must be noted that the active zones have been chosen manually, which means some details can potentially have been missed. The results must be seen in relation to the other presented results. However, the results suggests that OWFs generally generates a local net upwelling.

4.1.2 Normalized Surface Convergence

Continuing the discussion of the sea-surface elevation anomaly, lets now take a closer look at the normalized surface convergence anomaly.

Single Wind Farm Layout

Fig. 4.4 shows the temporal evolution of normalized surface horizontal convergence anomaly for experiment 1 for $0.5, 2, 4$ and 6 days. The same dipole pattern is seen here, with a convergence (downwelling) zone on the northern side and a divergence (upwelling) zone on the southern side of the farm. The results show only small variations with time.

The normalized surface horizontal convergence anomaly at day 6 for experiments 1-8 is shown in Fig. 4.5. For $\tau_{x0} = (0.05, 0.08, 0.10)$ N/m^2 and $\Delta\tau = 0.05$ N/m^2, only small variations in horizontal convergence anomaly are seen. When increasing the wind stress parameters to $\tau_{x0} = \Delta\tau = 0.10$ N/m^2, the magnitude of disturbance increases from approximately $(-1.05\text{-}0.3) \times 10^{-2}$ to $(-2.4\text{-}0.4) \times 10^{-2}$ for $L = 5$ km and from approximately $(-7.2\text{-}2.4) \times 10^{-3}$ to $(-1.8\text{-}0.6) \times 10^{-2}$ for $L = 10$ km. Thus, the magnitude of wind stress reduction seems to be important. This is in alignment with Broström (2008), which states that the circulation is driven primarily by spatial variation in wind stress rather than by the magnitude of wind stress. However, it seems as the wind farm size is more important than the wind stress parameters for the magnitude of the disturbance, as well as for the affected area. The results indicate that the magnitude of the disturbance is larger for $L = 5$ km, however the affected area is larger for $L = 10$ km. This is in alignment with the Ekman theory from section 2.2.3 and Eq. (3.4); the larger wind farms have larger wake areas, but approximately the same amplitude of decreased wind stress due to the Gaussian wake model. In other words, the same wind stress curl is for $L = 10$ km stretched over a larger area, which results in a weaker divergence/convergence. Note that the magnitude of the surface convergence zone on the northern side of the farm is stronger than the magnitude of the divergence zone on the southern side of the farm.

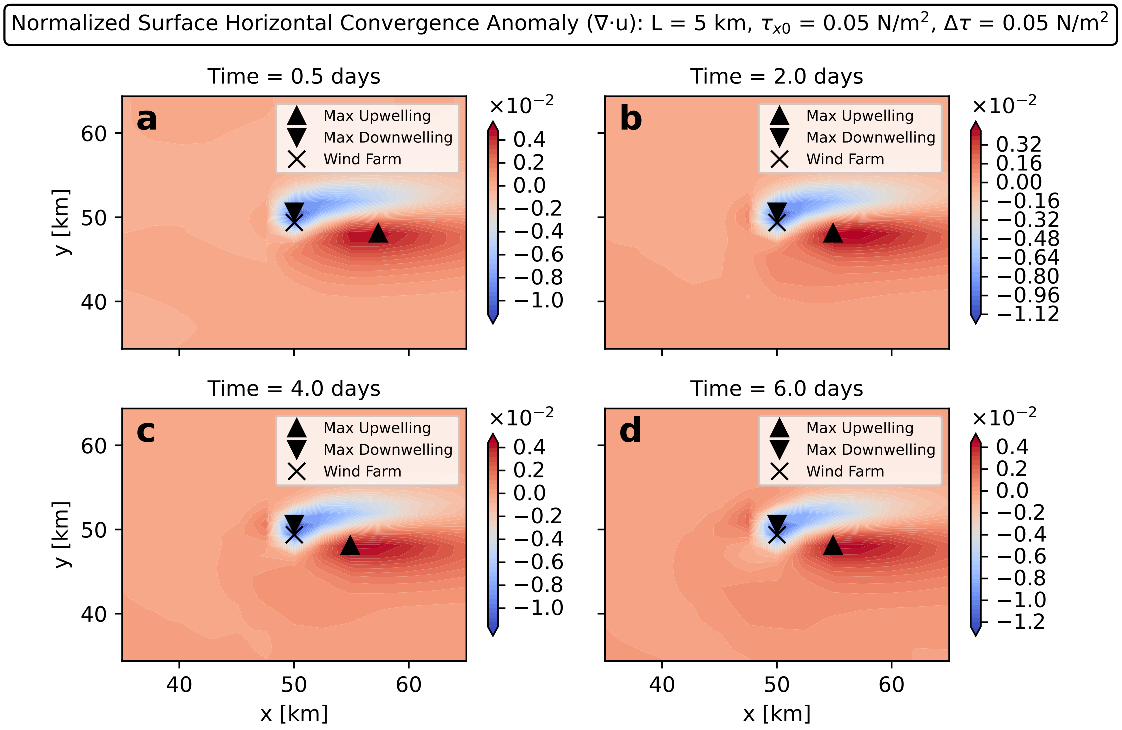

Figure 4.4: Normalized surface horizontal convergence anomaly for experiment 1 at a) 0.5 days, b) 2 days, c) 4 days and d) 6 days. A dipole pattern is created with downwelling on the northern side and upwelling on the southern side of the farm.

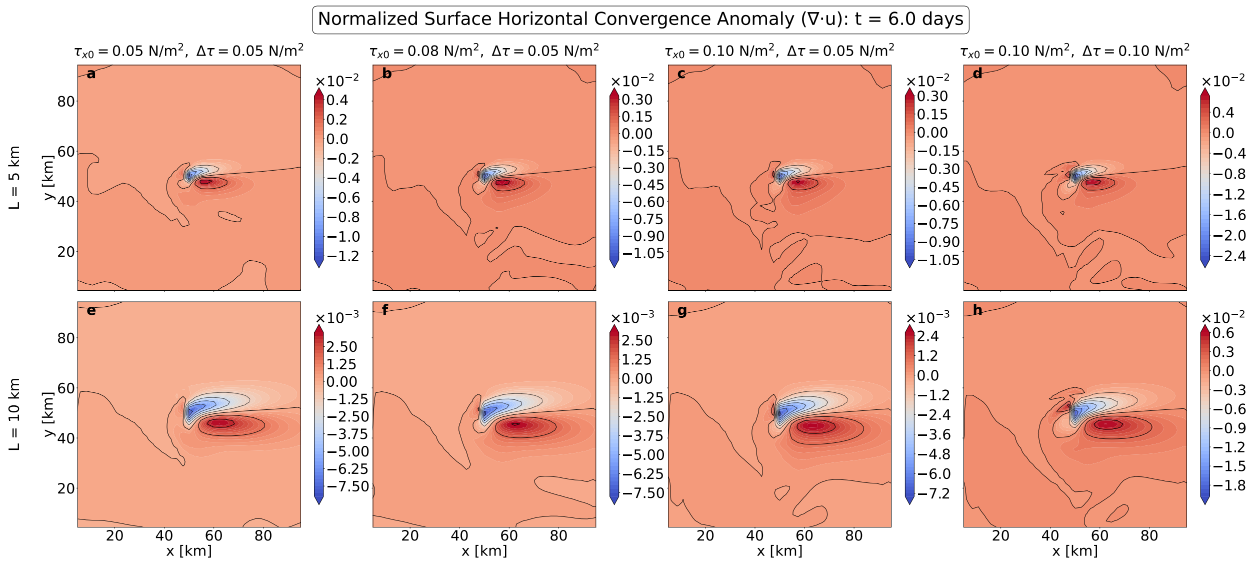

Figure 4.5: Normalized surface horizontal convergence anomaly at day 6 for experiments 1-8 for various $\tau_{x0} = (0.05, 0.08, 0.10)$ N/m^2 and $\Delta\tau = (0.05, 0.10)$ N/m^2 as described above each panel. Panels a) to d) experiments 1-4 ($L = 5$ km), panels e) to h) experiments 5-8 ($L = 10$ km). The dipole is apparent in all experiments.

A cross-section of the maximum upwelling and downwelling for experiments 1-8 is shown in Fig. 4.6. This figure gives the same information as Fig. 4.5; the upper panels indicate that the combination of strong wind stress and strong wind reduction in the wake contributes to stronger convergence and downwelling. For the other wind stresses, only small variations are found. The upper panels also indicate that the convergence is stronger for $L = 5$ km than for $L = 10$ km, however the affected area is larger for $L = 10$ km. This can be seen in panel c), where the peaks are wider but shorter than in panel a). The bottom panels show the maximum values of the normalized horizontal surface divergence. Also here, the combination of strong wind stress and strong wind reduction is associated with the larger magnitudes of divergence than for the other wind stresses. However, the difference is less than for maximum convergence. For experiment 8 ($L = 10$ km, $\tau_{x0} = \Delta\tau = 0.10$ N/m^2), the maximum divergence is also located at a different x-value than the other experiments. Like shown in Fig. 4.5, the cross-section shows that the magnitude of the convergence is stronger than the magnitude of the divergence.

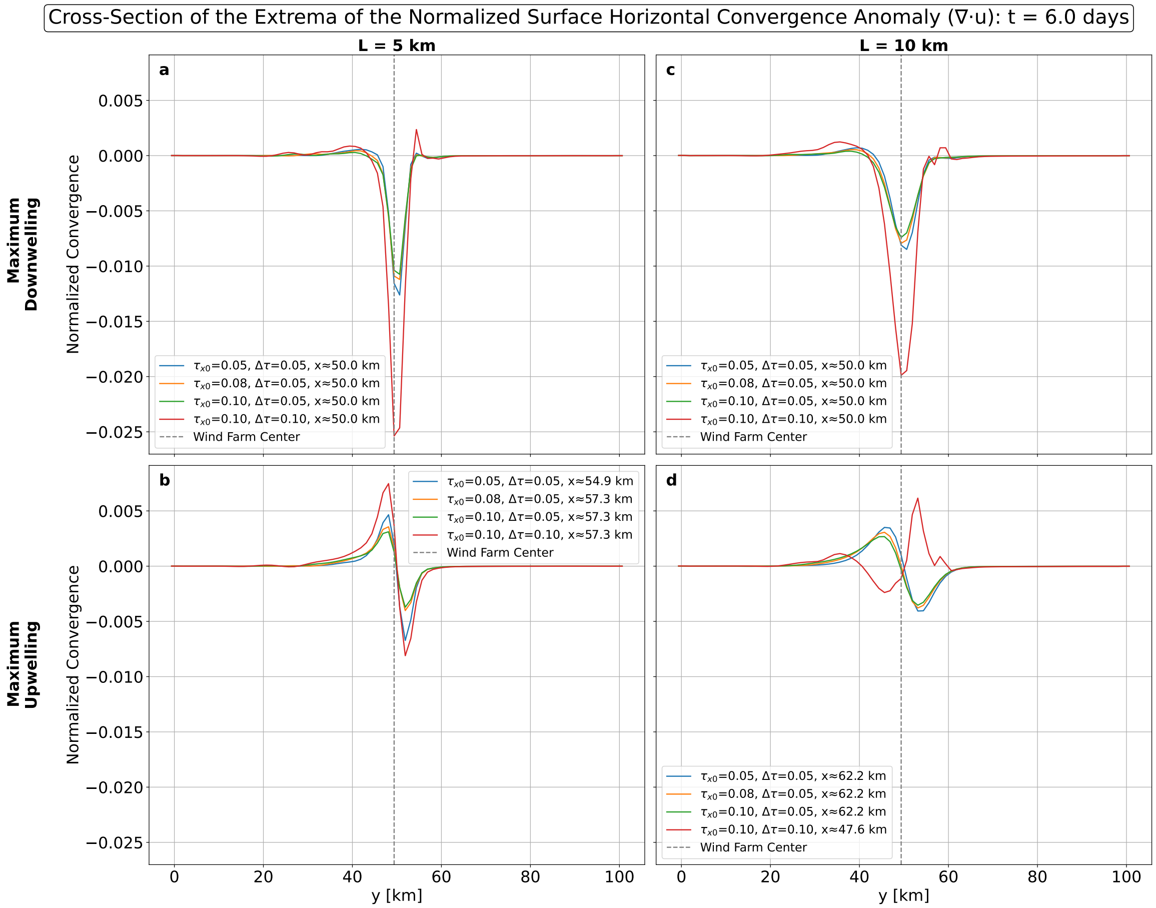

Figure 4.6: Cross-section of the extrema of the normalized surface horizontal convergence anomaly for experiments 1-8. Panels a) and c) show the maximum convergence (downwelling) values for experiments 1-4 (—, —,— and —) and experiments 5-8 (—, —,— and —), respectively. Panels b) and d) show the maximum divergence (upwelling) values for experiments 1-4 (—, —,— and —) and experiments 5-8 (—, —,— and —), respectively.

Overlapping Wind Farms

The normalized surface horizontal convergence anomaly and the cross-section of the extrema of the normalized surface horizontal convergence anomaly for experiments 9 and 10 are shown in Fig. 4.7 and Fig. 4.8, respectively. They both indicate that there is little variation in surface convergence for two overlapping wind farms compared to three overlapping wind farms at day 6. The normalized convergence ranges between $(-7.5\text{-}3) \times 10^{-3}$ for both experiments. The affected area is, however, larger for three overlapping wind farms than for two overlapping wind farms. It can also be seen that the magnitude of the convergence zone is stronger than the magnitude of the divergence zone. In addition, compared to single-farm experiment 7, the reduction in magnitude of disturbance for overlapping farms is not as pronounced as the reduction seen between experiments 3 and 7. In fact, the normalized surface convergence anomaly is stronger for overlapping farms than for experiment 7. This can be due to the stronger wind stress reduction in farm II.

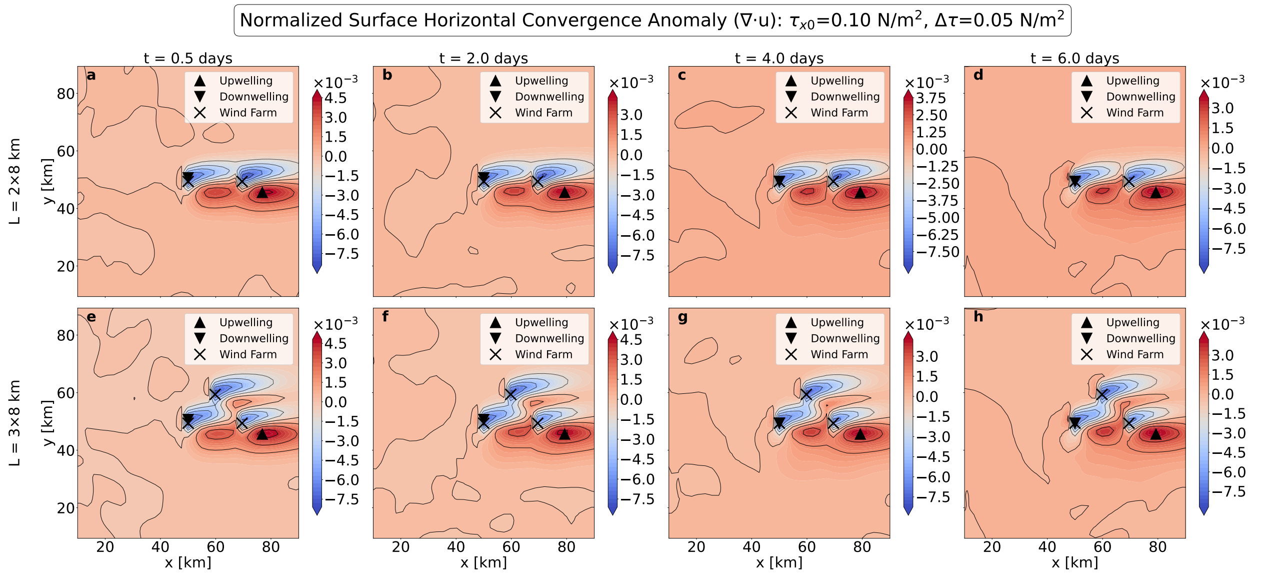

Figure 4.7: Temporal evolution of normalized surface horizontal convergence anomaly at day 0.5, 2, 4 and 6 for experiments 9-10 ($\tau_{x0} = 0.10$ N/m^2 and $\Delta\tau = 0.05$ N/m^2). Panels a) to d) show the results for two overlapping farms with $L = 8$ km and panels e) to h) show the result for three overlapping farms with $L = 8$ km.

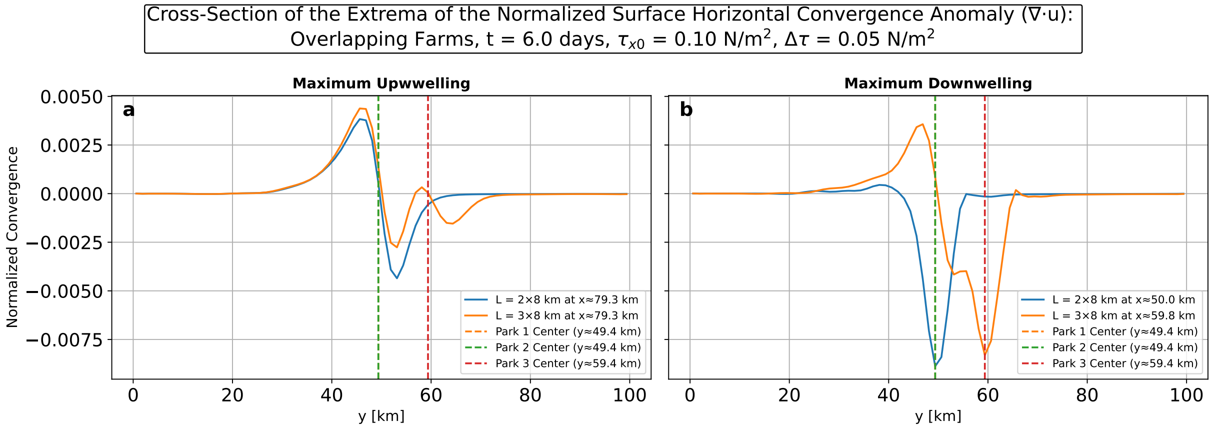

Figure 4.8: Cross-section of the extrema of the normalized surface horizontal convergence anomaly for experiments 9-10. Panel a) shows the maximum divergence values for experiments 9 (—) and 10 (—). Panel b) shows the maximum convergence values for experiments 9 (—) and 10 (—).

In summary, the results indicate that the magnitude of the normalized surface horizontal convergence anomaly decreases as the size of the wind farm increases, but increases when the wind stress reduction increases. This is in alignment with the theory discussed in section 2.2.3 and Eq. (3.4). In addition, the affected area increases as the size of the wind farm increases. Also, the magnitude of the convergence zone is stronger than the magnitude of the divergence zone.

Integral Over Active Zone

The second integral in Table 4.1 gives information on the net normalized horizontal convergence anomaly across the active zone for experiments 1-10. Here, 1 indicates net convergence (i.e. downwelling), values < 1 but > 0 indicate net convergence but decreased compared to the reference, values > 1 indicate increased net convergence compared to the reference, and values < 0 indicate divergence and upwelling. Both sets of single-farm experiments ($L = 5$ km and $L = 10$ km) show a similar pattern where the surface convergence anomaly grows stronger as the wind stress parameters are increased. All 10 experiments show positive values, which here means net convergence (i.e. downwelling) across the selected active zone. The strongest surface convergence is seen for the experiments with the combination of strong wind stress and strong wind stress reduction ($\tau_{x0} = \Delta\tau = 0.10$ N/m^2). This aligns well with the results presented in Fig. 4.6, Fig. 4.7 and with the study of Broström (2008) where it is stated that the circulation is driven primarily by the magnitude of wind stress curl rather than the magnitude of wind stress itself. The results does, however, not align with the results of the sea-surface elevation discussed above. One potential explanation could be that net surface convergence induces downwelling in the uppermost layers just below the surface, whereas vertical motion at greater depths contributes to a net upwelling when integrated over the entire water column. If so, the results would be in alignment with the net sea-surface elevation. This idea will be further explored when discussing the vertical velocity.

4.1.3 Vertical Velocity

As established above and in the Ekman theory in section 2.2.3, the surface convergence and divergence are related to vertical mass transport (Marshall & Plumb, 2008). Thus, it is expected that the vertical velocity follows a pattern that corresponds to the horizontal surface convergence.

The vertical velocity analysis involved examining the depth-averaged vertical velocity, a cross-section of the vertical velocity at $x \approx 55$ km and a horizontal section of the vertical velocity at $z = -11$ m. This provides valuable information on how the vertical velocity acts through the entire water column.

Single Wind Farm Layout

Fig. 4.9 shows the vertical velocity anomaly at 11 meters below the surface for experiments 1-8 at day 6. The results indicate that the magnitude of the vertical velocity at 11 meters depth seems to decrease as the wind stress is increased. However, the magnitude of the vertical velocity increases in the scenario of both strong wind stress and strong wind stress reduction. This is in alignment with Broström (2008), where it is stated that spatial variations in wind stress are more important for the circulation than the magnitude of the wind stress itself. It is also in alignment with the Ekman theory (Eq. (2.13)) that describes that the vertical motion depends on the wind stress curl at the surface (Marshall & Plumb, 2008). In addition, as seen before, it seems as the characteristic farm length is an important factor also here. The magnitude of the vertical velocity is lower for $L = 10$ km than for $L = 5$ km. The affected area is, however, larger for $L = 10$ km. The magnitude of the negative vertical velocity anomaly is larger than the positive anomaly, which indicates stronger downwelling than upwelling at this depth (11 m). These results are in alignment with the results of the horizontal surface convergence anomalies.

Fig. 4.10 shows depth-averaged vertical velocity anomaly and Fig. 4.11 shows the cross-section of vertical velocity anomaly at $x \approx 55$ km, both for experiments 1-8 at day 6. These two figures give information on the total vertical velocity in the entire water column. The results indicate that for $L = 5$ km the magnitude is stronger close to the surface than for $L = 10$ km, whereas the opposite is true further down the water column. The affected area also increases along with L in both the vertical and horizontal direction. This is why the depth-averaged results in Fig. 4.10 show larger anomalies for $L = 10$ km than for $L = 5$ km whereas Fig. 4.9 shows the opposite. This indicates that larger wind farms are able to generate vertical motion that reaches further down the water column and covers a larger horizontal area than smaller wind farms. The experiments with strong wind stress and strong wind stress reduction (experiments 4 and 8, $\tau_{x0} = \Delta\tau = 0.10$ N/m^2), show the strongest magnitude of vertical velocity anomaly for both the surface and greater depths. As stated above, this is in alignment with Broström (2008). The negative anomalies are stronger than the positive anomalies for all experiments, however the difference is smaller for the depth-averaged data.

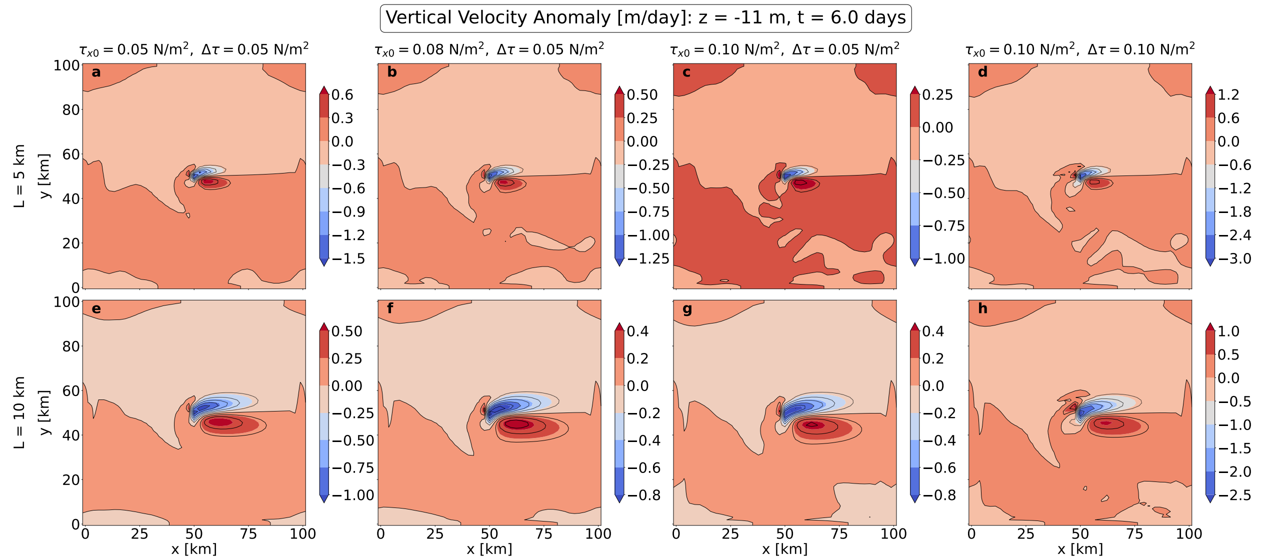

Figure 4.9: Vertical velocity anomaly at $z = -11$ m at day 6 for experiments 1-8 for various $\tau_{x0} = (0.05, 0.08, 0.10)$ N/m^2 and $\Delta\tau = (0.05, 0.10)$ N/m^2 as described above each panel. Panels a) to d) experiments 1-4 ($L = 5$ km), panels e) to h) experiments 5-8 ($L = 10$ km). OWFs create a dipole with downwelling on the northern side and upwelling on the southern side of the farm.

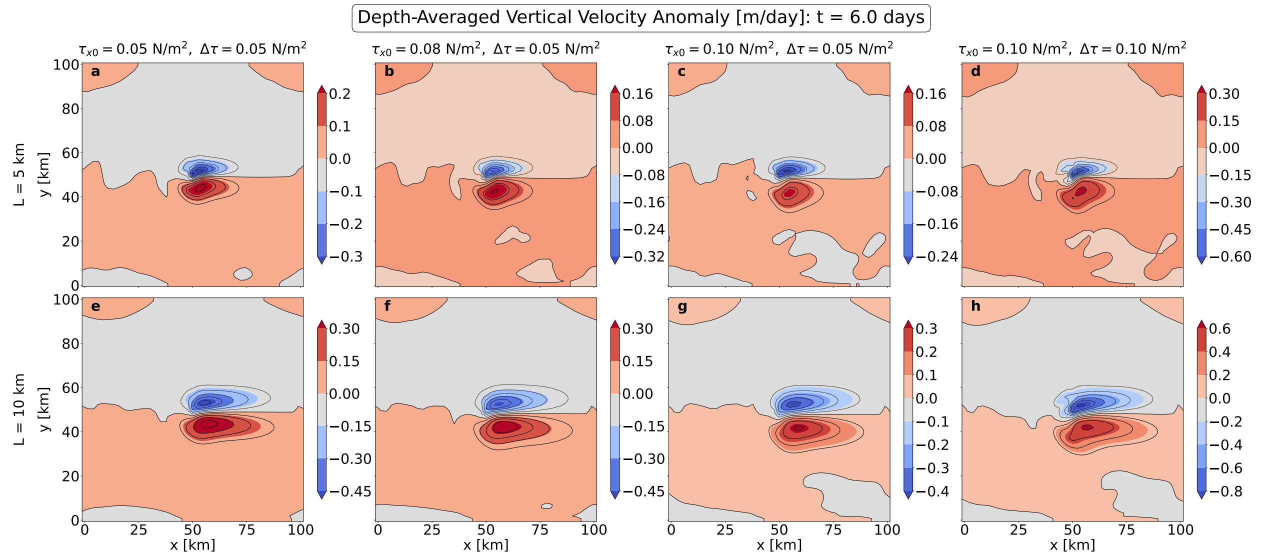

Figure 4.10: Depth-averaged vertical velocity anomaly at day 6 for experiments 1-8 for various $\tau_{x0} = (0.05, 0.08, 0.10)$ N/m^2 and $\Delta\tau = (0.05, 0.10)$ N/m^2 as described above each panel. Panels a) to d) experiments 1-4 ($L = 5$ km), panels e) to h) experiments 5-8 ($L = 10$ km). A dipole pattern is seen with downwelling on the northern side and upwelling on the southern side of the farm.

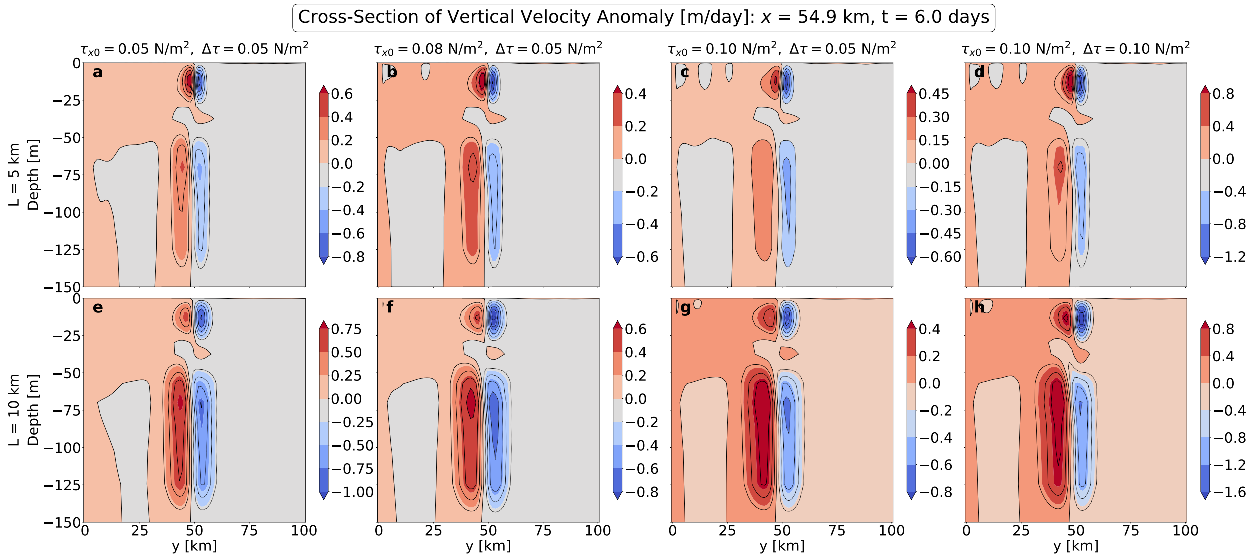

Figure 4.11: Cross-section of vertical velocity anomaly at $x \approx 55$ km at day 6 for experiments 1-8 for various $\tau_{x0} = (0.05, 0.08, 0.10)$ N/m^2 and $\Delta\tau = (0.05, 0.10)$ N/m^2 as described above each panel. Panels a) to d) experiments 1-4 ($L = 5$ km), panels e) to h) experiments 5-8 ($L = 10$ km). A dipole pattern is seen both above and below the thermocline, showing downwelling on the northern side and upwelling on the southern side of the farm.

Overlapping Wind Farms

Fig. 4.12 shows the temporal evolution of depth-averaged vertical velocity anomaly for experiments 9 and 10. The results show little variation in magnitude between the two scenarios. The affected area is larger for three overlapping farms than for two overlapping farms. If comparing the results at day 6 with the results for $L = 5$ km and $L = 10$ km ($\tau_{x0} = 0.10$ N/m^2, $\Delta\tau = 0.05$ N/m^2) the total disturbance on the entire water column seems to increase as the farm size increases.

Fig. 4.13 shows the temporal evolution of the cross-section of vertical velocity anomaly at $x \approx 55$ km for experiments 9 and 10. At day 6 the magnitude of the velocity anomaly is similar for both farms, and the results show little variation in magnitude from the single-farm layout experiments with the same wind stress parameters. However, the affected area is larger for three overlapping farms than for two overlapping farms. The cross-section for three overlapping farms also shows two upwelling cells close to the surface and two downwelling cells further down. Note that Fig. 4.13 only gives insight into the cross-section for one specific x-value. Thus, it essentially does not capture the total dynamics of the overlapping farms. Based on the additional wind stress reduction seen in Fig. 3.2, Broström (2008) and the Ekman theory (Eq. (2.13)) from section 2.2.3, a greater difference between overlapping-farm and single-farm experiments would be expected to be seen by including a cross-section through wind farm II.

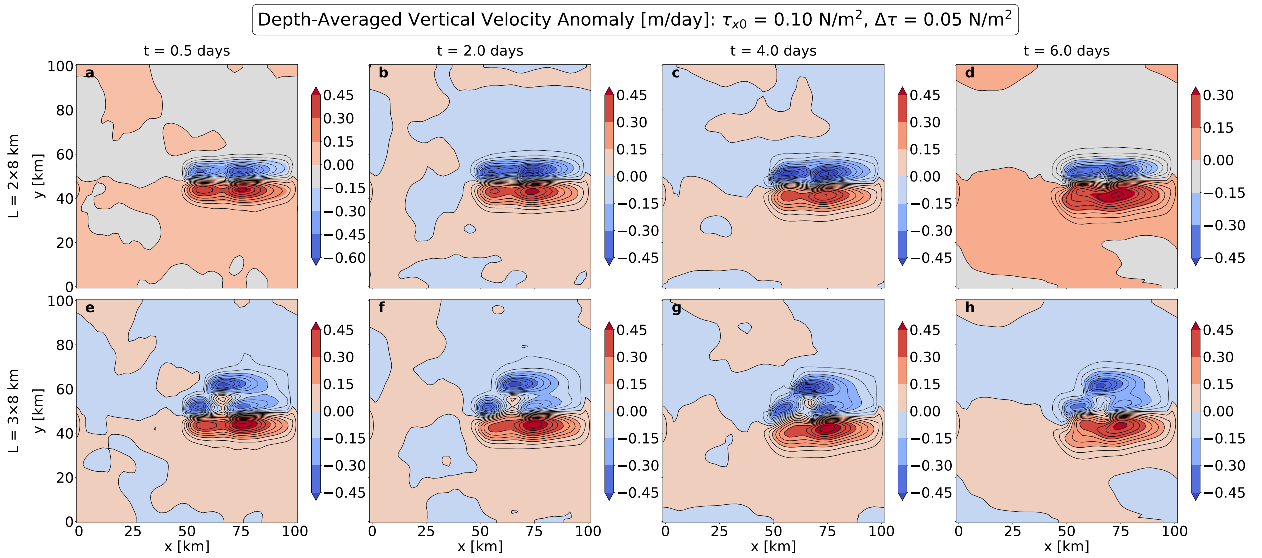

Figure 4.12: Temporal evolution of depth-averaged vertical velocity anomaly at day 0.5, 2, 4 and 6 for experiments 9-10 ($\tau_{x0} = 0.10$ N/m^2 and $\Delta\tau = 0.05$ N/m^2). Panels a) to d) show the results for two overlapping farms with $L = 8$ km and panels e) to h) show the result for three overlapping farms with $L = 8$ km.

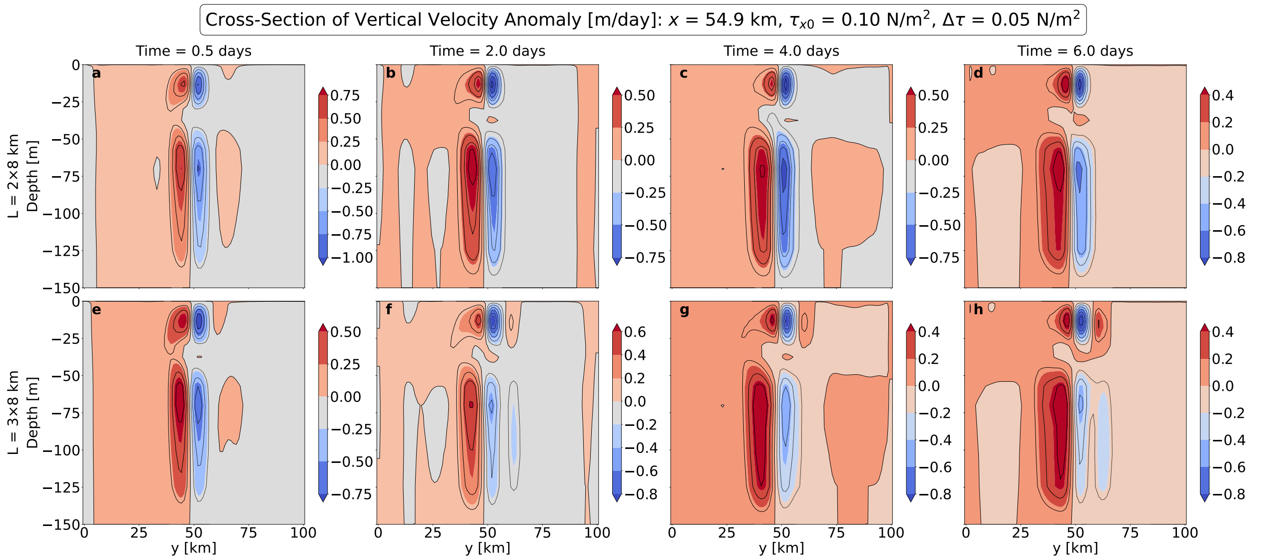

Figure 4.13: Temporal evolution of cross-section of vertical velocity anomaly at $x \approx 55$ km at day 0.5, 2, 4 and 6 for experiments 9-10 ($\tau_{x0} = 0.10$ N/m^2 and $\Delta\tau = 0.05$ N/m^2). Panels a) to d) show the results for two overlapping farms with $L = 8$ km and panels e) to h) show the result for three overlapping farms with $L = 8$ km.

Integral Over Active Zone

The third integral in Table 4.1 gives information on the net effect of the vertical velocity in the entire water column for one specific x-value, $x \approx 55$ km. In alignment with the results of the surface elevation integral, all experiments have a net positive vertical velocity, which here indicates net upward motion. This imbalance has been explained by Liu et al. (2023); due to horizontal Ekman transport, the water in the downwelling zone north of the farm is carried towards the south while being pushed downward through the water column. This convergence of water on the southern side of the farm then amplifies the upwelling driven by the surface wind stress curl. This can also be seen in Fig. 4.11; the figures are mostly red, which is why all the integrals have positive values. The downward motions (negative values, shown in blue) have, however, larger magnitudes. If looking at only the dipoles above the thermocline (i.e. above the gap at around 20-30 m depth), the downwelling zone seem stronger than the upwelling zone. Further down, the opposite seem to be true. This can help explain why the integral of vertical velocity shows net upwelling while the integral of surface convergence shows net downwelling. These findings strengthen the idea that different dynamical processes can occur at different depths. It is however also worth noting that cross-sections only capture a very limited part of the farms.

The fourth integral gives information on the net spatial effect of the depth-averaged vertical velocity. Also here, all values are positive which indicate net upwelling. This is also in alignment with the findings of Liu et al. (2023). The largest disturbance for the single-farm experiments can be seen for experiments 4 and 8 with strong wind stress and strong wind stress reduction ($\tau_{x0} = \Delta\tau = 0.10$ N/m^2). As explained above, this is in alignment with both Broström (2008) and well as Eq. (2.13) from section 2.2.3.

4.1.4 Ekman Pumping

Ekman pumping is, as described in section 2.2.3, the result of wind-driven divergence and convergence of Ekman transport on the surface (Marshall & Plumb, 2008). It is therefore expected that the vertical Ekman pumping follows the same pattern as the surface convergence, with stronger vertical transport for $L = 5$ km than for $L = 10$ km.

Single Wind Farm Layout

Fig. 4.14 shows the vertical Ekman pumping for experiments 1-8 at day 6. As expected based on the result of the horizontal convergence anomaly, the results show little variation between experiments 1-3 and experiments 5-7. For both $L = 5$ km and $L = 10$ km the Ekman pumping increases for experiments 4 and 8 with combination of strong wind stress and strong wind stress reduction ($\tau_{x0} = \Delta\tau = 0.10$ N/m^2). As expected, the results also indicate that the Ekman pumping decreases when the farm size increases, but the affected area gets larger. This is in alignment with the results of the normalized surface horizontal convergence anomaly, the vertical velocity anomaly at 11 m, and it is also in alignment with the Ekman theory based on Marshall & Plumb (2008) discussed in section 2.2.3; the magnitude of horizontal Ekman transport (Eq. (2.12)) is proportional with the magnitude of the surface wind stress. This means that the Ekman transport is weaker inside the wake behind the wind farm than outside. This locally generated wind stress curl on each side of the farm drives a vertical Ekman pumping (Eq. (2.14)). The magnitude of the vertical Ekman pumping is directly determined by the magnitude of the wind stress curl. For experiments 1-3 and 5-7, the wind stress reduction $\Delta\tau$ is kept constant. Thus, the wind stress curl and thereby the Ekman pumping will remain constant as well. Stronger wakes, i.e. stronger wind stress reduction, generates stronger wind stress curl at the outer edges of the wake. Consequently, the magnitude of the vertical Ekman pumping on both sides of the farm will increase. This is seen for experiments 4 and 8.

In realistic scenarios, it is reasonable to believe that larger wind farms have stronger and longer wakes and that the vertical Ekman pumping increases as a result. However, the results presented here show that the opposite is true, at least for idealized cases. Firstly, the Gaussian wake model has limitations. The stress reduction $\Delta\tau$ is kept constant, which means that the amplitude of the wake is approximately the same for both $L = 5$ km and $L = 10$ km while the size of the wake has doubled in size. Thus, essentially what happens for $L = 10$ km compared to $L = 5$ km, is that the same wind stress is stretched over a distance twice as long. According to Eq. (2.14), this results in a vertical Ekman pumping half the magnitude. Because the affected area increases, the net vertical Ekman pumping may still increase for $L = 10$ km compared to $L = 5$.

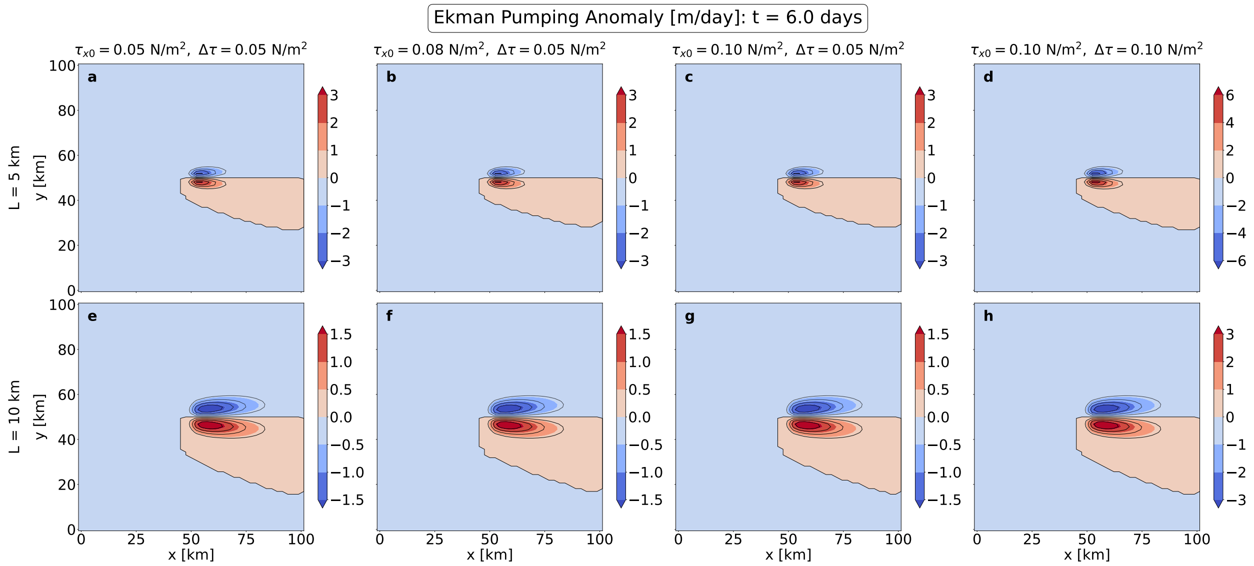

Figure 4.14: Ekman pumping at day 6 for experiments 1-8 for various $\tau_{x0} = (0.05, 0.08, 0.10)$ N/m^2 and $\Delta\tau = (0.05, 0.10)$ N/m^2 as described above each panel. Panels a) to d) experiments 1-4 ($L = 5$ km), panels e) to h) experiments 5-8 ($L = 10$ km). OWFs create a dipole with downwelling on the northern side and upwelling on the southern side of the farm.

Overlapping Wind Farms

Fig. 4.15 shows the Ekman pumping anomaly for experiments 9 and 10 at day 6. The results indicate that there is no difference between the magnitude of the positive vertical Ekman pumping between two and three overlapping farms. For the downwards vertical Ekman pumping, the maximum magnitude is -1.6 m/day for three overlapping farms and -2.4 m/day for two overlapping farms.

This aligns with the results of the surface convergence, as well as with the theory discussed above. The affected area is larger for the three overlapping farms than for the two overlapping farms. Comparing the results to the single-farm experiments with the same wind stress parameters, the Ekman pumping anomaly of the overlapping farms lies between the single-farm layout with $L = 5$ km and the single-farm layout with $L = 10$ km. This could be because the Gaussian wake model has been implemented multiple times, which increases both the total farm area and the reduction of wind stress inside the wake compared to the single-layout farms.

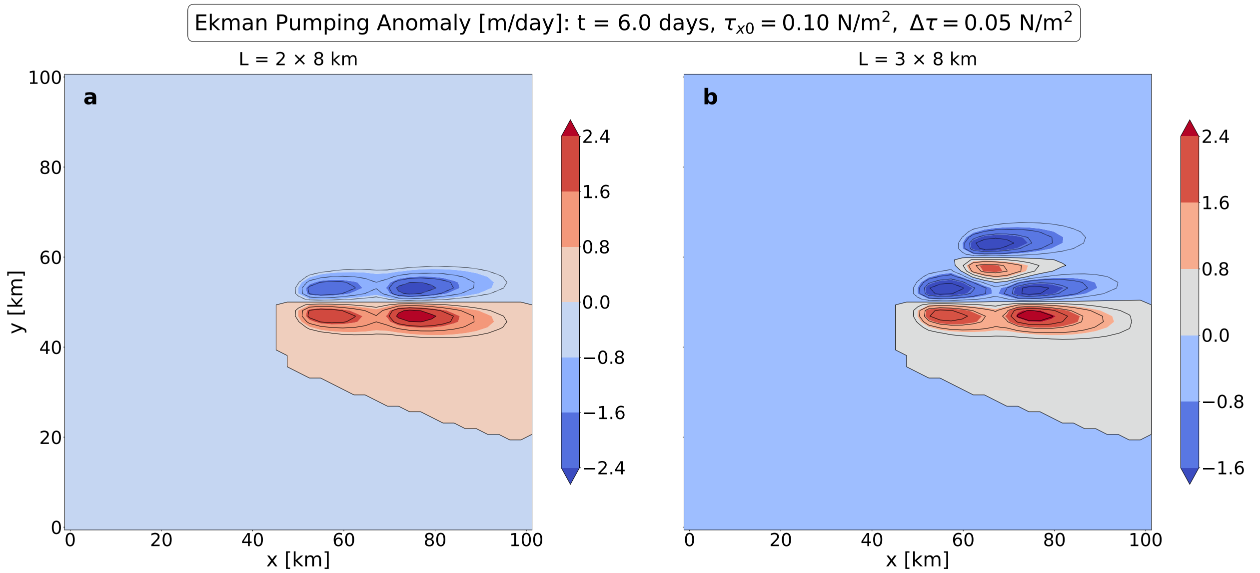

Figure 4.15: Ekman pumping anomaly at day 6 for experiments 9-10 ($\tau_{x0} = 0.10$ N/m^2 and $\Delta\tau = 0.05$ N/m^2). Panel a) shows the results for two overlapping farms with $L = 8$ km and panel b) shows the result for three overlapping farms with $L = 8$ km.

Thus, in regards to Ekman pumping, it seems that the size of the wind farm and the magnitude of the wind stress reduction in the wake are the determining factors for both the intensity and the spatial distribution. This is a direct consequence of the Ekman theory presented in section 2.2.3.

Integral Over Active Zone

The last integral in Table 4.1 gives information on the net horizontal spatial effect of the vertical Ekman pumping over the active zone. The results align with the findings shown in Figs. 4.14 and 4.15. All values are positive, which indicate net upwelling. This is in alignment with the vertical velocity and sea-surface elevation. As expected based on the discussion above, the largest disturbances for the single-farm layouts are seen for strong wind stress and strong wind stress reduction (experiments 4 and 8).

4.2 Thermodynamic- and Acoustic Properties

The disturbances created by OWFs on the physical properties discussed in section 4.1 can also affect the distribution of temperature, the thermocline and sound speed in the water column. This will be studied and discussed here.

Table 4.2: Thermodynamic- and acoustic properties integrals. The results of experiments 1-4 are normalized by experiment 1 and the results of experiments 5-8 are normalized by experiment 5. Experiments 9 and 10 are normalized by themselves. The green (—) reference value means that positive values indicate net increase of the properties and negative values indicate net decrease of the properties. The red (—) reference values mean that positive values indicate net decrease of the properties and negative values indicate net increase of the properties.

Experiment	$\int \overline{T'}_{depth}\,\mathrm{d}x\,\mathrm{d}y$	$\int T'_{x\approx 55km}\,\mathrm{d}z\,\mathrm{d}y$	$\int T'_{cline}\,\mathrm{d}x\,\mathrm{d}y$	$\int c'_{z=2.6m}\,\mathrm{d}x\,\mathrm{d}y$
1	**1.00**	**1.00**	**1.00**	**1.00**
2	1.04	1.09	0.56	0.44
3	1.06	1.12	0.28	0.27
4	2.41	2.68	0.73	1.50
5	**1.00**	**1.00**	**1.00**	**1.00**
6	1.17	1.08	-2.19	0.30
7	1.28	1.12	-4.26	0.05
8	2.92	4.08	-7.51	1.21
9	**1.00**	**1.00**	**1.00**	**1.00**
10	**1.00**	**1.00**	**1.00**	**1.00**

4.2.1 Temperature

Single Wind Farm Layout

Fig. 4.16 shows the temporal evolution of the depth-averaged temperature anomaly for experiment 1. The results show that the magnitude of the temperature disturbance through the water column increases with time. The affected area also increases.

Fig. 4.17 shows the depth-averaged temperature anomaly at day 6 for experiments 1-8. The results indicate that the size of the wind farm is a deciding factor for both the magnitude of temperature disturbance across the water column, and the size of the affected area. In addition, it seems that the combination of strong wind stress and strong wind reduction ($\tau_{x0} = \Delta\tau = 0.10$ N/m^2) further increases the disturbance. This is in alignment with the depth-averaged vertical velocity anomaly discussed in section 4.1, as the temperature is being redistributed by the changes in vertical velocity. The magnitude is approximately the same for positive and negative anomalies.

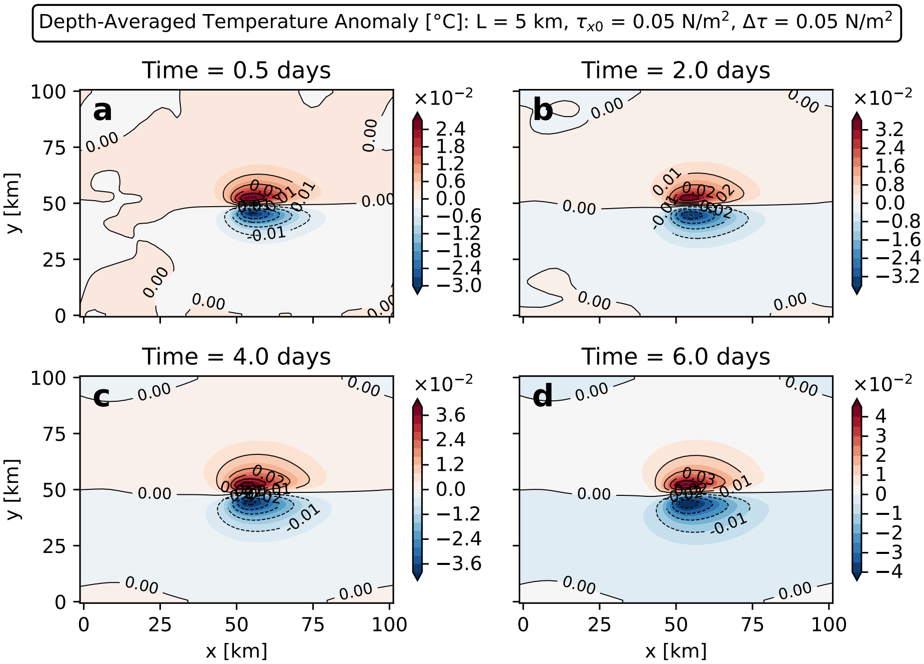

Figure 4.16: Temporal evolution of depth-averaged temperature anomaly for experiment 1: $\tau_{x0} = 0.05$ N/m^2, $\Delta\tau = 0.05$ N/m^2 at: a) 0.5 days, b) 2 days, c) 4 days and d) 6 days. OWFs create a dipole pattern with downwelling and increased temperature on the northern side and upwelling and decreased temperature on the southern side of the farm.

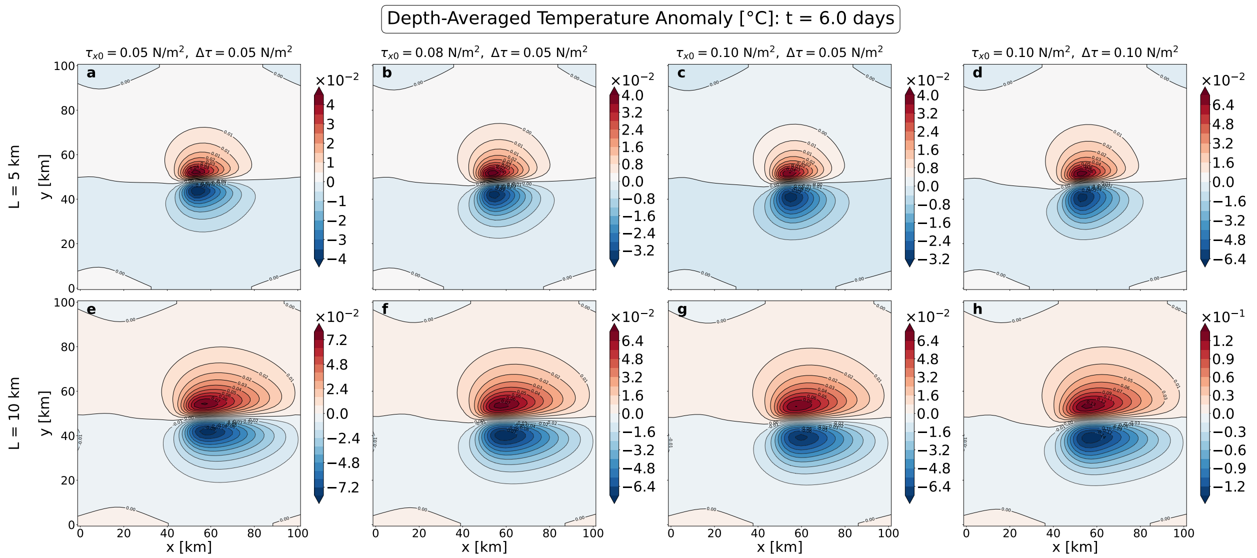

Figure 4.17: Depth-averaged temperature anomaly at day 6 for experiments 1-8 for various $\tau_{x0} = (0.05, 0.08, 0.10)$ N/m^2 and $\Delta\tau = (0.05, 0.10)$ N/m^2 as described above each panel. Panels a) to d) experiments 1-4 ($L = 5$ km), panels e) to h) experiments 5-8 ($L = 10$ km). OWFs create a dipole with downwelling on the northern side and upwelling of cold water on the southern side of the farm.

Overlapping Wind Farms

Fig. 4.18 shows the depth-averaged temperature anomaly for experiments 9 and 10. Both the magnitude of disturbance and affected area is larger for three overlapping farms than for two overlapping farms. Comparing the day 6 results with the results of the single-farm layout experiments with $\tau_{x0} = 0.10$ N/m^2, $\Delta\tau = 0.05$ N/m^2, the overlapping wind farms show increased magnitude of disturbance and larger affected area. As expected, due to temperature being redistributed by changes in vertical velocity, this is in alignment with the results of depth-averaged vertical velocity anomalies discussed in section 4.1. At day 6, the magnitude of the positive and negative anomalies are approximately the same.

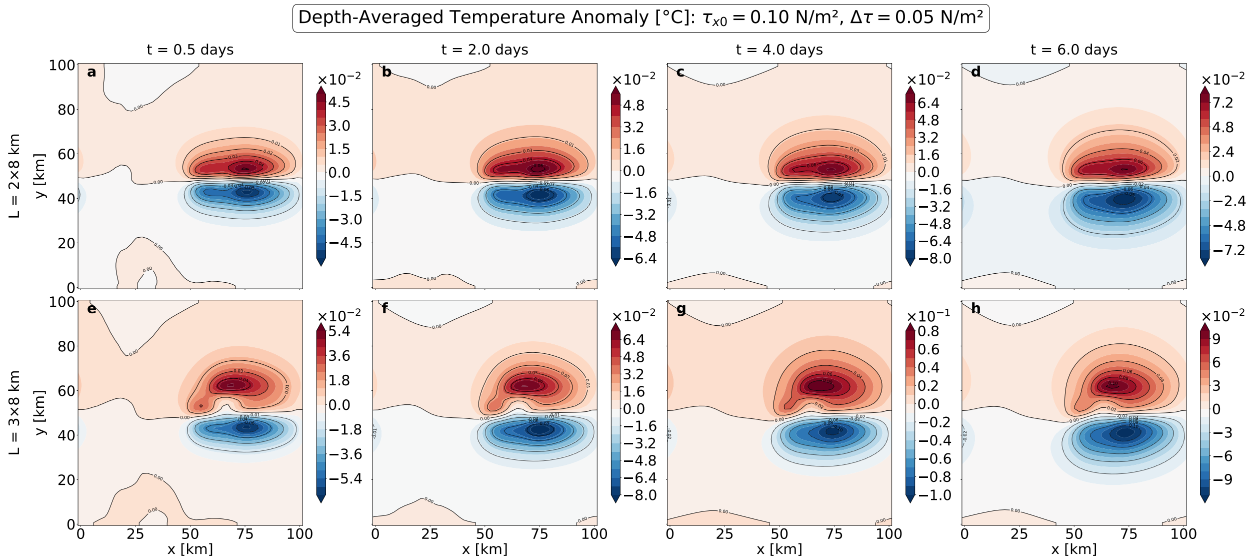

Figure 4.18: Temporal evolution of depth-averaged temperature anomaly at day 0.5, 2, 4 and 6 for experiments 9-10 ($\tau_{x0} = 0.10$ N/m^2 and $\Delta\tau = 0.05$ N/m^2). Panels a) to d) show the results for two overlapping farms with $L = 8$ km and panels e) to h) show the result for three overlapping farms with $L = 8$ km. OWFs create a dipole with downwelling and increased temperature on the northern side, and upwelling and decreased temperature on the southern side of the farm.

For temperature disturbance across the water column, both the magnitude of the wind stress reduction and the size of the wind farm seem to be decisive factors. Based on the results of the distribution and magnitude of the depth-averaged vertical velocity, this result is as expected.

Integral Over Active Zone

The first integral in Table 4.2 gives information on the net disturbance of the depth-averaged temperature anomaly across the entire horizontal domain. The second integral gives information on the net disturbance on the temperature across the entire water column at $x \approx 55$ km. Here, positive values indicate a net cooling effect. For both $L = 5$ km and $L = 10$ km, the value of the integral increases as the wind stress parameters increase. The most rapid increase is seen for experiments with the combination of strong wind stress and strong wind stress reduction ($\tau_{xo} = \Delta\tau = 0.10$ N/m^2).

This is in alignment with the horizontal integrals of depth-averaged vertical velocity in section 4.1, and an indirect consequence of the Ekman theory from section 2.2.3. All values are positive, which means that all experiments result in a net cooling effect. Theory in section 2.2 described that the temperature in the ocean typically decreases down the water column and that upwelling transports cooler water from the deep ocean towards the surface (Marshall & Plumb, 2008; Talley et al., 2011a). Based on this, a net cooling effect indicates a net upwelling effect. This is also in alignment with the results of the integrals for vertical velocity in section 4.1. Not shown here, but a vertical cross-section of the temperature shows that the dipole temperature cells are located at the thermocline, at approximately 30-40 m depth. As pointed out earlier, note that the selected cross-section may not be representative for the entire farm.

4.2.2 Thermocline

As discussed in section 2.2.1 the pycnocline acts as a physical barrier by inhibiting vertical transport between the mixed layer and deep ocean (Talley et al., 2011a). As the salinity is uniformly set in all the numerical experiments in this thesis, the thermocline is used instead of the pycnocline. The thermocline for the baseline simulation was calculated to be -33.5 m. The effect of the thermocline acting as a barrier can be seen in Fig. 4.11 and Fig. 4.13, as a gap in the vertical velocity at around 30-40 meters depth. As the pycnocline is rich in nutrients and plankton organisms, and most of the primary production takes place in the upper ocean where the sun can reach (Longhurst, 2007; Sallée et al., 2021), any disturbance of the thermocline may affect the vertical transport and thereby the access to nutrients and ultimately the primary production. In addition, disturbances of the vertical transport can also affect the distribution of the thermocline. This will be discussed in this chapter.

Single Wind Farm Layout

Fig. 4.19 shows the thermocline depth anomaly for experiments 1-8 at day 6. The results show little variation between the experiments 1-3 and 5-7 with $\tau_{x0} = (0.05, 0.08, 0.10)$ N/m^2 and $\Delta\tau = 0.05$ N/m^2. The results show the same dipole pattern as before, indicating that the wind farms do affect the thermocline depth. For experiments 4 and 8 with strong wind stress and strong wind stress reduction ($\tau_{x0} = \Delta\tau = 0.10$ N/m^2), the disturbance is increasing. This is in alignment with the vertical velocity anomalies in section 4.1 and with the depth-averaged temperature anomalies discussed above, and it is an indirect consequence of the Ekman theory from section 2.2.3. The magnitude is approximately the same for both positive and negative anomalies. The results indicate that the thermocline disturbance gets bigger with increased farm size and with increased wind stress reduction. These results align with the reduced-gravity theory presented by Broström (2008) discussed in section 2.3.

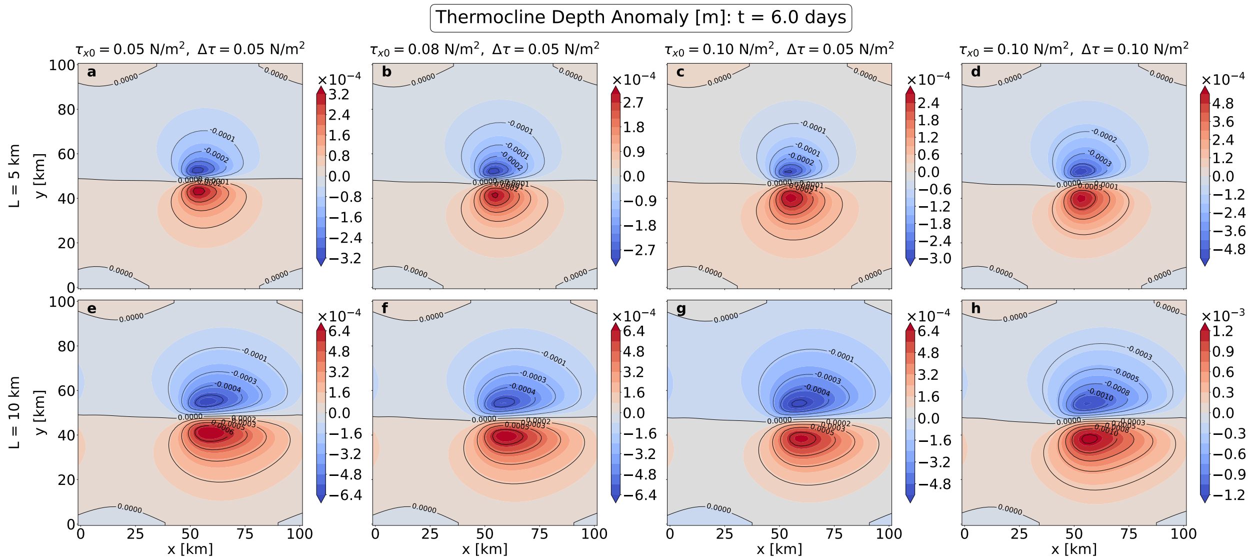

Figure 4.19: Thermocline depth anomaly at day 6 for experiments 1-8 for various $\tau_{x0} = (0.05, 0.08, 0.10)$ N/m^2 and $\Delta\tau = (0.05, 0.10)$ N/m^2 as described above each panel. Panels a) to d) experiments 1-4 ($L = 5$ km), panels e) to h) experiments 5-8 ($L = 10$ km). OWFs create a dipole with downwelling and a lowering of the thermocline on the northern side, and upwelling and a rise of the thermocline on the southern side of the farm.

Overlapping Wind Farms

Fig. 4.20 shows the temporal evolution of the thermocline depth anomaly for experiments 9 and 10 with $\tau_{x0} = 0.10$ N/m^2 and $\Delta\tau = 0.05$ N/m^2. The disturbance of the thermocline seems to grow stronger with time. Similarly to the single-farm layout, the disturbance is stronger for three overlapping farms than for two overlapping farms. Compared to the single-farm layout with the same wind stress parameters, the overlapping-farm scenarios show increased disturbances of the thermocline.

To summarize, the presence of OWFs does affect the thermocline depth. The thermocline depth is pushed downwards in the downwelling zone in the northern part of the farm and the thermocline depth is pushed upwards in the upwelling zone in the southern part of the farm. The magnitude of the disturbance of the thermocline depth increases with both increased farm size and also with strong wind stress reduction. These results align with the reduced-gravity theory presented by Broström (2008) discussed in section 2.3.

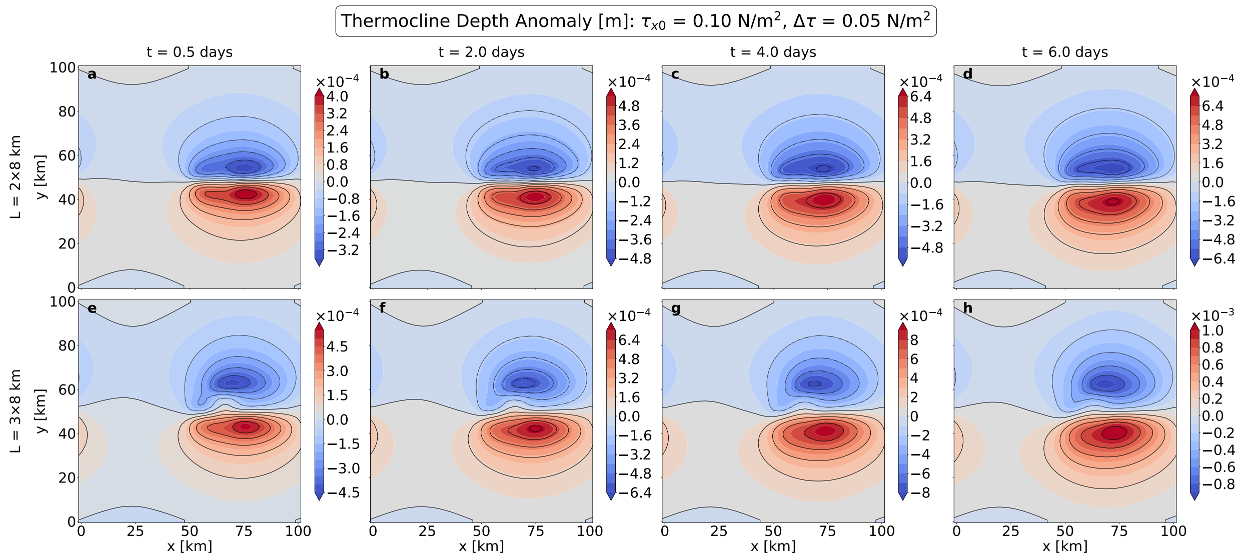

Figure 4.20: Temporal evolution of thermocline depth anomaly at day 0.5, 2, 4 and 6 for experiments 9-10 ($\tau_{x0} = 0.10$ N/m^2 and $\Delta\tau = 0.05$ N/m^2). Panels a) to d) show the results for two overlapping farms with $L = 8$ km and panels e) to h) show the result for three overlapping farms with $L = 8$ km. OWFs create a dipole with downwelling and a lowering of the thermocline on the northern side, and upwelling and a rise of the thermocline on the southern side of the farm.

Integral Over Active Zone

The third integral in Table 4.2 gives information about the net horizontal disturbance of the thermocline. For experiments 1-8, positive values indicate a rise of the thermocline and negative values indicate that the thermocline is pushed further down the water column. Here, the results differ between the experiments with $L = 5$ km and the experiments with $L = 10$ km. For $L = 5$ km, the result is a net rise of the thermocline. For $L = 10$ km there is a net rise of the thermocline for $\tau_{x0} = \Delta\tau = 0.05$ N/m^2 but for all other wind stress parameters, there is a net lowering of the thermocline. The strongest disturbance is seen for experiments 4 and 8, with both strong wind stress and wind stress reduction ($\tau_{x0} = \Delta\tau = 0.10$ N/m^2). For overlapping farms (experiments 9-10) there is a net lowering of the thermocline.

Liu et al. (2023) have studied the spatiotemporal variations of thermocline induced by wind wakes from OWFs. The findings suggest that the thermocline disturbance depends on factors such as stratification, initial thermocline depth, and the magnitude of both wind stress and wind stress reduction. The results show non-linear spatiotemporal variations that do not follow theoretical estimates. This non-linearity is explained by Liu et al. (2023) as being a result of two opposing mechanisms; the Ekman transport-induced horizontal imbalance causes a net rise in the thermocline. However, the increased upwelling also disturbs the stratification in a way that suppresses the rising of the thermocline. All simulations presented by Liu et al. (2023) show a net rise in thermocline depth (indicating net upwelling) the first 15 days. Thereafter, a reverse to a net lowering of the thermocline (indicating net downwelling) is seen at different rates and magnitudes depending on the mentioned factors. It can be seen that the shift from net rise to net lowering occurs at an earlier time for cases of strong wind stress reduction. Strong wind stress reduction also happens to be the condition that causes the strongest disturbance of thermocline depth. In addition, long wakes show a slight increased thermocline disturbance and a slight earlier shift, while wide wakes weaken the disturbance and the shift does not occur within the duration of the simulation set by Liu et al. (2023). Based on this, it seems that the magnitude of disturbance is an important factor for when in time the shift occurs. In addition, long wakes show a slight increased thermocline disturbance, while wide wakes weaken the disturbance.

Although the numerical setup in this thesis is different from those presented by Liu et al. (2023), the complex non-linear variations are explained by general ocean dynamics, and might thus be applied here to help explain the findings of this thesis as well. The integral values are the average at day 5-6. The negative values seen in the integrals for experiments 6-10 can, based on the findings of Liu et al. (2023), indicate that the magnitude of disturbance is stronger for overlapping farms and single farms with $L = 10$ km, than for $L = 5$ km, and that the magnitude increases further when the wind stress and wind stress reduction increase. The magnitude of disturbance is weaker for $L = 5$, which is why the shift has not yet occurred. These suggestions align with the results presented in Figs. 4.19 and 4.20.

Thus, the results from the integral suggest that, in addition to the factors presented by Liu et al. (2023), the size of the wind farm affects the rate at which the net thermocline depth changes from positive to negative. Seen in relation with the temperature integrals, the results suggest that the pretense of OWFs creates an initial net upwelling effect, but that the disturbance on the thermocline is complex. The vertical cross-section of temperature at $x \approx 55$ km (not depicted in this thesis) shows that the largest disturbance in temperature happens between approximately 20-60 m depth. To understand and study this further, it could therefore be interesting to include the horizontal distribution of temperature around the thermocline depth in addition to the horizontal depth-averaged temperature that has been studied in this thesis. It is also important to note that other results could potentially be obtained with a differently defined active zone.

4.2.3 Sound Speed

As discussed in section 2.5, many marine animals depend on sound to communicate, locate food and mating partners, to avoid predators, and for navigation (Forland et al., 2025). Jensen et al. (2011) describes that the propagation paths of sound are dependent on the sound speed profile, and that sound speed increases with increasing temperature. Further, the Snells' law (Eq. (2.41)) describes the local effect of sound bending towards areas with lower sound speed (Jensen et al., 2011).

As presented in section 1.4, numerical studies by Broström (2008), Paskyabi & Fer (2012), Segtnan & Christakos (2015) and Raghukumar et al. (2023) all agree that the presence of wind farm creates zones of upwelling and downwelling of varying degree, and that factors such as wind stress curl, wave forcing and farm layout affect the magnitude of said vertical disturbance. Similar results have been obtained in my study. This raises the interesting question of whether the farm-induced upwelling and downwelling also affect sound speed and ocean sound propagation. In this chapter, sound speed anomalies close to the surface ($z = -2.6$ m) will be presented and discussed.

Single Wind Farm Layout

Fig. 4.21 shows the temporal evolution of the sound speed anomaly at 2.6 m depth for experiment 1 at day $0.5, 2, 4$, and 6. As expected based on the theory of Jensen et al. (2011), the results indicate a reduction of sound speed in the upwelling zone south of the farm, and an increase in sound speed in the downwelling zone north of the farm. The sound speed has the same order of magnitude for all four days, but the distribution of the affected area changes. At day 6 the area with decreased sound speed has grown larger than the area with increased sound speed.

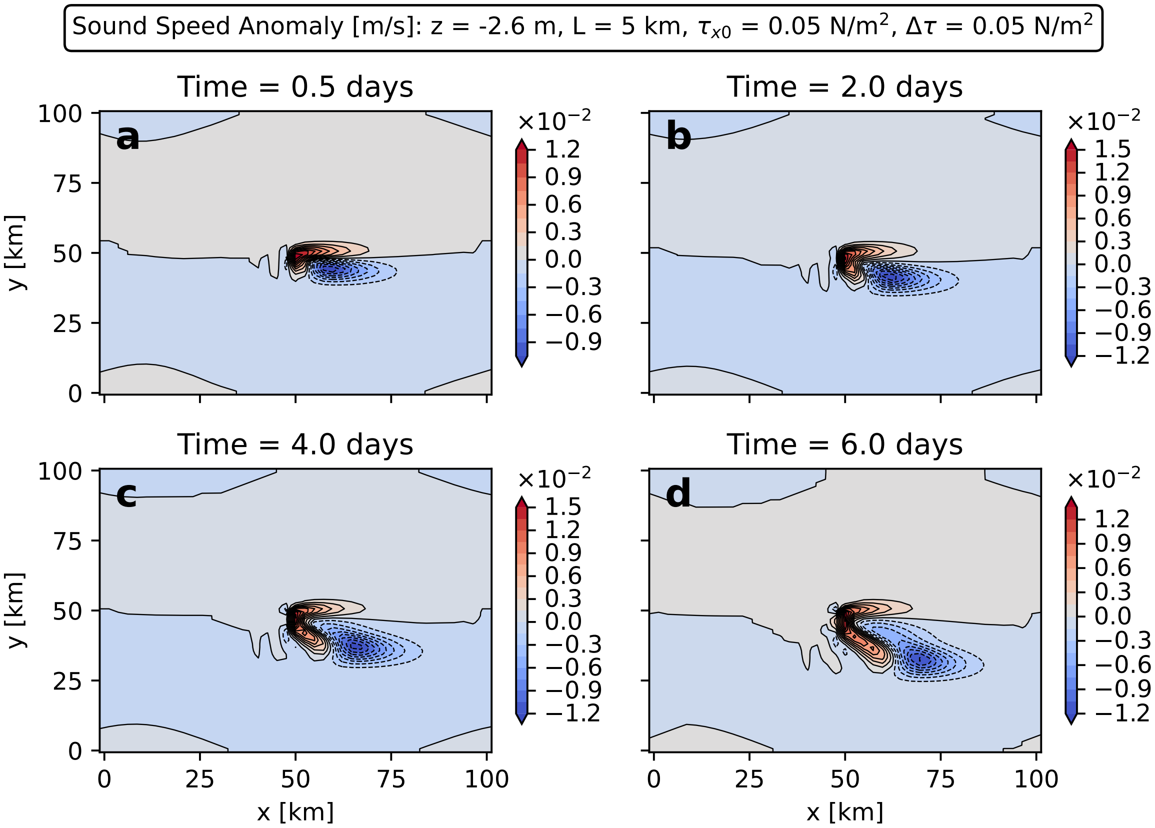

Figure 4.21: Temporal evolution of sound speed anomaly at $z = -2.6$ m for experiment 1: $\tau_{x0} = 0.05$ N/m^2, $\Delta\tau = 0.05$ N/m^2 at: a) 0.5 days, b) 2 days, c) 4 days and d) 6 days. OWFs create a dipole pattern with downwelling and increased sound speed the northern side, and upwelling and decreased sound speed on the southern side of the farm.

Fig. 4.22 shows the sound speed anomaly at 2.6 m depth at day 6 for experiments 1-8. The results do not indicate that there is a linear relation between the magnitude of disturbance and the strength of the wind stress or wind stress reduction. However, the affected area seems to grow larger with stronger wind stress. In addition, there seems to be a connection between the size of the wind farm and both the magnitude of disturbance and the distribution of the affected area.

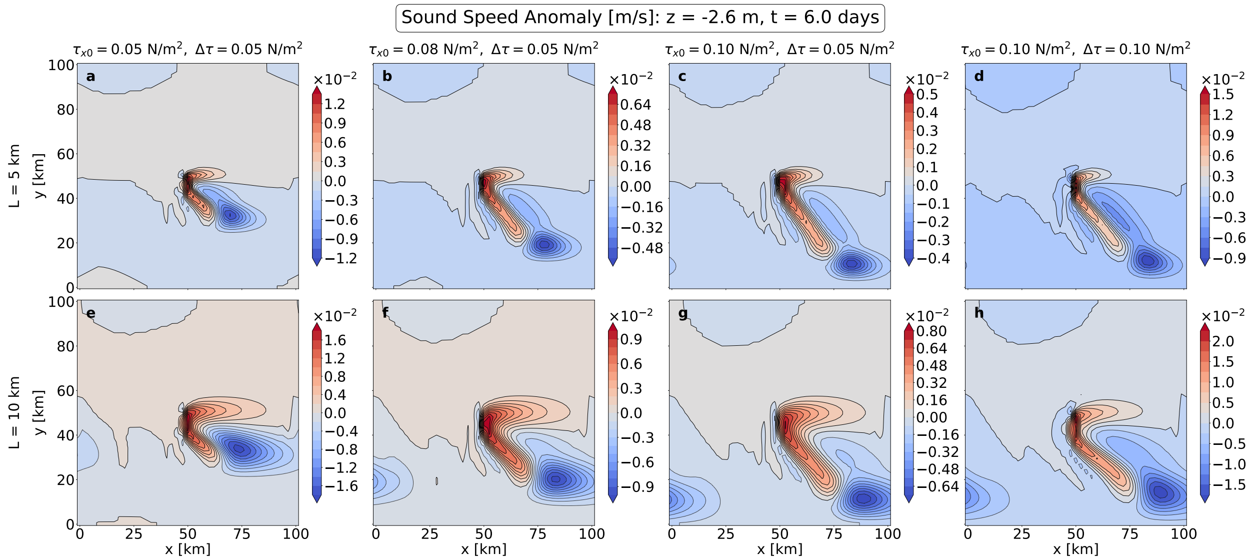

Figure 4.22: Sound speed anomaly at $z = -2.6$ m at day 6 for experiments 1-8 for various $\tau_{x0} = (0.05, 0.08, 0.10)$ N/m^2 and $\Delta\tau = (0.05, 0.10)$ N/m^2 as described above each panel. Panels a) to d) experiments 1-4 ($L = 5$ km), panels e) to h) experiments 5-8 ($L = 10$ km). OWFs create a dipole with downwelling and increased sound speed on the northern side, and upwelling and decreased sound speed on the southern side of the farm.

Overlapping Wind Farms

Fig. 4.23 shows the temporal evolution of sound speed anomaly at 2.6 m depth for experiments 9 and 10. Similar to experiment 1, the distribution of the affected area changes with time. At day 6, the magnitude of disturbance is slightly stronger for three overlapping farms than for two overlapping farms. In addition, the affected area is larger for three overlapping farms. There is little variation in the magnitude of disturbance of sound speed for overlapping farms compared to single-farm layout with $L = 10$ km. However, the affected area is larger for the experiments with overlapping farms.

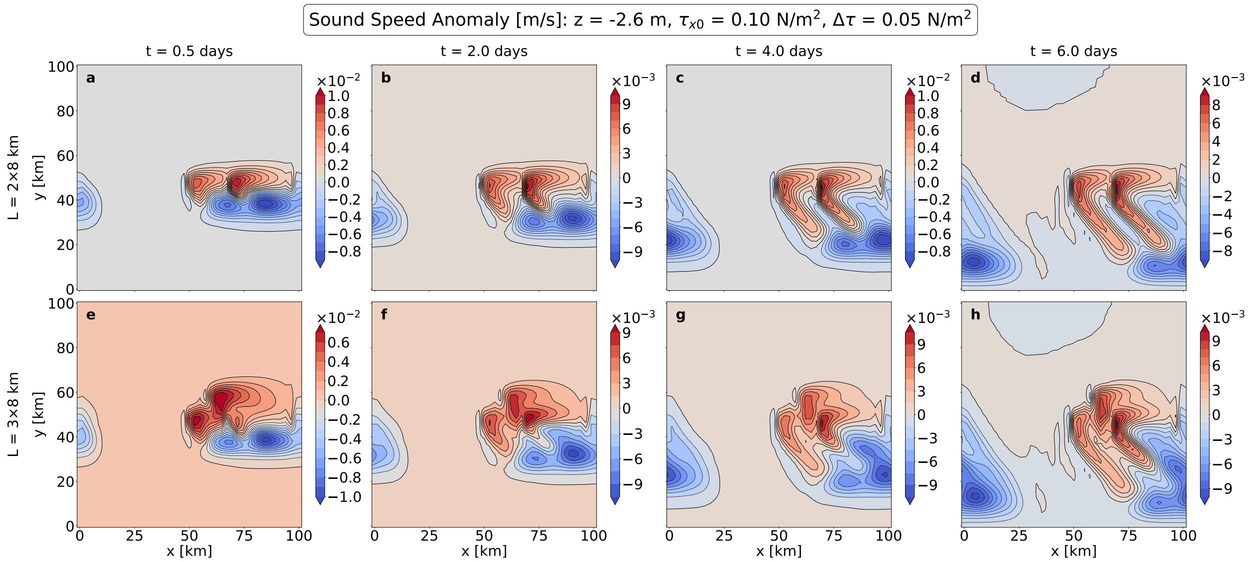

Figure 4.23: Temporal evolution of sound speed anomaly at $z = -2.6$ m at day 0.5, 2, 4 and 6 for experiments 9-10 ($\tau_{x0} = 0.10$ N/m^2 and $\Delta\tau = 0.05$ N/m^2). Panels a) to d) show the results for two overlapping farms with $L = 8$ km and panels e) to h) show the result for three overlapping farms with $L = 8$ km. OWFs create a dipole with downwelling and increased sound speed on the northern side, and upwelling and decreased sound speed on the southern side of the farm.

Integral Over Active Zone

The last integral in Table 4.2 gives information on the net horizontal disturbance of the sound speed at 2.6 m depth. Positive values indicate a reduction in sound speed. Thus, the results of all experiments show a net reduction of the sound speed close to the surface. For the single-farm experiments, the biggest reduction of sound speed close to the surface is seen for the experiments with a combination of strong wind stress and wind stress reduction ($\tau_{xo} = \Delta\tau = 0.10$ N/m^2). From section 2.5.1 it was stated that sound speed increases with increased temperature, salinity and pressure (Jensen et al., 2011). In the upper layers of the ocean, sound speed is mainly determined by temperature and salinity, whereas pressure becomes the determining factor in the deeper ocean (Mackenzie & Byrne, 2025; Jensen et al., 2011). Thus, a net reduction of sound speed indicates decreased temperature, which aligns with the net cooling effect shown by the temperature integrals and the net upwelling shown by the vertical velocity and surface elevation integrals. The impact and importance of the wind stress reduction is also in alignment with the results of the horizontal integral of the depth-averaged vertical velocity in section 4.1, and an indirect consequence of the Ekman theory from section 2.2.3.

Based on the results presented, there is no doubt that the presence of OWFs affects the sound speed in the upper ocean, and that both the size and layout of the wind farm, as well as the magnitude of wind stress and wind stress reduction, are important factors. The remaining question is whether the disturbance is significant enough to cause damage to ocean animals. Researchers have estimated that the ocean sound speed will increase with more than 1.5%, or 20 m/s by the end of the century due to climate change and global warming following a ”business-as-usual” scenario, and that this can impact the ability of marine animals to locate food, predictors, mating partners etc. (Affatati et al., 2022). According to Mackenzie & Byrne (2025), ocean sound speed increases by 4.5 m/s per 1°C increase in temperature. Compared to these numbers, the results presented in this thesis are very small. However, it is important to note that the idealized nature of my setup is a limiting factor and that future studies should consider including a more realistic setup to capture cite-specific extents of disturbances, e.g. at Hywind Tampen. This would provide valuable knowledge that can be implemented in future development of offshore wind technology.

4.3 Biogeochemistry

4.3.1 Biological Tracers

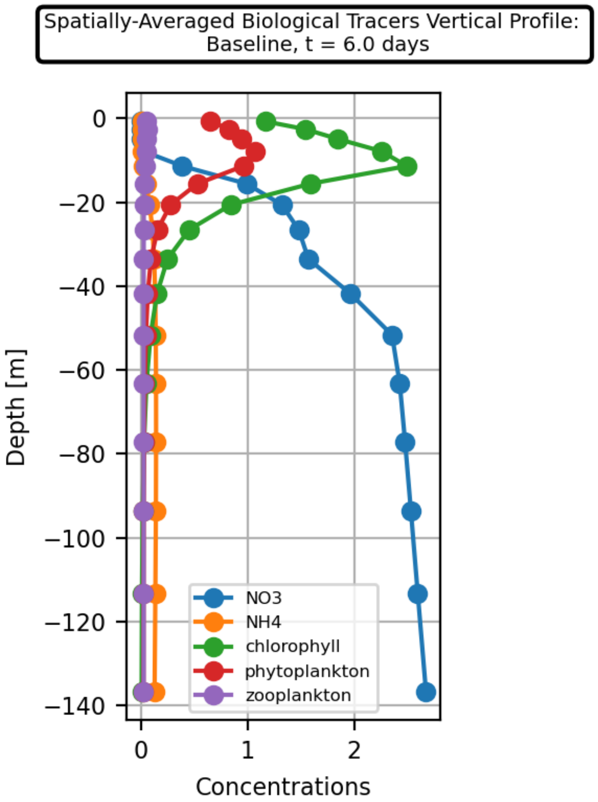

Figure 4.24: Vertical profile of spatially-averaged biological tracers NO_3 (—), NH_4 (—), chlorophyll (—), phytoplankton (—) and zooplankton (—) at day 6 for the baseline simulations. The concentration of chlorophyll and phytoplankton is highest close to the surface and decreases further down. The concentration of NO_3 and NH_4 is lowest close to the surface and increases with depth. The concentration of zooplankton is approximately zero for all depths.

Fig. 4.24 shows the vertical profile of the spatially-averaged biological tracers for the baseline simulations, i.e. without the wind farm at day 6. The concentration of nutrients NO_3 and NH_4 is highest towards the sea floor and decreases upward, whereas the concentration of chlorophyll, phytoplankton and zooplankton is higher closer to the surface. As discussed in section 2.2.4 and section 2.2.1, these patterns are due to the high consumption of nutrients in the upper ocean where most of the primary production usually occurs (Talley et al., 2011a; Longhurst, 2007; Sallée et al., 2021).

Single Wind Farm Layout

Fig. 4.25 shows the vertical profile anomalies of the spatially-averaged biological tracers NO_3, NH_4, chlorophyll, phytoplankton and zooplankton at day 6 for experiments 1-8. For all experiments, chlorophyll shows a large negative spike at around 10 m depth and some positive spikes at both 0 m and approximately 20 m depth. The phytoplankton anomaly follows the same pattern as the chlorophyll anomaly, only weaker. Negative chlorophyll and phytoplankton anomalies indicate a reduction in primary production and vice versa. As expected based on the theory already presented, the NO_3 anomaly follows a pattern somewhat opposite to chlorophyll and phytoplankton, with positive pikes at approximately 10 m and 40 m depth and negative pikes at approximately 20 m and 50 m depth. Similarly, NH_4 shows a small positive spike at approximately 10 m depth and a small negative spike at approximately 20 m depth. Zooplankton anomaly is close to zero throughout the entire water column. The results indicate that the largest anomalies are caused by experiments 4 and 8 with a combination of strong wind stress and wind stress reduction ($\tau_{x0} = \Delta\tau = 0.10$ N/m^2). For each wind stress combination, wind farms with $L = 10$ km also seem to generate larger anomalies than wind farms with $L = 5$ km.

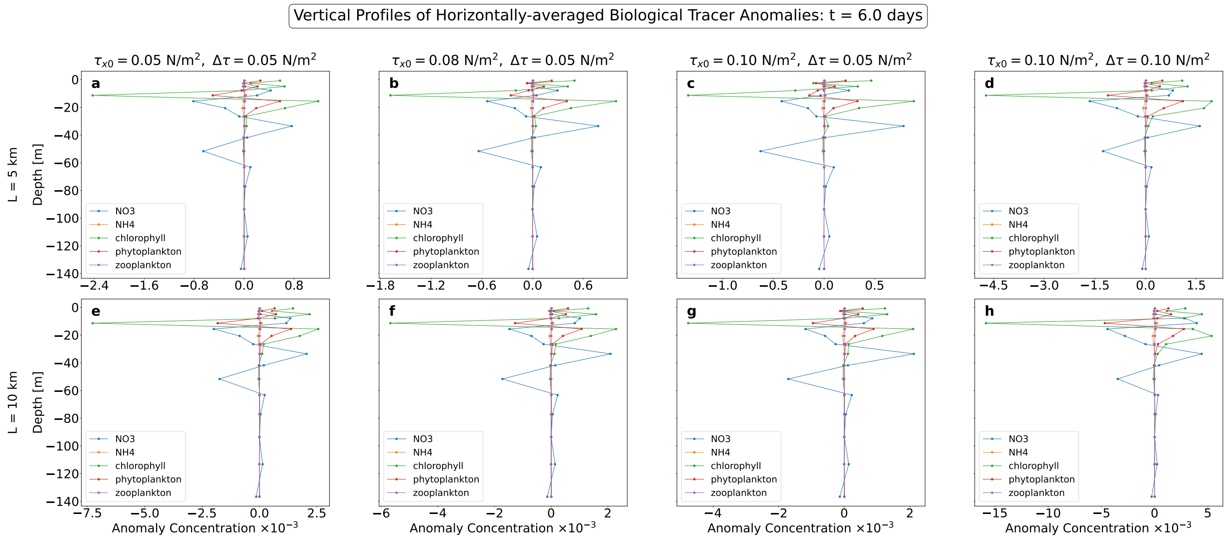

Figure 4.25: Vertical profile of horizontally-averaged biological tracer anomalies NO_3 (━), NH_4 (━), chlorophyll (━), phytoplankton (━) and zooplankton (━) at day 6 for experiments 1-8 for various $\tau_{x0} = (0.05, 0.08, 0.10)$ N/m^2 and $\Delta\tau = (0.05, 0.10)$ N/m^2 as described above each panel. Panels a) to d) experiments 1-4 ($L = 5$ km), panels e) to h) experiments 5-8 ($L = 10$ km).

Fig. 4.26 shows the cross-section of the biological tracer anomalies for experiments 1-4 with $L = 5$ km at day 6 for $x \approx 55$ km. In the downwelling cell, the concentration of both NO_3 and NH_4 decreases in the upper ocean due to nutrient-poor water being pushed down from above. Oppositely, nutrient-rich water is being pushed up from below, increasing the concentration of NO_3 and NH_4 in the upwelling zone close to the surface. This seems to happen mainly above the thermocline, but there is also a pair of weaker cells visible below the thermocline.

As expected based on Fig. 4.25, the opposite pattern is seen for chlorophyll; in the downwelling zone, chlorophyll-rich surface water is pushed downward into the already chlorophyll-rich area in Fig. 4.24, creating a cell with decreased concentration at the surface and a cell with increased concentration directly below. In the upwelling zone, the chlorophyll-rich water in the mixed layer is pumped towards the surface creating a positive cell, while chlorophyll-poor water from the depths creates a negative cell directly below. The same is true for phytoplankton and zooplankton as well.

The results indicate that both the magnitude of wind stress and wind stress reduction affect the results. However, the relation is not very clear.

Fig. 4.27 shows the same pattern as Fig. 4.26, in terms of both the distribution of positive and negative cells, and the magnitude of disturbance according to the wind stress parameters. The difference is the magnitude of the anomalies. Generally, it seems that wind farms with size $L = 10$ km generate greater disturbances than farms with size $L = 5$ km.

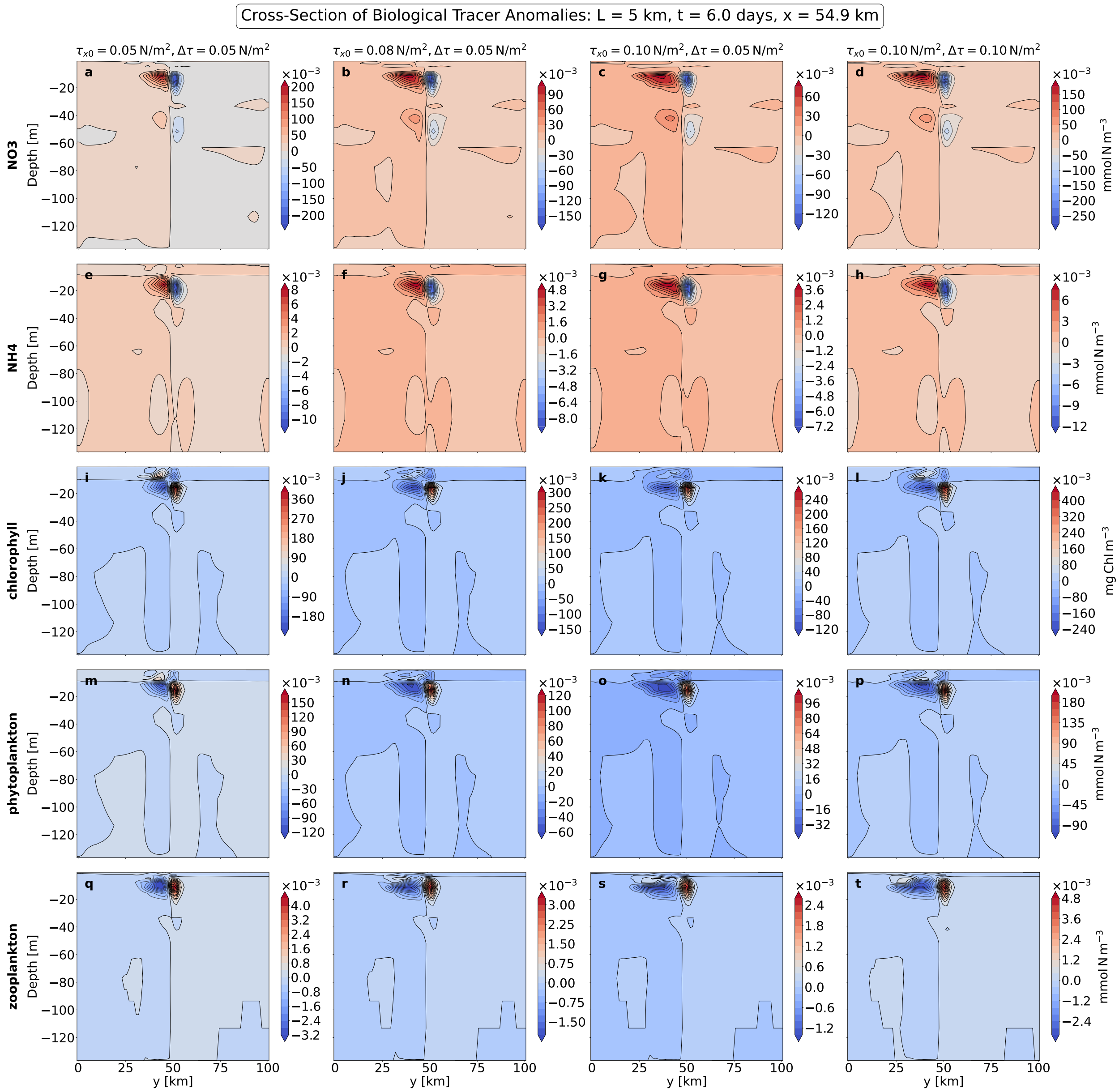

Figure 4.26: Cross-section of biological tracer anomalies at $x \approx 55$ km at day 6 for experiments 1-4 ($L = 5$ km) for various $\tau_{x0} = (0.05, 0.08, 0.10)$ N/m^2 and $\Delta\tau = (0.05, 0.10)$ N/m^2 as described above each panel. Panels a) to d) NO_3 anomalies for experiments 1-4, panels e) to h) NH_4 anomalies for experiments 1-4, panels i) to l) chlorophyll anomalies for experiments 1-4, panels m) to p) phytoplankton anomalies for experiments 1-4, panels q) to t) zooplankton anomalies for experiments 1-4.

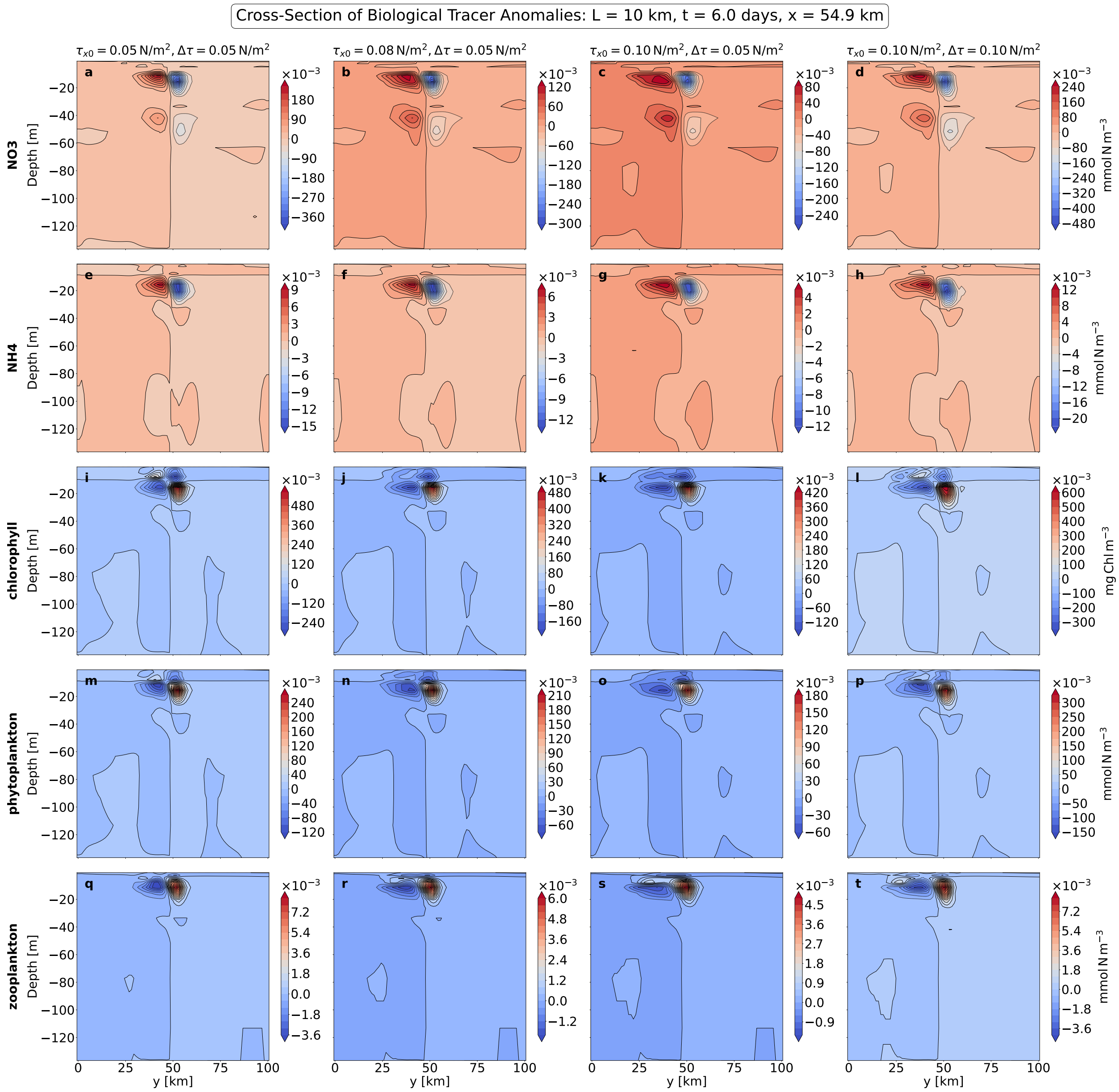

Figure 4.27: Cross-section of biological tracer anomalies at $x \approx 55$ km at day 6 for experiments 5-8 ($L = 10$ km) for various $\tau_{x0} = (0.05, 0.08, 0.10)$ N/m^2 and $\Delta\tau = (0.05, 0.10)$ N/m^2 as described above each panel. Panels a) to d) NO$_3$ anomalies for experiments 5-8, panels e) to h) NH$_4$ anomalies for experiments 5-8, panels i) to l) chlorophyll anomalies for experiments 5-8, panels m) to p) phytoplankton anomalies for experiments 5-8, panels q) to t) zooplankton anomalies for experiments 5-8.

Overlapping Wind Farms

Fig. 4.28 shows the temporal evolution of spatially-averaged vertical profiles of the anomalies of biological tracers NO_3, NH_4, chlorophyll, phytoplankton and zooplankton for overlapping farms with $\tau_{x0} = 0.10$ N/m^2 and $\Delta\tau = 0.05$ N/m^2. The disturbance of the tracer concentrations increases with time. At day 6, the anomalies follow the same vertical pattern as the single-farm experiments with the same wind stress parameters. The magnitude of the negative anomalies seem to increase with farm size. Positive anomalies show an increasing trend, but at a lower rate.

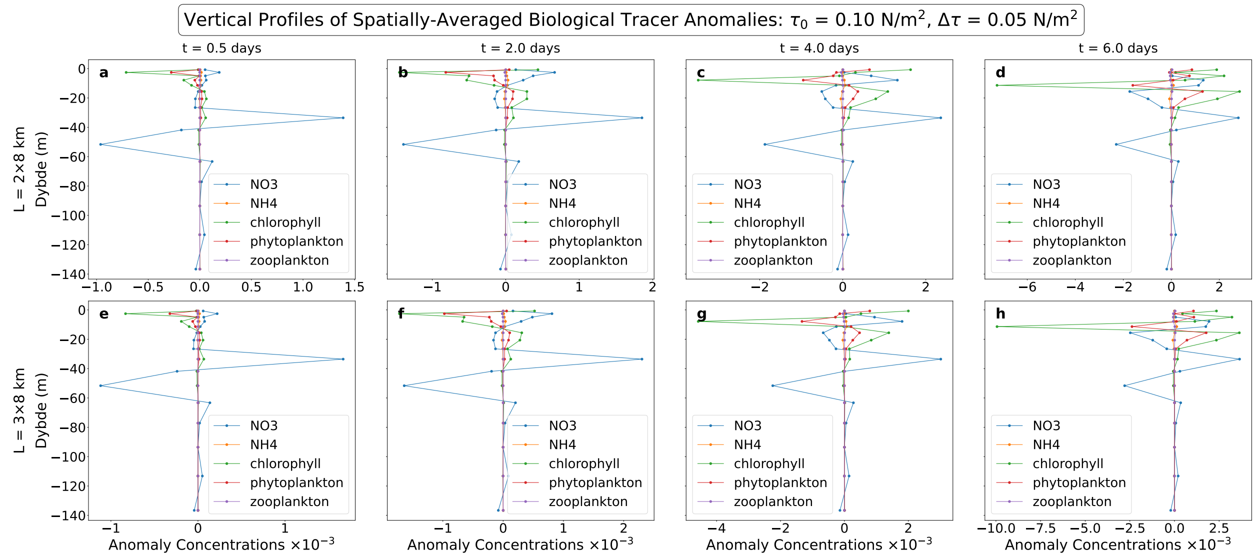

Figure 4.28: Temporal evolution of vertical profiles of spatially-averaged biological tracer anomalies NO_3 (—), NH_4 (—), chlorophyll (—), phytoplankton (—) and zooplankton (—) at day 0.5, 2, 4 and 6 for experiments 9-10 ($\tau_{x0} = 0.10$ N/m^2 and $\Delta\tau = 0.05$ N/m^2). Panels a) to d) show the results for two overlapping farms with $L = 8$ km and panels e) to h) show the result for three overlapping farms with $L = 8$ km.

Fig. 4.29 show the cross-section anomalies of biological tracers at day 6 for overlapping-farm experiments with $\tau_{x0} = 0.10$ N/m^2 and $\Delta\tau = 0.05$ N/m^2 at $x \approx 55$ km. The results follow the same pattern as the single-farm experiments. However, due to the layout of the overlapping farms as seen in Fig. 3.1, the cross-section at $x \approx 55$ km does not capture the total effect of the overlapping farms. To compare the impact of the farm layout on the anomaly disturbance, Fig. 4.30 shows the horizontal tracer anomalies at day 6 at depth 16 m for $\tau_{x0} = 0.10$ N/m^2 and $\Delta\tau = 0.05$ N/m^2 for single wind farms with $L = 5$ km and $L = 10$ km and for two and three overlapping farms with $L = 8$ km. The results indicate that both the affected area and the magnitude of disturbance increase when the farm size increases. The strongest and most extensive disturbances are observed for three overlapping farms.

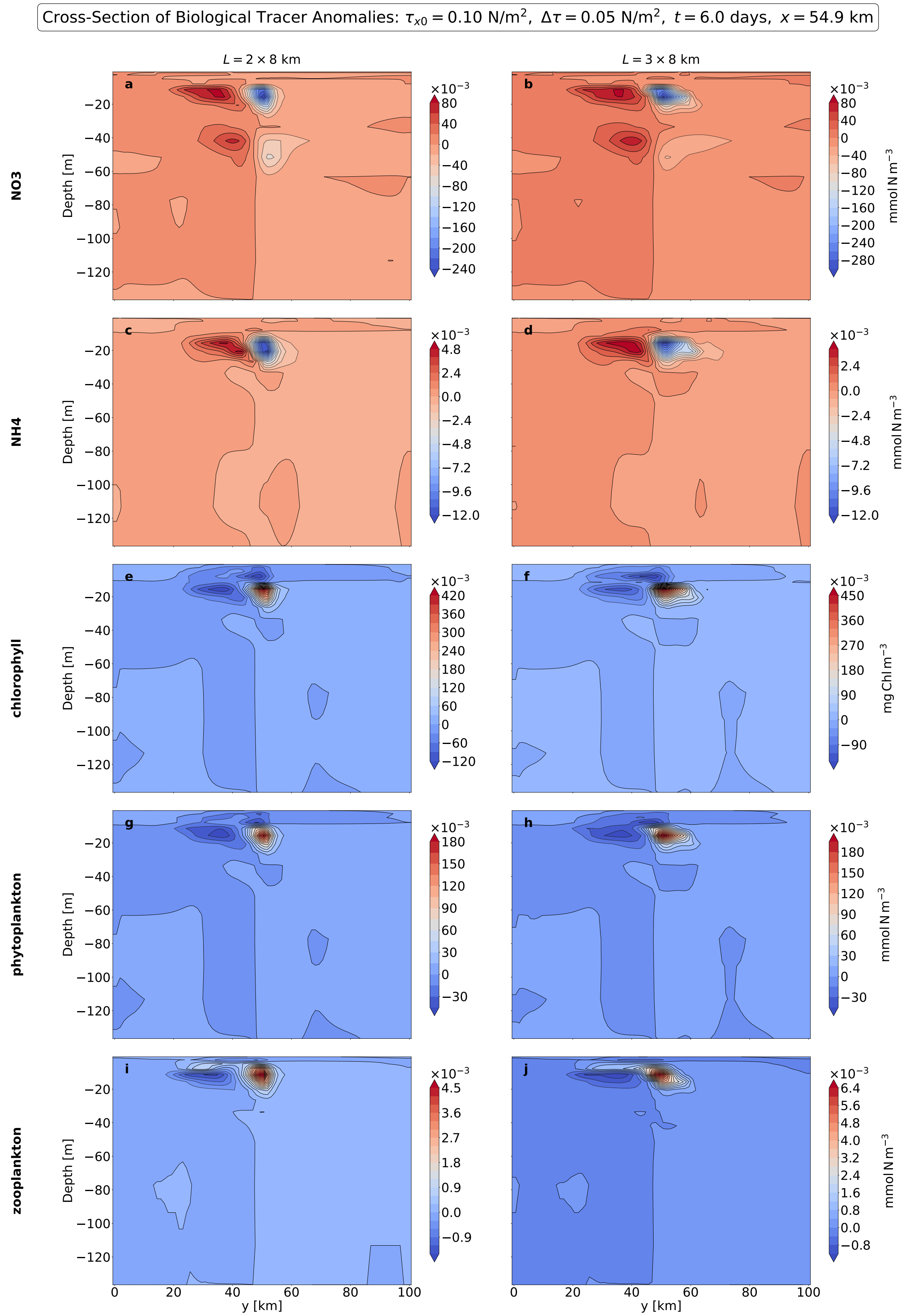

Figure 4.29: Cross-section of biological tracer anomalies at $x \approx 55$ km at day 6 for experiments 9-10 ($L = 2 \times 8$ km and $L = 3 \times 8$ km) for $\tau_{x0} = 0.10$ N/m^2 and $\Delta\tau = 0.05$ N/m^2. Panels a) to b) NO_3 anomalies, panels c) to d) NH_4 anomalies, panels e) to f) chlorophyll anomalies, panels g) to h) phytoplankton anomalies, panels i) to j) zooplankton anomalies.

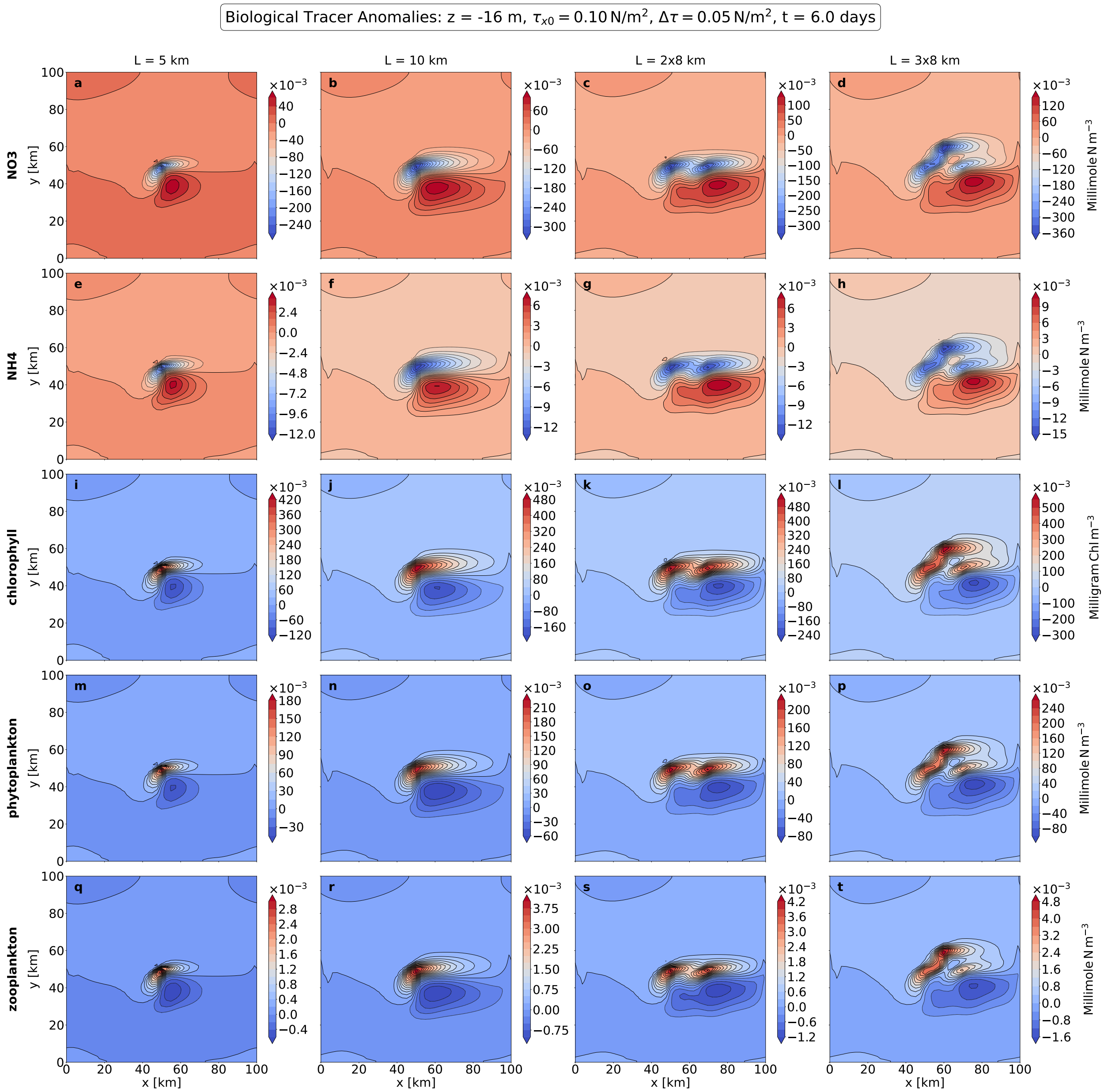

Figure 4.30: Biological tracer anomalies at $z = -16$ m for experiments $3, 7, 9$ and 10 ($\tau_{x0} = 0.10$ N/m^2 and $\Delta\tau = 0.05$ N/m^2) at day 6. Panels a) to d) NO_3 concentration anomalies, panels e) to h) NH_4 concentration anomalies, panels i) to l) chlorophyll concentration anomalies, panels m) to p) phytoplankton concentration anomalies, panels q) to t) zooplankton concentration anomalies.

Integral Over Active Zone

Table 4.3: Biogeochemical vertical integrals. The results of experiments 1-4 are normalized by experiment 1 and the results of experiments 5-8 are normalized by experiment 5. Experiments 9 and 10 are normalized by themselves. The green (—) reference values mean that positive values indicate net increased concentration and negative values indicate net decreased concentration. The red (—) reference values mean that positive values indicate net decreased concentration and negative values indicate net increased concentration.

Experiment	$\int \overline{\mathrm{NO}'_3}_{hor}\,\mathrm{d}z$	$\int \overline{\mathrm{NH}'_4}_{hor}\,\mathrm{d}z$	$\int \overline{\mathrm{Chlorophyll}'}_{hor}\,\mathrm{d}z$	$\int \overline{\mathrm{phytoplankton}'}_{hor}\,\mathrm{d}z$	$\int \overline{\mathrm{zooplankton}'}_{hor}\,\mathrm{d}z$
1	**1.00**	**1.00**	**1.00**	**1.00**	**1.00**
2	0.72	0.76	0.69	0.75	0.77
3	0.58	0.62	0.53	0.63	0.69
4	2.21	2.55	2.52	2.31	1.61
5	**1.00**	**1.00**	**1.00**	**1.00**	**1.00**
6	0.74	0.84	0.79	0.84	1.15
7	0.56	0.71	0.66	0.73	1.21
8	2.52	3.18	2.83	2.52	2.54
9	**1.00**	**1.00**	**1.00**	**1.00**	**1.00**
10	**1.00**	**1.00**	**1.00**	**1.00**	**1.00**

Table 4.4: Biogeochemical horizontal integrals. The results of experiments 1-4 are normalized by experiment 1 and the results of experiments 5-8 are normalized by experiment 5. Experiments 9 and 10 are normalized by themselves. The green (—) reference values mean that positive values indicate net increased concentration and negative values indicate net decreased concentration. The red (—) reference values mean that positive values indicate net decreased concentration and negative values indicate net increased concentration.

Experiment	$\int \overline{\mathrm{NO}'_3}_{depth}\,\mathrm{d}x\mathrm{d}y$	$\int \overline{\mathrm{NH}'_4}_{depth}\,\mathrm{d}x\mathrm{d}y$	$\int \overline{\mathrm{Chlorophyll}'}_{depth}\,\mathrm{d}x\mathrm{d}y$	$\int \overline{\mathrm{phytoplankton}'}_{depth}\,\mathrm{d}x\mathrm{d}y$	$\int \overline{\mathrm{zooplankton}'}_{depth}\,\mathrm{d}x\mathrm{d}y$
1	**1.00**	**1.00**	**1.00**	**1.00**	**1.00**
2	1.36	-6.44	-0.11	0.61	1.24
3	1.45	-11.92	-1.14	0.32	1.97
4	1.21	33.97	1.67	2.01	3.66
5	**1.00**	**1.00**	**1.00**	**1.00**	**1.00**
6	1.10	1.15	-0.20	0.71	-1.50
7	1.16	1.37	-1.49	0.41	-6.80
8	1.67	-0.71	3.52	2.39	-8.88
9	**1.00**	**1.00**	**1.00**	**1.00**	**1.00**
10	**1.00**	**1.00**	**1.00**	**1.00**	**1.00**

To further investigate the cumulative extent of the disturbance OWFs pose on the biological tracers, vertical and horizontal integrals are presented next. Table 4.3 shows the vertical integrals, which gives information on the net vertical disturbance of the horizontally-averaged tracers. For NO_3 and NH_4, positive values represent a net decrease in concentration. However, for chlorophyll and phytoplankton, positive values indicate a net increase in concentration. For zooplankton, positive values indicate a net concentration increase for experiments 1-4, and a net decrease for experiments 5-10. Based on this, the results show that there is a net reduction in NO_3 and NH_4, and a net increase in chlorophyll and phytoplankton for all experiments. For zooplankton, there is a net increase in concentration for experiments 1-4 and a net decrease in concentration for experiments 5-10. The strongest net vertical disturbance is found for the wind conditions of strong wind stress and strong wind stress reduction ($\tau_{x0} = \Delta\tau = 0.10$ N/m^2), i.e. experiments 4 and 8. For all other experiments with $\Delta\tau = 0.05$ N/m^2, the net values of all tracers except zooplankton decrease as the wind stress increases from experiments 1-3 and 5-7. This is in alignment with the results shown in Figs. 4.26 and 4.27; for NO_3 and NH_4, the magnitude of disturbance decreases as the wind stress increases, but the area increases, especially for the positive anomalies. This indicates that the net upwelling processes are spread over a larger area than the net downwelling processes. However, the magnitude of negative anomalies are about twice as big as the positive anomalies. Consequently, the net effect remains negative, but the magnitude decreases as the affected area in the upwelling zone increases with increasing wind stress. Equivalent patterns can be seen for all biological tracers; the magnitudes of positive anomalies are more than twice the magnitude of the negative anomalies for chlorophyll and phytoplankton. The affected area is, however, growing larger with increased wind stress, especially for the negative anomalies in the upwelling zone. Thus, the results of the integral remain net positive, but decrease in magnitude with increasing wind stress.

Table 4.4 shows the horizontal integrals, which gives information on the net horizontal disturbance of the depth-integrated biological tracer anomalies. For experiments 1-4, positive values indicate increased concentration of NO_3, chlorophyll, phytoplankton and zooplankton, but decreased concentration of NH_4. For experiments 5-8, positive values indicate increased concentrations for all biological tracers except zooplankton. For experiments 9-10, positive values indicate increased concentration of NO_3, NH_4, phytoplankton and zooplankton and decreased concentration of chlorophyll. For all experiments, there is a net increase in the concentration of NO_3 and phytoplankton. For zooplankton, there is a net increase in concentration for all experiments except experiment 5. For NH_4 and chlorophyll, there is more inconsistency in net concentration. For chlorophyll, phytoplankton and zooplankton, the same pattern as before is seen where the conditions of strong wind stress and strong wind stress reduction seem to cause the strongest disturbance. The same pattern is not as clear for nutrients NO_3 and NH_4.

It is apparent that OWFs have an effect on the distribution and transport of biological tracers. However, there are some inconsistencies between the results of the horizontal and vertical integrals, and it is difficult to evaluate the net impact this will have on primary production. This might be because the integrals are sensitive to the manually defined active zones, and that differently defined active zones can give different results. A more standardized method of choosing the active zones would be valuable to fully evaluate the results. To complement these uncertainties, ROMS primary production output data will be investigated next.

4.3.2 Primary Production

ROMS provides output-data on primary production. These data will be presented and discussed in this chapter.

As discussed in section 2.2.4, primary production is the backbone of the entire ocean ecosystem. Phytoplankton cannot perform primary production without access to nutrients and sunlight, and phytoplankton are very sensitive to environmental changes (NOAA, 2024a,b).

Single Wind Farm Layout

The cross-sections of the primary production anomaly at $x \approx 55$ km for experiments 1-8 are shown in Fig. 4.31. Generally, the downwelling zone creates a cell with reduced primary production above 20 m depth and a cell with increased primary production at approximately 20 m depth. In the upwelling zone, a cell with increased primary production is created above 20 m depth. This is in alignment with the results of the biological tracers; in the downwelling zone where the nutrient concentration decreases, there is also decreased primary production. Similarly, in the upwelling zone where the nutrient concentration increases, so does the primary production. This relation is further described in section 2.2.4 and section 2.2.1.

From Fig. 4.31 it can also be seen that with stronger wind stress but constant wind stress reduction $\Delta\tau = 0.5$ N/m^2, the strength of both positive and negative anomaly cells is reduced, while the affected area slightly increases. The magnitudes of the negative anomalies are stronger than the magnitudes of the positive anomalies, but the positive anomalies affect a larger area. This is in agreement with the results of the integrals that will be discussed below.

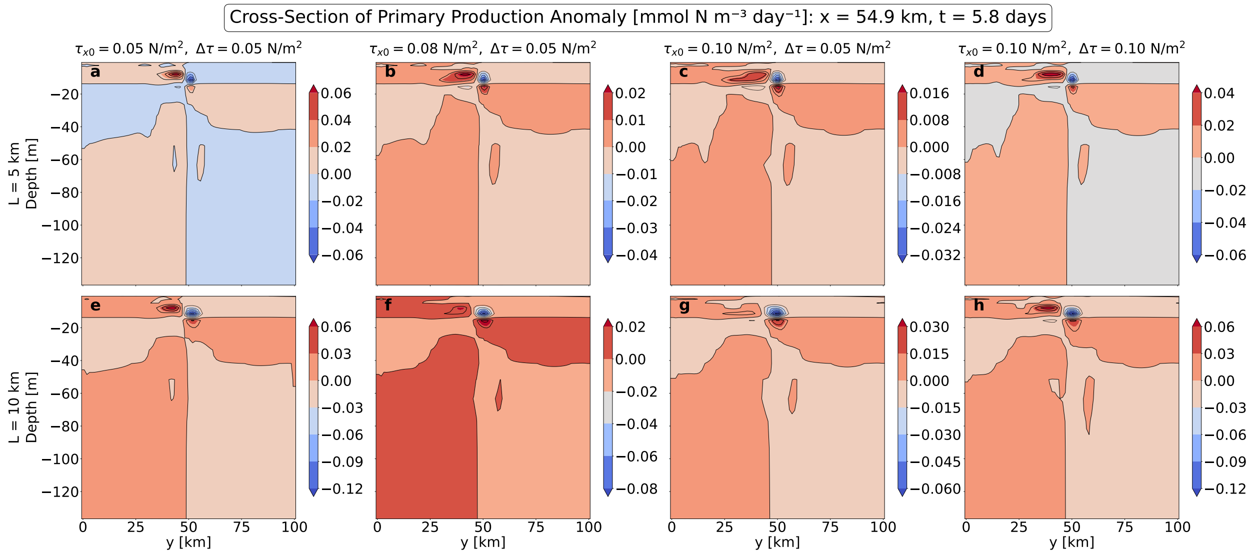

Figure 4.31: Cross-section of primary production anomaly at $x \approx 55$ km at day 5.8 for experiments 1-8 for various $\tau_{x0} = (0.05, 0.08, 0.10)$ N/m^2 and $\Delta\tau = (0.05, 0.10)$ N/m^2 as described above each panel. Panels a) to d) experiments 1-4 ($L = 5$ km), panels e) to h) experiments 5-8 ($L = 10$ km).

Fig. 4.32 shows the depth-integrated primary production anomaly for experiments 1-8 at approximately 6 days. The results indicate that the negative anomalies are stronger but affect a smaller area than the positive anomalies. It is also shown that the strongest disturbance is caused when both the wind stress and the wind stress reduction are strong. The disturbance also seems to increase when L increases.

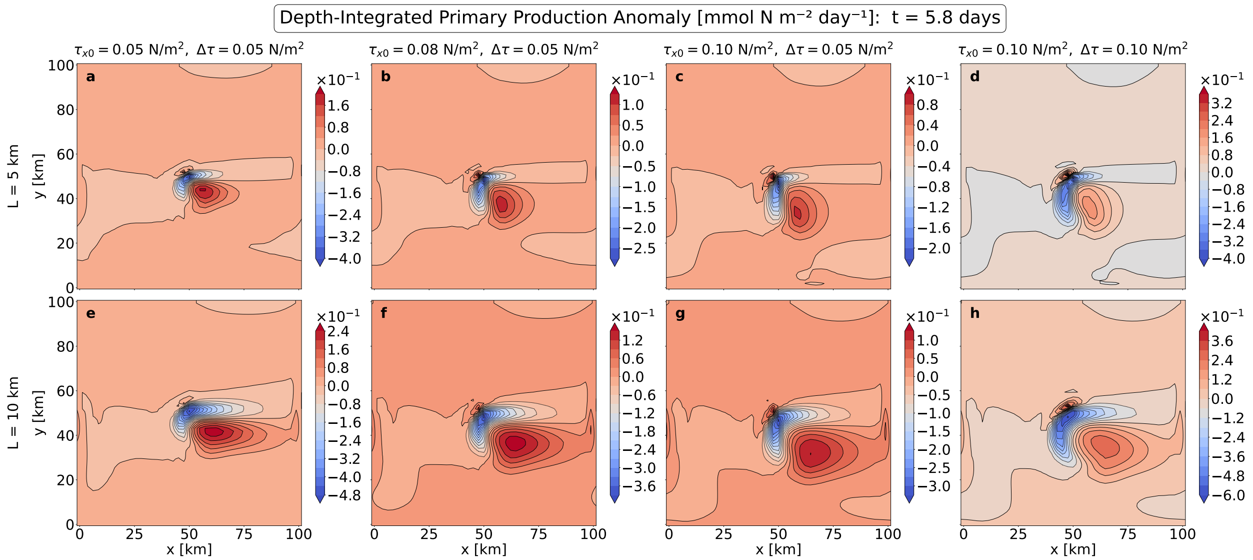

Figure 4.32: Depth-integrated primary production anomaly at day 5.8 for experiments 1-8 for various $\tau_{x0} = (0.05, 0.08, 0.10)$ N/m^2 and $\Delta\tau = (0.05, 0.10)$ N/m^2 as described above each panel. Panels a) to d) experiments 1-4 ($L = 5$ km), panels e) to h) experiments 5-8 ($L = 10$ km). OWFs create a dipole with downwelling and decreased primary production on the northern side, and upwelling and increased primary production on the southern side of the farm.

Overlapping Wind Farms

The upper panels of Fig. 4.33 show the vertical cross-section of primary production anomaly at $x \approx 55$ km for the two experiments with overlapping wind farms, and the bottom panels show the depth-integrated horizontal anomalies for the same two experiments. Compared to the single-farm experiments with the same wind stress parameters ($\tau_{x0} = 0.10$ N/m^2 and $\Delta\tau = 0.05$ N/m^2), the anomalies of the overlapping farms follow the same pattern but with stronger magnitudes. The difference in magnitude is largest for three overlapping farms. The magnitude for two overlapping farms is about the same as for one singular farm with $L = 10$ km. However, the affected area is larger for overlapping farms than for singular farms.

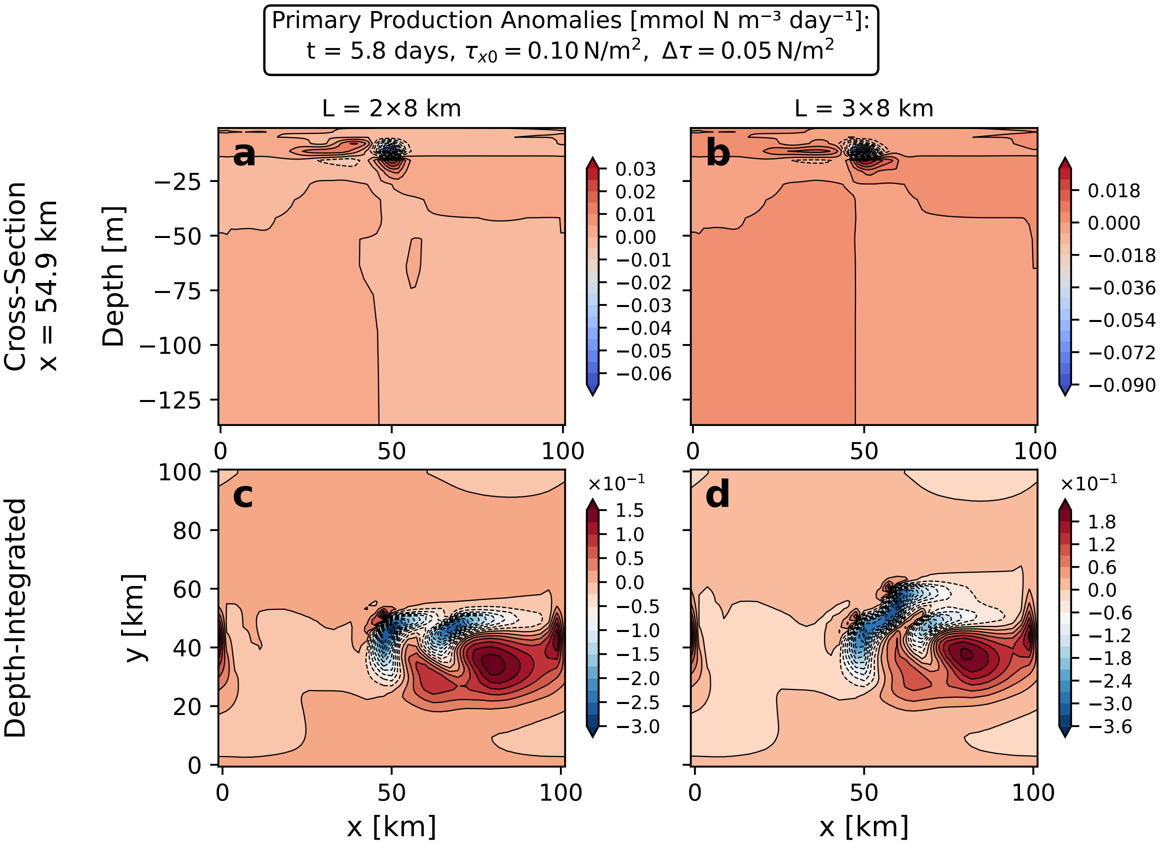

Figure 4.33: Primary production anomalies at day 5.8 for experiments 9-10 ($\tau_{x0} = 0.10$ N/m^2 and $\Delta\tau = 0.05$ N/m^2) as indicated above the panels. Panels a) to b) show the cross-section of primary production anomalies at $x \approx 55$ km, and panels c) to d) show the result of depth-integrated primary production anomalies. OWFs create a dipole with downwelling and decreased primary production on the northern side, and upwelling and increased primary production on the southern side of the farm.

Integral Over Active Zone

Table 4.5: Primary production integrals. The results of experiments 1-4 are normalized by experiment 1 and the results of experiments 5-8 are normalized by experiment 5. The green (—) reference values mean that positive values indicate net increased primary production and negative values indicate net decreased primary production. The red (—) reference value means that positive values indicate net decreased primary production and negative values indicate net increased primary production.

Experiment	$\int P'_{x=55km}\,\mathrm{d}z\,\mathrm{d}y$	$\int P'\,\mathrm{d}z\,\mathrm{d}y\,\mathrm{d}x$
1	**1.00**	**1.00**
2	0.82	0.79
3	0.61	0.68
4	1.60	2.23
5	**1.00**	**1.00**
6	0.24	0.87
7	-0.30	0.78
8	1.21	2.35
9	**1.00**	**1.00**
10	**1.00**	**1.00**

Table 4.5 shows the integrals for the primary production anomaly data. The first integral gives information on the net disturbance of primary production in the water column at $x \approx 55$ km. The second integral gives information on the net primary production anomaly in the three-dimensional domain. Positive values indicate increased primary production, and negative and red values indicate decreased primary production. The results indicate that the strongest disturbances in primary production are found for experiments 4 and 8, with conditions of both strong wind stress and wind stress reduction ($\tau_{x0} = \Delta\tau = 0.10$ N/m^2). In these experiments, there is a net increase in primary production. For the cross-section integral, experiments 7 and 10 show a reduced primary production. This result underscores the complexity of the ocean dynamics and that arbitrary cross-sections do not sufficiently capture the full extent of the effect OWFs have on the ocean.

Based on all primary production results presented in this chapter, the OWFs seem to create multiple cells of both increased and decreased primary production in the upper ocean. The net effect is generally a locally increased primary production. The size of the wind farm and the strength of the wind stress reduction in the wake seem to be important factors for the magnitude of the disturbance. These results are in alignment with the results of the horizontal integrals of depth-averaged vertical velocity from section 4.1 and also with the Ekman theory from section 2.2.3.

The results give important information that OWFs in fact do disturb primary production. However, the anomalies presented here are quite small. As previously stated, the experiments are idealized, and do not capture the full complexity of the real ocean. To determine the effect such a disturbance in primary production has on marine ecosystems, realistic numerical methods, and if possible, empirical data, would be necessary.

Chapter 5

Further Discussion

5.1 Legal Frameworks

5.1.1 The Offshore Energy Act

All renewable offshore energy production in Norway is regulated by the Offshore Energy Act given by Havenergilova (2010). The law applies to both the Norwegian continental shelf, and the Norwegian offshore territories located outside the baseline (Havenergilova, 2010, §1-2). The aim of the law is to ensure that all offshore energy projects are planned, constructed, and operated in accordance with existing guidelines on environmental considerations, safety, commercial interests and other societal objectives (Havenergilova, 2010, §1-1). The act also states that the Norwegian state holds the exclusive rights to exploit renewable offshore resources (Havenergilova, 2010, §1-3). As a first step in the development of new areas for offshore energy, the law requires a risk assessment to be submitted to public consultation; the assessment must document potential environmental and societal impacts (Havenergilova, 2010, §2-2). Based on selected technical, financial, as well as health, safety and environmental criteria, the designated areas are then assigned to the strongest of several contestants (Havenergilova, 2010, §2-3). Any construction, operation, modification or expansion cannot be carried out without a concession from the Energy Ministry (Havenergilova, 2010, §3-1). The law also outlines the responsibilities of the concessionaires; fishermen are entitled to be financially compensated for loss of fishing grounds, pollution, or waste caused by the site (Havenergilova, 2010, §9).

5.1.2 The Norwegian Water Resources and Energy Directorate

The Norwegian Water Resources and Energy Directorate (NVE) is a directorate underlying the Norwegian Ministry of Energy, responsible for managing the water and energy resources in Norway in a cost- and energy-efficient manner (NVE, 2015). As described by NVE (2023), this includes identifying new areas for renewable energy production offshore. This work is in collaboration with the Directorate of Fisheries, the Norwegian Environment Agency, the Norwegian Coastal Administration, the Norwegian Offshore Directorate and the Norwegian Defense Estates Agency.

The aim of the project is to locate areas that correspond to a cumulative energy production of 30 GW within 2040. There are several criteria to account for when identifying suitable sites. For instance, technical criteria such as wind conditions and ocean depth, as well as the interest of several stakeholders such as fisheries, maritime transport operators and power production companies have been considered. By conducting a suitability analysis, NVE has managed to identify 54000 km^2 with both good technical properties and low levels of interest conflicts spread over 20 areas along the Norwegian coast. Some conflicts of interest do, however, still exist. Before the development of offshore wind energy can start in these areas, additional risk assessments must be conducted as described in section 5.1.1.

5.2 Recommendations from the Institute of Marine Research

IMR serves as an advisory body for the Norwegian government on offshore construction activities in Norway that may impact marine life (Forland et al., 2025). The development of offshore wind energy is an example of such an activity. Every year, IMR provides an updated report that includes a scientific basis, an impact assessment, and advice related to noise impact, specifically (Forland et al., 2025). In addition, the report from 2020 includes a chapter related to offshore wind energy, offering advice for the Ministry of Energy to consider before approving new wind projects (de Jong et al., 2020). As described by de Jong et al. (2020) in the IMR report, the advice covers the effects of noise, electromagnetic fields, changes in ocean currents and vertical light changes on marine life. As further stated by de Jong et al. (2020), the environmental impacts of offshore wind are not yet fully understood, and it is uncertain if the cumulative effect is positive, negative or neutral. Thus, IMR advises against developing wind farms in areas of special importance to marine species, e.g. spawning areas for fish, pupping sites for ocean mammals and areas with coral reefs. IMR also recommends avoiding construction activities during spawning and pupping periods. Other recommendations include developing a standardized framework for future offshore wind projects in Norway. This framework should outline the procedures for collecting data on physical and biological conditions, both before construction, and during the operational phase. The collected data should be publicly available. Noise mitigation measures, e.g. bubble curtains during construction and low-level noise materials for mooring lines, are also recommended. The complete IMR report is available at de Jong et al. (2020).

5.3 Stakeholders Interest in Offshore Wind Energy

Several stakeholders are involved in ocean resources. As explained by Nærings- og fiskeridepartementet (2024), this includes e.g. fisheries and aquaculture, petroleum industry, marine transport, military forces as well as the general population. In Norway, coexistence between the petroleum sector, fishery industry and marine transport sector has existed for decades (Nærings- og fiskeridepartementet, 2024). Now, the Norwegian government wants to invest in offshore wind energy (Norwegian Government, 2022b). The current and future development of OWFs requires large ocean areas. This can potentially have a negative impact on the activities of other stakeholders such as fisheries, marine transport, and military forces. It is important that the ocean areas are utilized in a way that maximizes societal benefits without negatively affecting the environment and other stakeholders (Nærings- og fiskeridepartementet, 2024). To ensure effectiveness during the concession process discussed in section 5.1.1, it is important to have support from all the different stakeholders, as skepticism may cause delays. To increase the acceptance among the stakeholders, more research is needed on the potential risks offshore wind energy poses to the surrounding environment and how to optimize coexistence.

As explained in Åsjord Sire (2023), Offshore Norge, the Norwegian Fishermen’s Association and Fiskebåt have developed a guidebook for coexistence between fisheries and offshore wind energy. The purpose of the guidebook is to avoid conflicts between the different stakeholders.

As suggested by Nærings- og fiskeridepartementet (2024), another possible solution is that offshore wind energy areas can be combined with other activities. This will minimize the total ocean area occupied by different stakeholders and protect the ocean environment. However, more research is needed on the impact the different activities have on each other and the ocean environment (Nærings- og fiskeridepartementet, 2024).

Chapter 6

Limitations

6.1 Numerical Limitations

Numerical models such as ROMS are powerful and useful tools for studying and predicting upper ocean interactions. It is, however, important to be aware of the limitations. As described by Albretsen (2019), numerical simulations are based on simplified primitive equations and assumptions, and the models do not necessarily always capture all ocean dynamics correctly; different input data gives different outcomes, and the quality of the model results depends on several aspects. For realistic results, a realistic model setup is required. This includes using site-specific measurement data to configure initial conditions, bathymetry, and forcing files, using high spatial and temporal resolution that are able to capture small-scale motions, using suitable boundary conditions and couple the model to capture both atmospheric and ocean dynamics including waves, turbulence, friction, river runoff, tides, and other affecting factors of importance. Such realistic models can have a long simulation time, and computational costs can be high (Albretsen, 2019). In addition to the setup itself, Albretsen (2019) also highlights that there are limitations associated with numerical methods in general, as they include approximations and parameterizations based on simplifications and assumptions that inevitably introduce uncertainties and errors of some sort. The type of numerical schemes and the discretization methods of vertical and horizontal grids are examples of sources of error (Albretsen, 2019).

As described in chapter 3, this thesis looked at idealized cases where several factors have been neglected to isolate and focus on upwelling and downwelling processes. Although this gives valuable information about the effect of OWFs on upper ocean variability that can be applicable to real-world conditions, it does not give the full picture, as it fails to capture the impact of e.g. atmospheric forcings, wave forcings, bathymetry, and diurnal and seasonal variability. This is a huge limitation that needs to be addressed. Although outside the scope of this thesis, it could be interesting to expand the research to include more of these factors. For example, as shown in section 1.4, the study of Paskyabi & Fer (2012) outlined the importance of including wave forcing. This illustrates the need for further research on this topic, specifically focusing on realistic scenarios.

Numerical methods are particularly valuable in situations where observational data is limited, difficult to obtain, or simply unavailable e.g. when studying future scenarios. This does, however, introduce another limitation with my work. Due to limited available observational data, the numerical results cannot easily be evaluated and validated by comparison to real data. Nevertheless, as discussed in chapter 4, the results do agree with other similar idealized numerical studies focusing on the same topic.

The analytical Gaussian wake model also introduces additional limitations due to its simple nature. Although useful for studying the basic behavior of the upper ocean in response to wake formation, the Gaussian wake model does not account for all three-dimensional aspects of real scenarios, e.g. turbulence, asymmetric distribution of velocity deficit, and other atmospheric and oceanographic variations (Krutova, 2024). Although outside the scope of this thesis, research highlighting different available wake models and their limitations is described by Krutova (2024).

Numerical limitations also affect the results of the integrals used to evaluate the net effect of OWFs on the different ocean properties. Although the spin-up time was determined based on a stability analysis of the kinetic energy, not all integrals had converged to a steady state by the end of the simulations. This introduces uncertainties that may reduce the reliability of the results and make it more difficult to identify relations between the different findings. To mitigate such uncertainties, future studies should consider extending the duration of the numerical experiments.

To summarize, all numerical models have strengths and weaknesses. As a modeller, it is important to consider these aspects to ensure the selection of a model that is well suited for given applications.

6.2 General Limitations

Other limitations worth mentioning include the exclusion of both diurnal variations in solar radiation, and seasonal variations in temperature, stratification, atmospheric stability, wave forcing, and solar radiation – all of which are relevant when assessing the effect of OWFs on upper ocean variability and primary production. These limitations are a natural consequence of the time constraints and workload limitations set for this thesis.

Chapter 7

Conclusions

In this study, idealized numerical experiments have been used to investigate the effect of OWFs on ocean variability and marine ecosystems. The farm has been analytically modeled using a Gaussian function to simulate the wake. A sensitivity analysis has been performed on single-farm experiments with $L = 5$ km and $L = 10$ km and wind stress parameters $\tau_{x0} = (0.01, 0.08, 0.10)$ N/m^2 and $\Delta\tau = (0.05, 0.10)$ N/m^2, as well as on overlapping-farms experiments with $L = 2 \times 8$ km and $L = 3 \times 8$ km and wind stress parameters $\tau_{x0} = 0.10$ N/m^2 and $\Delta\tau = 0.04$ N/m^2. The Rossby radius of deformation was calculated to be approximately 4 km, which is less than all L used in the experiments. Based on the reduced-gravity model presented by Broström (2008), a rapid and strong oceanic response was thus expected to be seen for all numerical experiments.

The general result obtained from this work is that OWFs can create unbalanced dipoles with upwelling on the southern side and downwelling on the northern side of the farm. The affected area increases when L increases. The magnitude of disturbance increases with L for sea-surface, depth-averaged vertical velocity, temperature, thermocline depth, sound speed, biological tracers and primary production. The opposite is true for normalized surface horizontal convergence, vertical velocity close to the surface and vertical Ekman pumping. In alignment with Broström (2008) and Ekman theory (Marshall & Plumb, 2008), strong wind stress reduction was shown to be a determining factor for the magnitude of disturbance for all studied properties except for sound speed, for which no such relation could be seen. Some of the studied properties showed results that align with each other, but others did not. Looking at the entire water column, the results of vertical velocity, temperature, and primary production all indicate a net upwelling. Focusing on the upper ocean, the results of both the sea-surface elevation, Ekman pumping and sound speed indicate a net upwelling whereas the results of the surface convergence and vertical velocity indicate net downwelling. Thus, the results indicate that the effect of the wind farms is complex and varies with depth in the water column. This complexity and local effects make it challenging to conclude whether the net effect of offshore wind turbines on the upper ocean variability and marine ecosystems is positive, negative, or neutral.

The results presented in this thesis suggest that the presence of wind farms causes a modification (slight net reduction) in sound speed close to the surface and a net increased primary production in the nearby area. Although these findings provide a solid foundation for evaluating the impact of OWFs on upper ocean variability and marine ecosystems, the results require additional exploration to determine whether the impact is strong enough to cause significant disruption in food availability, communication, navigation, and behavior of different ocean animals. Potential consequences for different stakeholders should also be addressed through more site-specific and realistic studies – both numerical and empirical – conducted at existing test sites such as Hywind Tampen, before future large-scale OWF projects are implemented.

Overall, the study emphasizes the importance of including wind wake effects in the mandatory risk assessment required in the early stages of offshore wind project development, as regulated by Havenergilova (2010). Idealized numerical studies such as the one presented in this thesis give valuable insight into the environmental effect of OWFs. It is, however, important to be aware and mindful of the limitations introduced through assumptions and simplifications of the method. Until the complexity of environmental impacts is fully understood, the findings of this study – along with results of other more realistic numerical studies – can serve as an initial guideline to ensure that the interests of all stakeholders are considered in the development of future offshore wind projects.

Chapter 8

Future Work

In this thesis, only idealized numerical experiments have been studied. Although they give valuable insight into basic ocean dynamics, they do not capture the complexity of real ocean dynamics. To gain realistic results, future work should include realistic numerical experiments. This should include site-specific input data on wind and wave forcing, bathymetry, stratification, and tracers, as well as a more advanced and realistic wake model. Future studies should also account for both diurnal and seasonal variations in stratification, atmospheric stability, wind and wave forcing, and solar radiation. Long-term effects would also be of interest. In addition, empirical data should be gathered from existing OWF sites, such as Hywind Tampen, to complement the numerical studies.

This thesis covered the effect of wind farms on sound speed close to the surface. Future numerical projects should take it one step further and use the calculated sound speed profiles as input for sound propagation models. As described by Farcas et al. (2016), modeling of underwater sound propagation is well established, with several methods available. For example, the BELLHOP model is described by Porter (2011) as a beam tracing model that is applicable for predicting acoustic pressure fields in the ocean. Model outputs include transmission loss, eigenrays, arrivals, and received time-series (Porter, 2011).

Chapter 9

Declaration of the Use of Artificial Intelligence

During the writing process of this thesis, I have used ChatGPT-4 as a learning tool. ChatGPT can be a useful tool when used correctly, but can also provide misleading and straight up wrong information if used incorrectly or uncritically. It is important not to trust ChatGPT above your own knowledge and logic, and it is important not to let ChatGPT become ”your new brain”.

I have mainly used ChatGPT for the following:

- when I have been stuck with my coding or dealt with errors while learning Fortran and while processing ROMS output data in Python, xroms and MatLab
- to help me with the format or to make figures and tables in Latex
- to explain hard-to-grasp concepts in Norwegian to make them easier to comprehend
- to summarize the main points of long articles post reading them myself to make sure I have understood the key aspects correctly
- to generate lists of synonyms for certain words

I have ***not*** used ChatGPT for the following:

- to generate or write sentences or paragraphs for me. I enjoy writing and creating my own sentences. ChatGPT can be a good tool for finding words, but I do not like using it to generate sentences for me. I think it kills my creativity and writing flow.
- to summarize articles or books I have not read myself first
- to write theory. It is not a reliable source for complex scientific information, and should not be used as one.

With that being said, all scientific analysis, interpretations, discussions and conclusions are exclusively my own and have been made based on theory and prior studies presented in cited literature.

Bibliography

Affatati, A., Scaini, C., & Salon, S. (2022). Ocean sound propagation in a changing climate: Global sound speed changes and identification of acoustic hotspots. *Earth's Future*, *10*, e2021EF002099. URL: https://agupubs.onlinelibrary.wiley.com/doi/abs/10.1029/2021EF002099. doi:https://doi.org/10.1029/2021EF002099. E2021EF002099 2021EF002099.

Albretsen, J. (2019). Ocean models. URL: https://www.hi.no/en/hi/forskning/research-data-1/models/ocean-models [Online; accessed 20. Mar. 2025].

Allaby, M. (2010). assimilation efficiency. URL: https://www.oxfordreference.com/view/10.1093/acref/9780199567669.001.0001/acref-9780199567669-e-6057. doi:10.1093/acref/9780199567669.013.6057.

Arango, H. G., & Shchepetkin, A. F. (2024). ROMS > start. URL: https://www.myroms.org [Online; accessed 2. Sep. 2024].

Broström, G. (2008). On the influence of large wind farms on the upper ocean circulation. *Journal of Marine Systems*, *74*, 585–591. URL: https://www.sciencedirect.com/science/article/pii/S0924796308001085. doi:https://doi.org/10.1016/j.jmarsys.2008.05.001.

Burton, T. L., Jenkins, N., Bossanyi, E., Sharpe, D., & Graham, M. (2021). *Wind Energy Handbook (3rd Edition)*. (Third edition ed.). Newark: John Wiley & Sons.

Christiansen, N., Daewel, U., Djath, B., & Schrum, C. (2022a). Emergence of large-scale hydrodynamic structures due to atmospheric offshore wind farm wakes. *Frontiers in Marine Science*, *9*. URL: https://www.frontiersin.org/journals/marine-science/articles/10.3389/fmars.2022.818501. doi:10.3389/fmars.2022.818501.

Christiansen, N., Daewel, U., & Schrum, C. (2022b). Tidal mitigation of offshore wind wake effects in coastal seas. *Frontiers in Marine Science*, *9*. URL: https://www.frontiersin.org/journals/marine-science/articles/10.3389/fmars.2022.1006647. doi:10.3389/fmars.2022.1006647.

Daewel, U., Akhtar, N., Christiansen, N., & Schrum, C. (2022). Offshore Wind Wakes - the underrated impact on the marine ecosystem. doi:10.21203/rs.3.rs-1720162/v1 [Online; accessed 26. Feb. 2025].

Desalegn, B., Gebeyehu, D., Tamrat, B., Tadiwose, T., & Lata, A. (2023). Onshore versus offshore wind power trends and recent study practices in modeling of wind turbines' life-cycle impact assessments. *Cleaner Engineering and Technology*, *17*, 100691. URL: `https://www.sciencedirect.com/science/article/pii/S2666790823000964`. doi:`https://doi.org/10.1016/j.clet.2023.100691`.

DMCS Ocean Modeling Group (2025). ROMS > start. URL: `https://www.myroms.org` [Online; accessed 1. Mar. 2025].

Drange, H. (2024). Gjennomgang av deler av kapittel 6, 7, 8 og 10 i marshall & plumb (2008). URL: `https://folk.uib.no/ngfhd/Teaching/Div/geof110_v2024.pdf` [Online; accessed 13. Feb. 2024].

Ehrlich, R. (2013). *Renewable energy : a first course*. Boca Raton, Fla: CRC Press.

EIA (2023). History of wind power - U.S. Energy Information Administration (EIA). URL: `https://www.eia.gov/energyexplained/wind/history-of-wind-power.php` [Online; accessed 19. Feb. 2025].

Equinor (2019). Hywind tampen, pud del ii - konsekvensutredning. URL: `https://cdn.equinor.com/files/h61q9gi9/global/59db109a1ab7991e6b7546ef9b161dcfa74ec514.pdf?hywind-tampen-pud-del-II-konsekvensutredning-mars-2019-equinor.pdf` [Online; accessed 14. Jan. 2025].

Equinor (2024). Hywind Tampen. URL: `https://www.equinor.com/no/energi/hywind-tampen` [Online; accessed 27. Aug. 2024].

Equinor (2025a). Equinor vil utvikle havvind i Norge. URL: `https://www.equinor.com/no/energi/havvind-i-norge` [Online; accessed 19. Feb. 2025].

Equinor (2025b). Havvind. URL: `https://www.equinor.com/no/energi/havvind` [Online; accessed 19. Feb. 2025].

Farcas, A., Thompson, P. M., & Merchant, N. D. (2016). Underwater noise modelling for environmental impact assessment. *Environmental Impact Assessment Review*, *57*, 114–122. URL: `https://www.sciencedirect.com/science/article/pii/S0195925515300202`. doi:`https://doi.org/10.1016/j.eiar.2015.11.012`.

Fennel, K., Wilkin, J., Levin, J., Moisan, J., O'Reilly, J., & Haidvogel, D. (2006). Nitrogen cycling in the middle atlantic bight: Results from a three-dimensional model and implications for the north atlantic nitrogen budget. *Global Biogeochemical Cycles*, *20*. URL: `https://agupubs.onlinelibrary.wiley.com/doi/abs/10.1029/2005GB002456`. doi:`https://doi.org/10.1029/2005GB002456`. `arXiv:https://agupubs.onlinelibrary.wiley.com/doi/pdf/10.1029/2005GB002456`.

Firouz, S. M., Allahyaribeik, S., Ezaam, M., Bidokhti, A. A. A. A., & Soheylifar, M. R. (2024). Sound propagation simulation in the strait of hormuz using roms and ramgeo models. *International Journal of Environmental Science and Technology*, *21*, 7269–7294.

URL: https://link.springer.com/article/10.1007/s13762-024-05541-8. doi:https://doi.org/10.1007/s13762-024-05541-8. [Online; accessed 10. Mar. 2025].

Floeter, J., Pohlmann, T., Harmer, A., & Möllmann, C. (2022). Chasing the offshore wind farm wind-wake-induced upwelling/downwelling dipole. *Frontiers in Marine Science*, *9*. URL: https://www.frontiersin.org/journals/marine-science/articles/10.3389/fmars.2022.884943. doi:10.3389/fmars.2022.884943.

Forland, T. N., Sivle, L. D., de Jong, K., Pedersen, G., McQueen, K., Strømme, M. L., Kutti, T., Durif, C., Grimsbø, E., & Wehde, H. (2025). Havforskningsinstituttets rådgivning for menneskeskapt støy i havet. *Havforksningsinstitutttet*, *1*. URL: https://www.hi.no/hi/nettrapporter/rapport-fra-havforskningen-2025-1. [Online; accessed 10. Mar. 2025].

GEBCO (2024). GEBCO data download. URL: https://download.gebco.net [Online; accessed 4. Feb. 2025].

Gnedin, N. Y., Semenov, V. A., & Kravtsov, A. V. (2018). Enforcing the courant–friedrichs–lewy condition in explicitly conservative local time stepping schemes. *Journal of Computational Physics*, *359*, 93–105. URL: https://www.sciencedirect.com/science/article/pii/S0021999118300184. doi:https://doi.org/10.1016/j.jcp.2018.01.008.

González-Longatt, F., Wall, P., & Terzija, V. (2012). Wake effect in wind farm performance: Steady-state and dynamic behavior. *Renewable Energy*, *39*, 329–338. doi:10.1016/j.renene.2011.08.053.

Haidvogel, D., Shchepetkin, A., & Arango, H. (2013). The regional ocean modeling system: New time-stepping algorithms to reduce mode-splitting error and to ensure constancy preservation. *Recent developments in numerical methods for atmosphere and ocean modelling*, (pp. 151–162).

Havenergilova (2010). Lov om fornybar energiproduksjon til havs (lov-2010-06-04-21). Lovdata. URL: https://lovdata.no/dokument/NL/lov/2010-06-04-21.

Holme, O. S., & Equinor (2022). Gomo vedlegg a hywind tampen. URL: https://www.offshorenorge.no/contentassets/06a63e26e3584ce5970ab92e4371cb6f/vedlegg-a/faste-innretninger/gomo-vedlegg-a-hywind-tampen-rev3.pdf [Online; accessed 4. Feb. 2025].

Holt, J., Wakelin, S., & Huthnance, J. (2009). Down-welling circulation of the northwest european continental shelf: A driving mechanism for the continental shelf carbon pump. *Geophysical Research Letters*, *36*. URL: https://agupubs.onlinelibrary.wiley.com/doi/abs/10.1029/2009GL038997. doi:https://doi.org/10.1029/2009GL038997.

IEA (2024). Electricity Mid-Year Update, IEA, Paris. URL: https://www.iea.org/reports/electricity-mid-year-update-july-2024 [Online; accessed 19. Feb. 2025].

Jakobsen, A., & IMR (2024). 10 ting du ikke visste om plankton. URL: https://www.hi.no/hi/nyheter/2024/april/10-ting-du-ikke-visste-om-plankton [Online; accessed 16. Dec. 2024].

Jensen, F. B., Kuperman, W. A., Porter, M. B., & Schmidt, H. (2011). *Computational Ocean Acoustics*. Modern Acoustics and Signal Processing (2nd ed.). New York, NY: Springer Nature.

de Jong, K. (2024). Prosjekt #2677029 - windsys: Effects of floating wind farms on the marine ecosystem, with a focus on pelagic fish. - cristin. URL: `https://app.cristin.no/projects/show.jsf?id=2677029` [Online; accessed 5. Aug. 2025].

de Jong, K., Steen, H., Forland, T. N., Wehde, H., Nyqvist, D., Palm, A. C. U., Nilssen, K. T., Albretsen, J., Falkenhaug, T., Biuw, M., Buhl-Mortensen, L., & Sivle, L. D. (2020). Potensielle effekter av havvindanlegg på havmiljøet. *Havforskningsinstituttet*, . URL: `https://www.hi.no/hi/nettrapporter/rapport-fra-havforskningen-2020-42`. [Online; accessed 3. Mar. 2025].

Krutova, M. (2024). Investigation of offshore wind turbine wakes by numerical modeling and full-scale measurements. URL: `https://hdl.handle.net/11250/3127653`.

Krutova, M., Paskyabi, M. B., Nielsen, F. G., & Reuder, J. (2020). Evaluation of Gaussian wake models under different atmospheric stability conditions: Comparison with large eddy simulation results. *J. Phys. Conf. Ser.*, *1669*, 012016. doi:`10.1088/1742-6596/1669/1/012016`.

Lian, Z., Liu, K., & Yang, T. (2022). Potential influence of offshore wind farms on the marine stratification in the waters adjacent to china. *Journal of Marine Science and Engineering*, *10*. URL: `https://www.mdpi.com/2077-1312/10/12/1872`. doi:`10.3390/jmse10121872`.

Liu, K., Du, J., Larsén, X. G., & Lian, Z. (2023). Spatiotemporal variations of ocean upwelling and downwelling induced by wind wakes of offshore wind farms. *Journal of Marine Science and Engineering*, *11*. URL: `https://www.mdpi.com/2077-1312/11/10/2020`. doi:`10.3390/jmse11102020`.

Longhurst, A. R. (2007). Chapter 3 - fronts and pycnoclines: Ecological discontinuities. In A. R. Longhurst (Ed.), *Ecological Geography of the Sea (Second Edition)* (pp. 35–49). Burlington: Academic Press. (Second edition ed.). URL: `https://www.sciencedirect.com/science/article/pii/B9780124555211500048`. doi:`https://doi.org/10.1016/B978-012455521-1/50004-8`.

Lopes, M., Tonelli, M., & Cernicchiaro, G. (2024). Upwelling-driven variation of sound speed profile in a brazilian bay monitored by a coastal acquisition system. *Anais da Academia Brasileira de Ciências*, *96*. doi:`10.1590/0001-3765202420230846`.

Mackenzie, F. T., & Byrne, R. H. (2025). Seawater - chemical and physical properties of seawater - acoustic properties — britannica. URL: `https://www.britannica.com/science/seawater/Acoustic-properties` [Online; accessed 6. Jul. 2025].

Marshall, J., & Plumb, R. A. (2008). *Atmosphere, ocean, and climate dynamics: an introductory text*. (1st ed.). Burlington, MA: Elsevier Academic Press.

Miller, S., Lopera, L., & Bracco, A. (2022). Why Are the Eastern Margins of Ocean Basins Full of Fish? *Front. Young Minds*, . URL: https://kids.frontiersin.org/articles/10.3389/frym.2022.704120. [Online; accessed 26. Feb. 2025].

Mulder, C., & Hendriks, A. J. (2014). Half-saturation constants in functional responses. *Global Ecology and Conservation*, *2*, 161–169. URL: https://www.sciencedirect.com/science/article/pii/S2351989414000420. doi:https://doi.org/10.1016/j.gecco.2014.09.006.

Mæland, R. B. (2022). Får støtte til å forske på flytande havvind — havforskningsinstituttet. URL: https://www.hi.no/hi/nyheter/2022/juni/far-stotte-til-nytt-havvind-prosjekt [Online; accessed 5. Aug. 2025].

NASA (2024). What Is Climate Change? - NASA Science. URL: https://science.nasa.gov/climate-change/what-is-climate-change [Online; accessed 19. Feb. 2025].

Naturvernforbundet (2025). Havvind. URL: https://naturvernforbundet.no/havvind/?gad_source=1&gclid=CjwKCAiAn9a9BhBtEiwAbKg6fuypyuUbuagV1M0fjfxpvYCLKUvjUbXm2HKWdUjzLR_73obUm0t_sxoCCJMQAvD_BwE [Online; accessed 19. Feb. 2025].

NOAA (2011). Ocean currents. URL: https://www.noaa.gov/education/resource-collections/ocean-coasts/ocean-currents [Online; accessed 14. Nov. 2024].

NOAA (2024a). What are phytoplankton? URL: https://oceanservice.noaa.gov/facts/phyto.html [Online; accessed 16. Dec. 2024].

NOAA (2024b). What are plankton? URL: https://oceanservice.noaa.gov/facts/plankton.html [Online; accessed 16. Dec. 2024].

NORCE (2025). Offshore Wind Energy. URL: https://www.norceresearch.no/en/research-theme/offshore-wind [Online; accessed 19. Feb. 2025].

Norwegian Government (2022a). Havvind blir Norges neste eksporteventyr. URL: https://www.regjeringen.no/no/aktuelt/havvind-blir-norges-neste-eksporteventyr/id2949198.

Norwegian Government (2022b). Kraftfull satsing på havvind. URL: https://www.regjeringen.no/no/aktuelt/kraftfull-satsing-pa-havvind/id2912297.

NVE (2015). Dette er nve - nve. URL: https://www.nve.no/om-nve/dette-er-nve/ [Online; accessed 11. Mar. 2025].

NVE (2023). Identifisering av utredningsområder for havvind: Sammendrag - del 1. URL: https://veiledere.nve.no/havvind/identifisering-av-utredningsomrader-for-havvind/sammendrag/sammendrag-del-1/ [Online; accessed 11. Mar. 2025].

NVE (2024). Hvor kommer strømmen fra? - NVE. URL: https://www.nve.no/energi/

energisystem/kraftproduksjon/hvor-kommer-stroemmen-fra [Online; accessed 27. Aug. 2024].

Nærings- og fiskeridepartementet (2024). Næringsplan for norske havområder. URL: https://www.regjeringen.no/no/dokumenter/naringsplan-for-norske-havomrader/id3046882/?ch=6 [Online; accessed 12. Mar. 2025].

Palm, A. C. U., Hareide, N. R., de Jong, K., Tenningen, M., & Dankel, D. L. (2023). Kunnskapsinnhenting for Sameksistens mellom fiskeri- og havvindsnæring. *Havforskningsinstituttet*, . URL: https://www.hi.no/hi/nettrapporter/rapport-fra-havforskningen-2023-40. [Online; accessed 25. Feb. 2025].

Palm, A. C. U., de Jong, K., Pedersen, G., Saltskår, J., Hovland, T., Renner, A., Mihaljevic, M., Wilhelmsen, J. F., Drivenes, L., Bergamasco, A., Falcieri, F., Majaneva, M., Critchley, E. J., Kühn, S., Viotti, F., & Akkaş, K. (2025). Cruise report hywind tampwn 19 to 26 october 2024 — institute of marine research. URL: https://www.hi.no/en/hi/nettrapporter/toktrapport-en-2025-7 [Online; accessed 5. Aug. 2025].

Paskyabi, M. B. (2015). Offshore wind farm wake effect on stratification and coastal upwelling. *Energy Procedia*, *80*, 131–140. URL: https://www.sciencedirect.com/science/article/pii/S1876610215021475. doi:https://doi.org/10.1016/j.egypro.2015.11.415. 12th Deep Sea Offshore Wind R&D Conference, EERA DeepWind'2015.

Paskyabi, M. B., & Fer, I. (2012). Upper Ocean Response to Large Wind Farm Effect in the Presence of Surface Gravity Waves. *Energy Procedia*, *24*, 245–254. doi:10.1016/j.egypro.2012.06.106.

Porter, M. B. (2011). The bellhop manual and user's guide: Preliminary draft. URL: http://oalib.hlsresearch.com/Rays/HLS-2010-1.pdf [Online; accessed 2. Apr. 2025].

Raghukumar, K., Nelson, T., Jacox, M., Chartrand, C., Fiechter, J., Chang, G., Cheung, L., & Roberts, J. (2023). Projected cross-shore changes in upwelling induced by offshore wind farm development along the California coast. *Commun. Earth Environ.*, *4*, 1–12. doi:10.1038/s43247-023-00780-y.

Rivera-Arreba, I., Wise, A. S., Eliassen, L. V., & Bachynski-Polić, E. E. (2023). Effect of atmospheric stability on the dynamic wake meandering model applied to two 12mw floating wind turbines. *Wind Energy*, *26*, 1235–1253. URL: https://onlinelibrary.wiley.com/doi/abs/10.1002/we.2867. doi:https://doi.org/10.1002/we.2867. arXiv:https://onlinelibrary.wiley.com/doi/pdf/10.1002/we.2867.

Sallée, J.-B., Pellichero, V., Akhoudas, C., Pauthenet, E., Vignes, L., Schmidtko, S., Garabato, A. N., Sutherland, P., & Kuusela, M. (2021). Summertime increases in upper-ocean stratification and mixed-layer depth. *Nature*, *591*, 592–598. doi:10.1038/s41586-021-03303-x.

Segtnan, O. H., & Christakos, K. (2015). Effect of offshore wind farm design on the vertical motion of the ocean. *Energy Procedia*, *80*, 213–222. doi:10.1016/j.egypro.2015.11.424.

Shchepetkin, A. F., & McWilliams, J. C. (2005). The regional oceanic modeling system (roms): a split-explicit, free-surface, topography-following-coordinate oceanic model. *Ocean Modelling*, *9*, 347–404. URL: https://www.sciencedirect.com/science/article/pii/S1463500304000484. doi:https://doi.org/10.1016/j.ocemod.2004.08.002.

Shchepetkin, A. F., & McWilliams, J. C. (2009). Computational kernel algorithms for fine-scale, multiprocess, longtime oceanic simulations. In R. M. Temam, & J. J. Tribbia (Eds.), *Special Volume: Computational Methods for the Atmosphere and the Oceans* (pp. 121–183). Elsevier volume 14 of *Handbook of Numerical Analysis*. URL: https://www.sciencedirect.com/science/article/pii/S1570865908012020. doi:https://doi.org/10.1016/S1570-8659(08)01202-0.

Sigman, D. M., & Hain, M. P. (2012). The biological productivity of the ocean. *Nature Education Knowledge*, *3*, 21. URL: https://www.nature.com/scitable/knowledge/library/the-biological-productivity-of-the-ocean-70631104/. [Online; accessed 12. Aug. 2025].

Åsjord Sire, E. (2023). Anbefalt praksis for sameksistens mellom fiskeri og havvind: Nå kan du laste ned dreieboka. URL: https://www.offshorenorge.no/om-oss/nyheter/2023/12/dreiebok/ [Online; accessed 12. Mar. 2025].

Statkraft (2025). Vindkraft | Statkraft. URL: https://www.statkraft.no/var-virksomhet/vindkraft/?gad_source=1&gclid=CjwKCAiAn9a9BhBtEiwAbKg6fvZkg7_SOGHOOZ9-8FZRQ-cD8SggA7dgkCctL2NirMOKTR6IY5TFjhoCPxEQAvD_BwE [Online; accessed 19. Feb. 2025].

Stull, R. B. (1988). *An Introduction to Boundary Layer Meteorology* volume 13 of *Atmospheric and Oceanographic Sciences Library*. (1988th ed.). Dordrecht: Springer Netherlands.

Talley, L. D., Pickard, G. L., Emery, W. J., & Swift, J. H. (2011a). Chapter 3 - Physical Properties of Seawater. In *Descriptive Physical Oceanography (Sixth Edition)* (pp. 29–65). Cambridge, MA, USA: Academic Press. doi:10.1016/B978-0-7506-4552-2.10003-4.

Talley, L. D., Pickard, G. L., Emery, W. J., & Swift, J. H. (2011b). Chapter 4 - Typical Distributions of Water Characteristics. In *Descriptive Physical Oceanography (Sixth Edition)* (pp. 67–110). Cambridge, MA, USA: Academic Press. doi:10.1016/B978-0-7506-4552-2.10004-6.

Talley, L. D., Pickard, G. L., Emery, W. J., & Swift, J. H. (2011c). Chapter 7 - Dynamical Processes for Descriptive Ocean Circulation. In *Descriptive Physical Oceanography (Sixth Edition)* (pp. 187–221). Cambridge, MA, USA: Academic Press. doi:10.1016/B978-0-7506-4552-2.10007-1.

Thyng, K., Hetland, R., Filipe, Renkl, C., Smith, M., Constantinou, N. C., Xomchuk, V. R., & rsignell (2024a). xoceanmodel/xroms: v0.6.1. URL: https://doi.org/10.5281/zenodo.14003363. doi:10.5281/zenodo.14003363.

Thyng, K., Hetland, R., Filipe, Renkl, C., Smith, M., Constantinou, N. C., Xomchuk, V. R., & rsignell (2024b). xroms documentation. URL: https://xroms.readthedocs.io/en/latest/.

Thyng, K., Hetland, R., Filipe, Renkl, C., Smith, M., Constantinou, N. C., Xomchuk, V. R., & rsignell (2024c). xroms.derived. URL: https://xroms.readthedocs.io/en/latest/generated/xroms.derived.html#xroms.derived.convergence.

Thyng, K., Hetland, R., Filipe, Renkl, C., Smith, M., Constantinou, N. C., Xomchuk, V. R., & rsignell (2024d). xroms.utilities. URL: https://xroms.readthedocs.io/en/latest/generated/xroms.utilities.html#module-xroms.utilities.

Turbeville, J. (2014). Plankton Station. URL: https://home.miracosta.edu/kmeldahl/VOBT/AFLcontents/planktonstation.htm [Online; accessed 14. Nov. 2024].

UCAR (2025). Ocean Upwelling | Center for Science Education. URL: https://scied.ucar.edu/learning-zone/how-climate-works/ocean-upwelling [Online; accessed 26. Feb. 2025].

UNA Norway (2024). FNs bærekraftsmål. URL: https://fn.no/om-fn/fns-baerekraftsmaal [Online; accessed 19. Feb. 2025].

UNFCCC (2024). The Paris Agreement | UNFCCC. URL: https://unfccc.int/process-and-meetings/the-paris-agreement [Online; accessed 27. Aug. 2024].

United Nations (2024). THE 17 GOALS | Sustainable Development. URL: https://sdgs.un.org/goals [Online; accessed 27. Aug. 2024].

United Nations Environment Programme (2024). Emissions Gap Report 2024: No more hot air … please! With a massive gap between rhetoric and reality, countries draft new climate commitments. URL: https://wedocs.unep.org/20.500.11822/46404.

Webb, Paul and Roger Williams University (2025). 6.3 Density. URL: https://rwu.pressbooks.pub/webboceanography/chapter/6-3-density [Online; accessed 17. Feb. 2025].

Wells, N. C. (2003). OCEAN CIRCULATION | General Processes. In *Encyclopedia of Atmospheric Sciences* (pp. 1528–1540). Cambridge, MA, USA: Academic Press. doi:10.1016/B0-12-227090-8/00276-1.

Wiki ROMS (2008). Wind-driven upwelling/downwelling over a periodic channel test case. URL: https://www.myroms.org/wiki/UPWELLING_CASE [Online; accessed 6. Jun. 2025].

Wiki ROMS (2016). Numerical Solution Technique - WikiROMS. URL: https://www.myroms.org/wiki/Numerical_Solution_Technique [Online; accessed 24. Jan. 2025].

Wiki ROMS (2019a). Boundary Conditions - WikiROMS. URL: https://www.myroms.org/wiki/Boundary_Conditions [Online; accessed 1. Mar. 2025].

Wiki ROMS (2019b). Vertical S-coordinate - WikiROMS. URL: https://www.myroms.org/wiki/Vertical_S-coordinate [Online; accessed 24. Jan. 2025].

Wiki ROMS (2020a). Fennel Model Input Script - bio_Fennel.in. URL: https://www.myroms.org/wiki/bio_Fennel.in [Online; accessed 18. Apr. 2025].

Wiki ROMS (2020b). Variables. URL: https://www.myroms.org/wiki/Variables#Z [Online; accessed 12. Aug. 2025].

Wiki ROMS (2021). Standard Input Script - roms.in. URL: https://www.myroms.org/wiki/roms.in#Tracer_Advection_Schemes [Online; accessed 18. Apr. 2025].

Wiki ROMS (2022). ROMS History. URL: https://www.myroms.org/wiki/Regional_Ocean_Modeling_System_(ROMS) [Online; accessed 16. Dec. 2024].

Wiki ROMS (2024). Equations of Motion - WikiROMS. URL: https://www.myroms.org/wiki/Equations_of_Motion [Online; accessed 15. Jan. 2025].

WindEurope (2022). Offshore wind energy | WindEurope. URL: https://windeurope.org/policy/topics/offshore-wind-energy [Online; accessed 27. Aug. 2024].

Zhu, Y., Zhang, R., Li, D., & Chen, D. (2020). The thermocline biases in the tropical north pacific and their attributions. *Journal of Climate*, *34*, 1–17. doi:10.1175/JCLI-D-20-0675.1.

Appendix A

Hywind Tampen Wind Farm

Hywind Tampen has been fully operating since August of 2023, and is the current largest offshore floating wind farm in the world (Equinor, 2024). As shown in Fig. A.1, the wind farm is located 140 km off the coast of Gulen, Norway, in the North Sea, between existing oil rigs Snorre and Gullfaks (Equinor, 2024). Hywind Tampen is a test project, where the objectives include development of technology that reduces costs and accelerate future large-scale floating wind farms (Equinor, 2024).

The wind farm is the first of its kind to deliver energy to oil rigs; with a total capacity of 88 MW, the wind farm can cover approximately 35% of the power demand for Snorre and Gullfaks (Equinor, 2024). As a direct consequence, the dependency on gas fuel is estimated to decrease to a level where the associated emissions of CO_2 and NO_x are reduced by an annual average of 200000 tons and 1000 tons, respectively (Equinor, 2019, p. 15).

The farm consists of 11 floating wind turbines HY01-HY11, each of which is mounted on a floating concrete spar structure and connected to a shared anchoring system (Equinor, 2024). The configuration of the wind turbines is shown in Fig. A.1b. The total area of the wind farm covers about 11 km^2 on the ocean surface and 22 km^2 on the sea floor (Equinor, 2019, p. 31). Measured from the ocean surface to the tip of the rotor, the turbines have a total height of 190 m, with a rotor diameter of 167 m (Equinor, 2019, p. 25). Hywind Tampen wind farm is located on the western slope of the Norwegian trench, where the depth of the ocean ranges between 260 and 300 meters (Equinor, 2019; Palm et al., 2023). The detailed bathymetry is illustrated in Fig. A.2.

As described by Palm et al. (2023), there is a lot of fishing activity near Hywind Tampen, primarily targeting pelagic species such as herring and blue whiting, as well as bottom-dwelling fish like saithe and hake. The wind farm is also near spawning areas for haddoc and cod. Palm et al. (2023) also states that there is currently very limited research available on the effect of floating wind farms on fish. However, in the Hywind Tampen area post-construction, schools of herring have been observed close to the surface, and ling, tusk and saithe have been observed around the anchor chains at the sea floor (Palm et al., 2023).

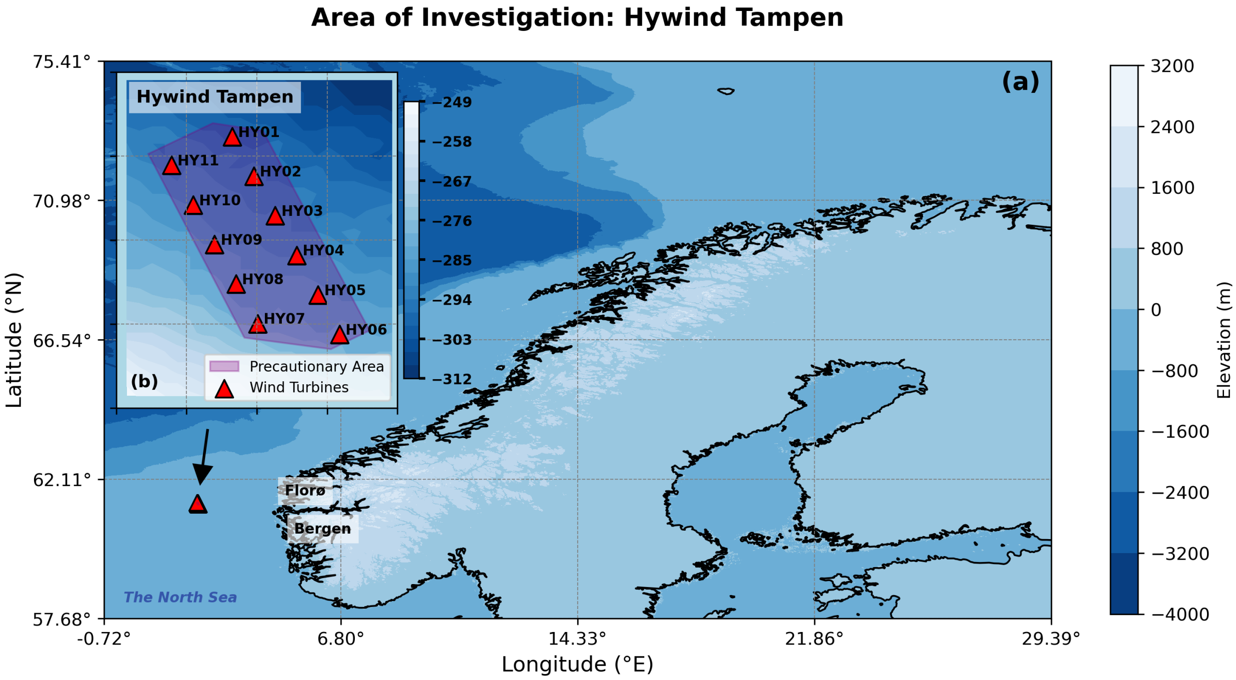

Figure A.1: a) Overview of Hywind Tampen wind farm located in the North Sea, about 140 km off the West Coast of Norway. b) The configuration of the 11 turbines HY01-HY11. The wind turbines are represented as red (—) triangles. Figure is inspired by Holme & Equinor (2022) and generated with python using bathymetry from GEBCO (2024) and turbine coordinates from Holme & Equinor (2022).

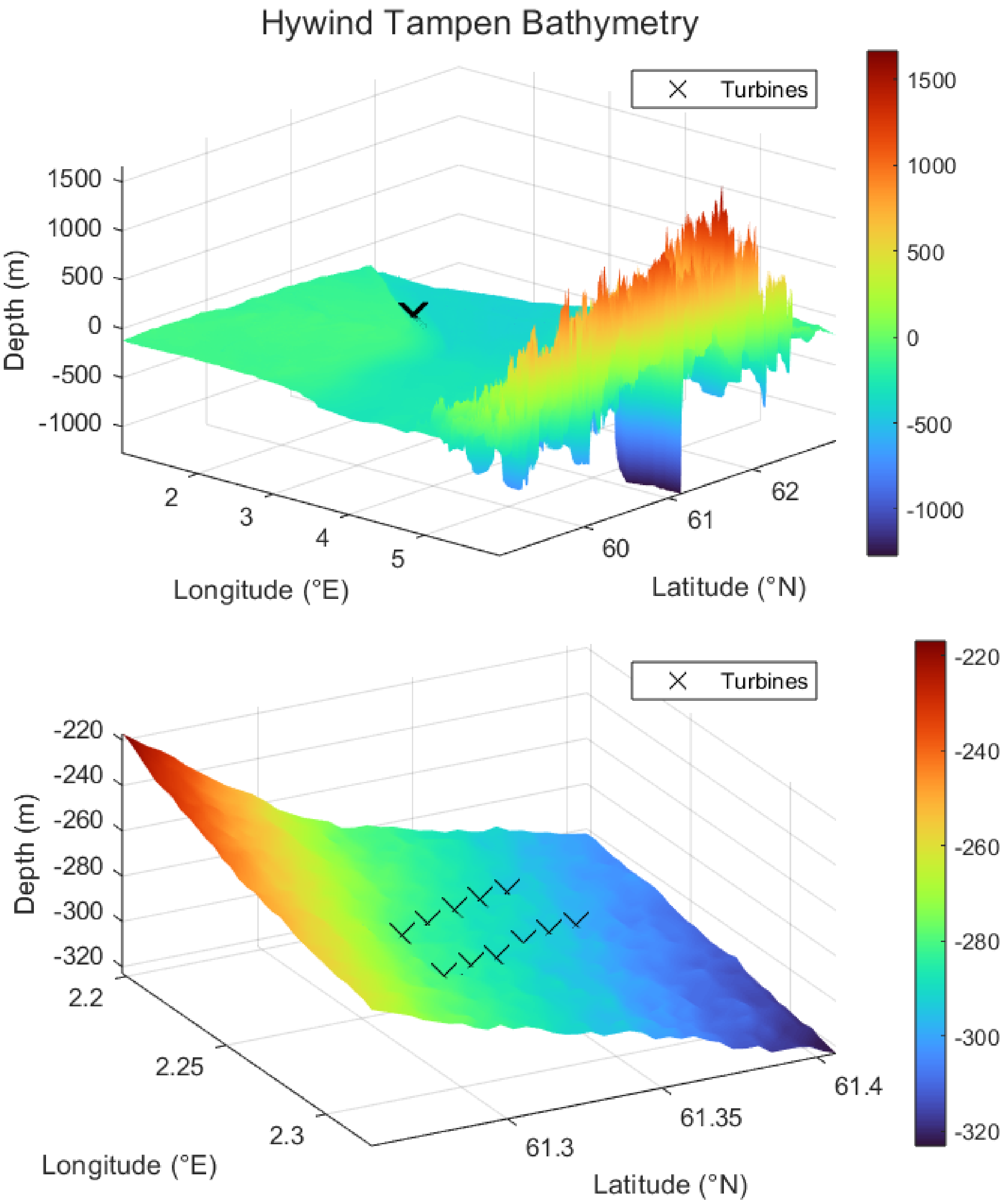

Figure A.2: Detailed bathymetry at Hywind Tampen wind farm. The locations of the turbines are indicated by the black (—) crosses. Figure is generated in MatLab using bathymetry from GEBCO (2024) and turbine coordinates from Holme & Equinor (2022).

Appendix B

WindSYS Cruise to Hywind Tampen 2024

As part of a broader learning process related to my thesis, I participated in the WindSYS cruise to Hywind Tampen with IMR from October 19th to October 26th 2024. This was a unique and enjoyable experience, providing valuable insight into how ocean research is conducted from a vessel – in this case G.O. SARS. It was also very cool to see the wind turbines up close, as shown in Fig. B.1.

The WindSYS project is a collaboration between research institutions, industry stakeholders, and public authorities (Mæland, 2022). The partners involved include IMR, UiB, NINA, SINTEF, Runde Miljøsenter, Fiskeridirektoratet, Fiskebåt, Equinor, Norges Fiskarlag, Norsk Olje og Gass, NVE, Miljødirektoratet, as well as research institutions in Scotland, the Netherlands, and Germany (Mæland, 2022). The project is led by IMR researcher Karen de Jong, and focuses on the effects of floating OWFs on marine ecosystems, specifically pelagic fish (de Jong, 2024). Its objectives include developing detailed documentation of behavioral changes in pelagic fish following the construction phase of Hywind Tampen, based on measured farm-induced noise and vibrations (de Jong, 2024). The most recent cruise report is available at Palm et al. (2025).

During the week at sea, I got to assist several researchers in their work. This included helping retrieve water samples from Niskin bottles on the CTD, and prepare them for eDNA (environmental DNA) and nutrient analysis. With eDNA, one of the researchers was trying to find out which species are or have previously been in the area. These samples were filtrated and the filters were then collected to conduct further analysis back home.

Another research group studied turbulence and zooplankton. They conducted turbulence measurements using an MSS-probe (micro CTD). However, the probe did not work properly the first days. It only worked in a basket with seawater, but not in the actual ocean. Luckily they were able to fix it, and they got some measurements from both the Sognefjord and at Hywind Tampen. They also collected water from CTD Niskin bottles, and I helped filter the water and add chemicals to prepare the samples for further analysis later on.

Two PhD-students were working on an experiment to see how the swimming pattern of copepods is affected by noise emitted from wind turbines. First, they used a WP2 net to collect copepods from different depths. I helped sort and transfer the copepods into bottles. The copepods were then placed into a cage system and lowered back into the ocean. The cage was set up with cameras, sensors (hydrophones) and different types of light conditions (flashlight vs. natural light). This allowed the researchers to analyze the behavior of the copepods and relate their findings to the recorded noise and the respectable light conditions. Unfortunately, they were not able to conduct the study out at Hywind Tampen due to stormy weather. Instead, they conducted the experiments in Sognefjorden, studying ship noise.

Another researcher was studying bird behavior. One of the turbines at Hywind Tampen has a sensor that detects birds. However, at that point in time, the sensor was broken. Therefore, we had to do bird watching with binoculars instead. We looked at the type of bird, their behavior (if they were just hanging out, looking for food, passing through etc.). The end goal of this study is to gather enough information to make a device that could identify birds and bird behavior using machine learning.

A few DeepVision measurements were also conducted and the lander was deployed again to be out at sea until May 2025.

To summarize, I learned a lot and it was fun to see how marine research is conducted. I also learned how a lot of things go wrong, and how to deal with it and find creative solutions. I am overall very grateful for this experience.

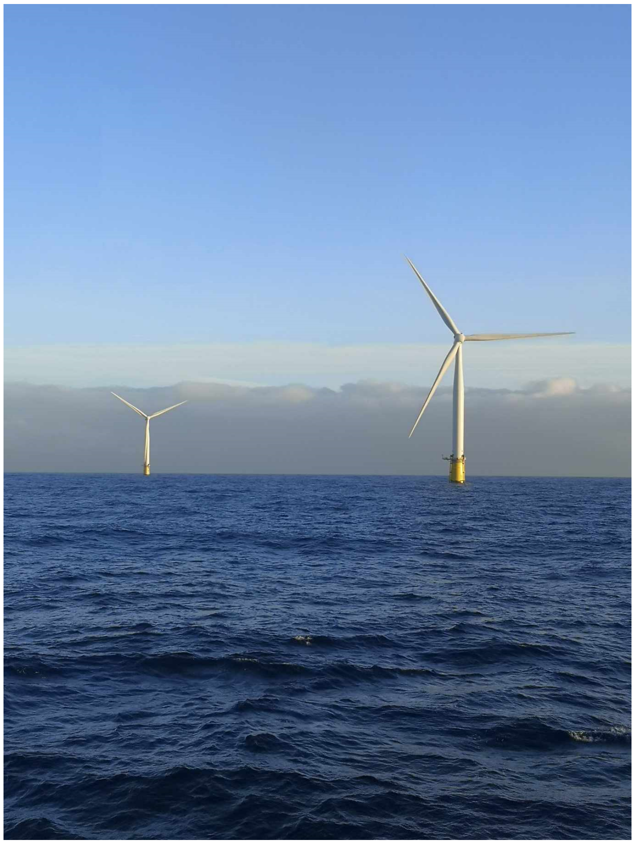

Figure B.1: Two of the 11 wind turbines at Hywind Tampen. Photograph is captured by Frida S. Eliassen.

Appendix C

ROMS Activated C-preprocessing Options

Table C.1: ROMS Activated C-preprocessing Options

Activated C-preprocessing Options	Description
UPWELLING	Wind-Driven Upwelling/Downwelling over a Periodic Channel
ANA_BIOLOGY	Analytical biology initial conditions
ANA_BPFLUX	Analytical bottom passive tracers fluxes
ANA_BSFLUX	Analytical kinematic bottom salinity flux
ANA_BTFLUX	Analytical kinematic bottom temperature flux
ANA_GRID	Analytical grid set-up
ANA_INITIAL	Analytical initial conditions
ANA_SMFLUX	Analytical kinematic surface momentum flux
ANA_SPFLUX	Analytical surface passive tracer fluxes
ANA_SRFLUX	Analytical kinematic shortwave radiation flux
ANA_SSFLUX	Analytical kinematic surface salinity flux
ANA_STFLUX	Analytical kinematic surface temperature flux
ANA_VMIX	Analytical vertical mixing coefficients
ASSUMED_SHAPE	Using assumed-shape arrays
AVERAGES	Writing out time-averaged nonlinear model fields
BIO_FENNEL	Fennel et al. (2006) nitrogen-based model
BIO_SEDIMENT	Restore fallen particulate material to the nutrient pool
BOUNDARY_ALLREDUCE	Using mpi_allreduce in mp_boundary routine
CARBON	Add Carbon constituents
COLLECT_ALLREDUCE	Using mpi_allreduce in mp_collect routine
DENITRIFICATION	Add denitrification processes
DIAGNOSTICS_BIO	Computing and writing biological diagnostic terms
DIAGNOSTICS_TS	Computing and writing tracer diagnostic terms
DIAGNOSTICS_UV	Computing and writing momentum diagnostic terms
DJ_GRADPS	Parabolic Splines density Jacobian (Shchepetkin, 2002)

Table C.1 – Continued

Activated C-preprocessing Options	Description
DOUBLE_PRECISION	Double precision arithmetic numerical kernel
MIX_S_TS	Mixing of tracers along constant S-surfaces
MIX_S_UV	Mixing of momentum along constant S-surfaces
MPI	MPI distributed-memory configuration
NONLINEAR	Nonlinear Model
!NONLIN_EOS	Linear Equation of State for seawater
POWER_LAW	Power-law shape time-averaging barotropic filter
PROFILE	Time profiling activated
REDUCE_ALLREDUCE	Using mpi_allreduce in mp_reduce routine
!RST_SINGLE	Double precision fields in restart NetCDF file
SALINITY	Using salinity
STEP2D_LF_AM3	Predictor/Corrector LF-AM3 stepping scheme
SOLVE3D	Solving 3D Primitive Equations
SPLINES_VDIFF	Parabolic Spline Reconstruction for Vertical Diffusion
SPLINES_VVISC	Parabolic Spline Reconstruction for Vertical Viscosity
!TALK_NONCONSERV	Alkalinity is passive and unaffected by nitrate or ammonium
TS_DIF2	Harmonic mixing of tracers
UV_ADV	Advection of momentum
UV_COR	Coriolis term
UV_U3HADVECTION	Third-order upstream horizontal advection of 3D momentum
UV_C4VADVECTION	Fourth-order centered vertical advection of momentum
UV_LDRAG	Linear bottom stress
UV_VIS2	Harmonic mixing of momentum
VAR_RHO_2D	Variable density barotropic mode

Appendix D

ROMS Grid Parameters

Table D.1: ROMS Model Grid Parameters

Value	Parameter	Description	Unit
41	Lm	Number of i-direction interior ρ-points	—
80	Mm	Number of j-direction interior ρ-points	—
16	N	Number of vertical levels	—
2.44	DX	Grid spacing in the x-direction	km
1.25	DY	Grid spacing in the y-direction	km
1.59–25.61	DZ	Vertical spacing	m
2304	ntimes	Number of timesteps for 3D equations	—
300	dt	Timestep size for 3D equations	s
30	ndtfast	Number of 2D timesteps between each 3D timestep	—
0.345	B-CFL	Barotropic Courant number	—
0.0384	C-CFL	Coriolis Courant number	—

Appendix E

ROMS Initial Conditions

Table E.1: ROMS Initial Conditions

Variable	**Value**	**Unit**
f (Coriolis)	1.28×10^{-4}	s^{-1}
ubar, vbar, u, v (velocities)	0	m/s
zeta (free surface)	0	m
Set incoming solar shortwave radiation	150	W/m^2
Potential temperature (temp)	[13.59–22.49]	°C
Salinity (salt)	35.00	PSU
NO_3 (nitrate)	[1.67–2.65]	$mmol\,m^{-3}$
NH_4 (ammonium)	0.10	$mmol\,m^{-3}$
Chlorophyll	0.02	$mg\,m^{-3}$
Phytoplankton	0.08	$mmol\,N\,m^{-3}$
Zooplankton	0.06	$mmol\,N\,m^{-3}$
LdetritusN (large detritus N)	0.02	$mmol\,N\,m^{-3}$
SdetritusN (small detritus N)	0.04	$mmol\,N\,m^{-3}$
LdetritusC (large detritus C)	0.002	$mmol\,C\,m^{-3}$
SdetritusC (small detritus C)	0.06	$mmol\,C\,m^{-3}$
TIC (total inorganic carbon)	2100	$\mu mol\,kg^{-1}$
Alkalinity	2350	$\mu mol\,kg^{-1}$

Appendix F

ROMS Mixing Coefficients

Table F.1: ROMS Vertical Mixing Coefficients

Variable	**Value**	**Unit**
Vertical mixing coefficients for salt, temp	1×10^{-6}	m^2/s
Vertical mixing coefficients for momentum	$2 \times 10^{-3} + 8 \times 10^{-3} \exp \frac{z_w}{150}$	m^2/s
Vertical mixing coefficients for biological tracers	15×10^{-5}	m^2/s
Non-linear Horizontal mixing coefficients for salt, temp	0	m^2/s
Non-linear Horizontal mixing coefficients for momentum	5	m^2/s

where z_w is the vertical position of the w-point in meter for all grid points in the $3D$-domain.

Appendix G

ROMS Physical Parameters

Table G.1: ROMS Physical Parameters

Value	Parameter	Description
2304	ntimes	Number of timesteps for 3-D equations.
300.000	dt	Timestep size (s) for 3-D equations.
30	ndtfast	Number of timesteps for 2-D equations between each 3D timestep.
1	ERstr	Starting ensemble/perturbation run number.
1	ERend	Ending ensemble/perturbation run number.
0	nrrec	Number of restart records to read from disk.
T	LcycleRST	Switch to recycle time-records in restart file.
288	nRST	Number of timesteps between writing data into restart fields.
1	ninfo	Number of timesteps between print of information to stdout.
T	ldefout	Switch to create a new output NetCDF file(s).
72	nHIS	Number of timesteps between writing fields into history file.
0	nQCK	Number of timesteps between writing fields into quicksave file.
1	ntsAVG	Starting timestep for accumulation of time-averaged data.
72	nAVG	Number of timesteps between writing time-averaged data into averages file.
1	ntsDIA	Starting timestep for accumulation of time-averaged diagnostics.
72	nDIA	Number of timesteps between writing diagnostics data.

Table G.1 – Continued

Value	Parameter	Description
0.0000E+00	nl_tnu2(01)	NLM horizontal harmonic mixing coefficient (m^2/s) for tracer 01: temp.
0.0000E+00	nl_tnu2(02)	NLM horizontal harmonic mixing coefficient (m^2/s) for tracer 02: salt.
5.0000E+00	nl_visc2	NLM horizontal harmonic mixing coefficient (m^2/s) for momentum.
F	LuvSponge	Turning OFF sponge on horizontal momentum.
F	LtracerSponge(01)	Turning OFF sponge on tracer 01: temp.
F	LtracerSponge(02)	Turning OFF sponge on tracer 02: salt.
1.0000E-06	Akt_bak(01)	Background vertical mixing coefficient (m^2/s) for tracer 01: temp.
1.0000E-06	Akt_bak(02)	Background vertical mixing coefficient (m^2/s) for tracer 02: salt.
1.0000E-05	Akv_bak	Background vertical mixing coefficient (m^2/s) for momentum.
3.0000E-04	rdrg	Linear bottom drag coefficient (m/s).
3.0000E-03	rdrg2	Quadratic bottom drag coefficient.
2.0000E-02	Zob	Bottom roughness (m).
2	Vtransform	S-coordinate transformation equation.
4	Vstretching	S-coordinate stretching function.
3.0000E+00	theta_s	S-coordinate surface control parameter.
0.0000E+00	theta_b	S-coordinate bottom control parameter.
25.000	Tcline	Surface/bottom layer width (m) for vertical stretching.
1025.000	rho0	Mean density (kg/m³) for Boussinesq approximation.
0.000	dstart	Time-stamp assigned to model initialization (days).
0.00	time_ref	Reference time for units attribute (yyyymmdd.dd).
0.0000E+00	Tnudg(01)	Nudging time scale (days) for tracer 01: temp.
0.0000E+00	Tnudg(02)	Nudging time scale (days) for tracer 02: salt.
0.0000E+00	Znudg	Nudging time scale (days) for free-surface.
0.0000E+00	M2nudg	Nudging time scale (days) for 2D momentum.
0.0000E+00	M3nudg	Nudging time scale (days) for 3D momentum.
0.0000E+00	obcfac	Factor between passive and active open boundary conditions.
F	VolCons(1)	Western edge boundary volume conservation OFF.

Table G.1 – Continued

Value	Parameter	Description
F	VolCons(2)	Southern edge boundary volume conservation OFF.
F	VolCons(3)	Eastern edge boundary volume conservation OFF.
F	VolCons(4)	Northern edge boundary volume conservation OFF.
14.000	T0	Background potential temperature (°C) constant.
35.000	S0	Background salinity (PSU) constant.
1027.000	R0	Background density (kg/m^3) for linear EOS.
1.7000E-04	Tcoef	Thermal expansion coefficient (1/°C).
0.0000E+00	Scoef	Saline contraction coefficient (1/PSU).
1.000	gamma2	Slipperiness: free-slip (1.0) or no-slip (–1.0).
F	LuvSrc	Turning OFF momentum point sources/sinks.
F	LwSrc	Turning OFF volume influx point sources/sinks.
F	LtracerSrc(01)	Turning OFF point sources/sinks on tracer 01: temp.
F	LtracerSrc(02)	Turning OFF point sources/sinks on tracer 02: salt.
F	LsshCLM	Turning OFF processing of SSH climatology.
F	Lm2CLM	Turning OFF processing of 2D momentum climatology.
F	Lm3CLM	Turning OFF processing of 3D momentum climatology.
F	LtracerCLM(01)	Turning OFF processing of tracer 01 climatology.
F	LtracerCLM(02)	Turning OFF processing of tracer 02 climatology.
F	LnudgeM2CLM	Turning OFF nudging of 2D momentum climatology.
F	LnudgeM3CLM	Turning OFF nudging of 3D momentum climatology.
F	LnudgeTCLM(01)	Turning OFF nudging of tracer 01 climatology.
F	LnudgeTCLM(02)	Turning OFF nudging of tracer 02 climatology.

Appendix H

ROMS Fennel Model Parameters

Table H.1: ROMS Fennel Model Parameters

Value	Parameter	Description
1	BioIter	Number of iterations for nonlinear convergence.
4.0000E-02	AttSW	Light attenuation of seawater (m^{-1}).
2.4860E-02	AttChl	Light attenuation by chlorophyll ($1/(mg \cdot Chl \cdot m^{-2})$).
4.3000E-01	PARfrac	Fraction of shortwave radiation that is photosynthetically active.
1.0000E+00	Vp0	Eppley temperature-limited growth parameter.
9.5000E-03	I_thNH4	Radiation threshold for nitrification (W/m^2).
1.0000E-01	D_p5NH4	Half-saturation radiation for nitrification (W/m^2).
5.0000E-02	NitriR	Nitrification rate (day^{-1}).
2.0000E+00	K_NO3	Inverse half-saturation for phytoplankton NO_3 uptake ($1/(mmol \cdot N \cdot m^{-3})$).
2.0000E+00	K_NH4	Inverse half-saturation for phytoplankton NH_4 uptake ($1/(mmol \cdot N \cdot m^{-3})$).
3.2000E+01	K_PO4	Inverse half-saturation for phytoplankton PO_4 uptake ($1/(mmol \cdot P \cdot m^{-3})$).
2.0000E+00	K_Phy	Zooplankton half-saturation for ingestion $(mmol \cdot N \cdot m^{-3})^2$.
5.3500E-02	Chl2C_m	Maximum chlorophyll to carbon ratio ($mg \cdot Chl/mg \cdot C$).

Table H.1 – Continued

Value	Parameter	Description
1.0000E-03	ChlMin	Chlorophyll minimum threshold ($mg\cdot Chl/m^3$).
6.6250E+00	PhyCN	Phytoplankton C:N ratio (mol·C/mol·N).
6.2500E-02	R_P2N	Phytoplankton P:N ratio (mol·P/mol·N).
1.5000E+00	PhyIP	Phytoplankton NH_4 inhibition parameter (1/mmol·N).
2.5000E-02	PhyIS	Initial slope of phytoplankton P–I curve ($mg\cdot C/(mg\cdot Chl\cdot W\cdot m^{-2}\cdot day)$).
1.0000E-03	PhyMin	Phytoplankton minimum threshold ($mmol\cdot N/m^3$).
1.5000E-01	PhyMR	Phytoplankton mortality rate (day^{-1}).
7.5000E-01	ZooAE_N	Zooplankton nitrogen assimilation efficiency.
1.0000E-01	ZooBM	Zooplankton basal metabolism rate (day^{-1}).
6.6250E+00	ZooCN	Zooplankton C:N ratio (mol·C/mol·N).
1.0000E-01	ZooER	Zooplankton excretion rate (day^{-1}).
6.0000E-01	ZooGR	Zooplankton maximum growth rate (day^{-1}).
1.0000E-03	ZooMin	Zooplankton minimum threshold ($mmol\cdot N/m^3$).
2.5000E-02	ZooMR	Zooplankton mortality rate (day^{-1}).
1.0000E-02	LDeRRN	Large detritus N remineralization rate (day^{-1}).
1.0000E-02	LDeRRC	Large detritus C remineralization rate (day^{-1}).
5.0000E-03	CoagR	Coagulation rate (day^{-1}).
3.0000E-02	SDeRRN	Small detritus N remineralization rate (day^{-1}).
3.0000E-02	SDeRRC	Small detritus C remineralization rate (day^{-1}).
3.0000E-02	RDeRRN	River detritus N remineralization rate (day^{-1}).
3.0000E-02	RDeRRC	River detritus C remineralization rate (day^{-1}).
1.0000E-01	wPhy	Phytoplankton sinking velocity (m/day).
1.0000E+00	wLDet	Large detritus sinking velocity (m/day).
1.0000E-01	wSDet	Small detritus sinking velocity (m/day).
3.7000E+02	pCO2air	CO_2 partial pressure in air (ppm).

Table H.1 – Continued

Value	Parameter	Description
0.0000E+00	nl_tnu2(03)	NLM horizontal mixing coeff. (m^2/s) for tracer 03: NO_3.
0.0000E+00	nl_tnu2(04)	NLM horizontal mixing coeff. for tracer 04: NH_4.
0.0000E+00	nl_tnu2(05)	NLM horizontal mixing coeff. for tracer 05: chlorophyll.
0.0000E+00	nl_tnu2(06)	NLM horizontal mixing coeff. for tracer 06: phytoplankton.
0.0000E+00	nl_tnu2(07)	NLM horizontal mixing coeff. for tracer 07: zooplankton.
0.0000E+00	nl_tnu2(08)	NLM horizontal mixing coeff. for tracer 08: LdetritusN.
0.0000E+00	nl_tnu2(09)	NLM horizontal mixing coeff. for tracer 09: SdetritusN.
0.0000E+00	nl_tnu2(10)	NLM horizontal mixing coeff. for tracer 10: LdetritusC.
0.0000E+00	nl_tnu2(11)	NLM horizontal mixing coeff. for tracer 11: SdetritusC.
0.0000E+00	nl_tnu2(12)	NLM horizontal mixing coeff. for tracer 12: TIC.
0.0000E+00	nl_tnu2(13)	NLM horizontal mixing coeff. for tracer 13: alkalinity.
F	LtracerSponge(03)	Sponge OFF on tracer 03: NO_3.
F	LtracerSponge(04)	Sponge OFF on tracer 04: NH_4.
F	LtracerSponge(05)	Sponge OFF on tracer 05: chlorophyll.
F	LtracerSponge(06)	Sponge OFF on tracer 06: phytoplankton.
F	LtracerSponge(07)	Sponge OFF on tracer 07: zooplankton.
F	LtracerSponge(08)	Sponge OFF on tracer 08: LdetritusN.
F	LtracerSponge(09)	Sponge OFF on tracer 09: SdetritusN.
F	LtracerSponge(10)	Sponge OFF on tracer 10: LdetritusC.
F	LtracerSponge(11)	Sponge OFF on tracer 11: SdetritusC.
F	LtracerSponge(12)	Sponge OFF on tracer 12: TIC.
F	LtracerSponge(13)	Sponge OFF on tracer 13: alkalinity.
1.0000E-06	Akt_bak(03)	Background vertical mixing coeff. (m^2/s) for tracer 03: NO_3.
1.0000E-06	Akt_bak(04)	Background vertical mixing coeff. for tracer 04: NH_4.
1.0000E-06	Akt_bak(05)	Background vertical mixing coeff. for tracer 05: chlorophyll.

Table H.1 – Continued

Value	Parameter	Description
1.0000E-06	Akt_bak(06)	Background vertical mixing coeff. for tracer 06: phytoplankton.
1.0000E-06	Akt_bak(07)	Background vertical mixing coeff. for tracer 07: zooplankton.
1.0000E-06	Akt_bak(08)	Background vertical mixing coeff. for tracer 08: LdetritusN.
1.0000E-06	Akt_bak(09)	Background vertical mixing coeff. for tracer 09: SdetritusN.
1.0000E-06	Akt_bak(10)	Background vertical mixing coeff. for tracer 10: LdetritusC.
1.0000E-06	Akt_bak(11)	Background vertical mixing coeff. for tracer 11: SdetritusC.
1.0000E-06	Akt_bak(12)	Background vertical mixing coeff. for tracer 12: TIC.
1.0000E-06	Akt_bak(13)	Background vertical mixing coeff. for tracer 13: alkalinity.
0.0000E+00	Tnudg(03)	Nudging timescale (days) for tracer 03: NO_3.
0.0000E+00	Tnudg(04)	Nudging timescale for tracer 04: NH_4.
0.0000E+00	Tnudg(05)	Nudging timescale for tracer 05: chlorophyll.
0.0000E+00	Tnudg(06)	Nudging timescale for tracer 06: phytoplankton.
0.0000E+00	Tnudg(07)	Nudging timescale for tracer 07: zooplankton.
0.0000E+00	Tnudg(08)	Nudging timescale for tracer 08: LdetritusN.
0.0000E+00	Tnudg(09)	Nudging timescale for tracer 09: SdetritusN.
0.0000E+00	Tnudg(10)	Nudging timescale for tracer 10: LdetritusC.
0.0000E+00	Tnudg(11)	Nudging timescale for tracer 11: SdetritusC.
0.0000E+00	Tnudg(12)	Nudging timescale for tracer 12: TIC.
0.0000E+00	Tnudg(13)	Nudging timescale for tracer 13: alkalinity.
F	LtracerSrc(03)	Point sources/sinks OFF on tracer 03: NO_3.
F	LtracerSrc(04)	Point sources/sinks OFF on tracer 04: NH_4.

Table H.1 – Continued

Value	Parameter	Description
F	LtracerSrc(05)	Point sources/sinks OFF on tracer 05: chlorophyll.
F	LtracerSrc(06)	Point sources/sinks OFF on tracer 06: phytoplankton.
F	LtracerSrc(07)	Point sources/sinks OFF on tracer 07: zooplankton.
F	LtracerSrc(08)	Point sources/sinks OFF on tracer 08: LdetritusN.
F	LtracerSrc(09)	Point sources/sinks OFF on tracer 09: SdetritusN.
F	LtracerSrc(10)	Point sources/sinks OFF on tracer 10: LdetritusC.
F	LtracerSrc(11)	Point sources/sinks OFF on tracer 11: SdetritusC.
F	LtracerSrc(12)	Point sources/sinks OFF on tracer 12: TIC.
F	LtracerSrc(13)	Point sources/sinks OFF on tracer 13: alkalinity.
F	LtracerCLM(03)	Climatology OFF on tracer 03: NO_3.
F	LtracerCLM(04)	Climatology OFF on tracer 04: NH_4.
F	LtracerCLM(05)	Climatology OFF on tracer 05: chlorophyll.
F	LtracerCLM(06)	Climatology OFF on tracer 06: phytoplankton.
F	LtracerCLM(07)	Climatology OFF on tracer 07: zooplankton.
F	LtracerCLM(08)	Climatology OFF on tracer 08: LdetritusN.
F	LtracerCLM(09)	Climatology OFF on tracer 09: SdetritusN.
F	LtracerCLM(10)	Climatology OFF on tracer 10: LdetritusC.
F	LtracerCLM(11)	Climatology OFF on tracer 11: SdetritusC.
F	LtracerCLM(12)	Climatology OFF on tracer 12: TIC.
F	LtracerCLM(13)	Climatology OFF on tracer 13: alkalinity.
F	LnudgeTCLM(03)	Nudging climatology OFF for tracer 03: NO_3.
F	LnudgeTCLM(04)	Nudging climatology OFF for tracer 04: NH_4.
F	LnudgeTCLM(05)	Nudging climatology OFF for tracer 05: chlorophyll.
F	LnudgeTCLM(06)	Nudging climatology OFF for tracer 06: phytoplankton.

Table H.1 – Continued

Value	Parameter	Description
F	LnudgeTCLM(07)	Nudging climatology OFF for tracer 07: zooplankton.
F	LnudgeTCLM(08)	Nudging climatology OFF for tracer 08: LdetritusN.
F	LnudgeTCLM(09)	Nudging climatology OFF for tracer 09: SdetritusN.
F	LnudgeTCLM(10)	Nudging climatology OFF for tracer 10: LdetritusC.
F	LnudgeTCLM(11)	Nudging climatology OFF for tracer 11: SdetritusC.
F	LnudgeTCLM(12)	Nudging climatology OFF for tracer 12: TIC.
F	LnudgeTCLM(13)	Nudging climatology OFF for tracer 13: alkalinity.